

DEVELOPMENT OF PHONON-MEDIATED
CRYOGENIC PARTICLE DETECTORS WITH
ELECTRON AND NUCLEAR RECOIL DISCRIMINATION

A DISSERTATION
SUBMITTED TO THE DEPARTMENT OF PHYSICS
AND THE COMMITTEE ON GRADUATE STUDIES
OF STANFORD UNIVERSITY
IN PARTIAL FULFILLMENT OF THE REQUIREMENTS
FOR THE DEGREE OF
DOCTOR OF PHILOSOPHY

Sae Woo Nam

December, 1998

© Copyright 1999 by Sae Woo Nam
All Rights Reserved

I certify that I have read this dissertation and that in my opinion it is fully adequate, in scope and in quality, as a dissertation for the degree of Doctor of Philosophy.

Blas Cabrera
(Principal Advisor)

I certify that I have read this dissertation and that in my opinion it is fully adequate, in scope and in quality, as a dissertation for the degree of Doctor of Philosophy.

Douglas Osheroff

I certify that I have read this dissertation and that in my opinion it is fully adequate, in scope and in quality, as a dissertation for the degree of Doctor of Philosophy.

Roger Romani

Approved for the University Committee on Graduate Studies:

Abstract

Observations have shown that galaxies, including our own, are surrounded by halos of "dark matter". One possibility is that this may be an undiscovered form of matter, weakly interacting massive particles (WIMPs).

This thesis describes the development of silicon based cryogenic particle detectors designed to directly detect interactions with these WIMPs. These detectors are part of a new class of detectors which are able to reject background events by simultaneously measuring energy deposited into phonons versus electron hole pairs. By using the phonon sensors with the ionization sensors to compare the partitioning of energy between phonons and ionizations we can discriminate between electron recoil events (background radiation) and nuclear recoil events (dark matter events). These detectors with built-in background rejection are a major advance in background rejection over previous searches.

Much of this thesis will describe work in scaling the detectors from $\frac{1}{4}$ g prototype devices to a fully functional prototype 100 g dark matter detector. In particular, many sensors were fabricated and tested to understand the behavior of our phonon sensors, Quasiparticle trapping assisted Electrothermal feedback Transition edge sensors (QETs). The QET sensors utilize aluminum quasiparticle traps attached to tungsten superconducting transition edge sensors patterned on a silicon substrate. The tungsten lines are voltage biased and self-regulate in the transition region. Phonons from particle interactions within the silicon propagate to the surface

where they are absorbed by the aluminum generating quasiparticles in the aluminum. The quasiparticles diffuse into the tungsten and couple energy into the tungsten electron system. Consequently, the tungsten increases in resistance and causes a current pulse which is measured with a high bandwidth SQUID system.

With this advanced sensor technology, we were able to demonstrate detectors with xy position sensitivity with electron and nuclear recoil discrimination. Furthermore, early results from running the 100g detector in the Stanford Underground Facility (SUF) indicate that competitive dark matter results are achievable with the current detector design.

Much of the design and testing of the experimental apparatus and instrumentation is described as well.

Acknowledgements

There are at least a hundred people I need to thank. At the top of the list is my advisor Blas Cabrera. I am grateful for his tolerance of my often reckless attitude regarding proper scientific procedure . I am also thankful for the amazing amount of latitude he has given me regarding the direction of my thesis. Furthermore, his breadth of knowledge in physics and related disciplines continually amazes me. I feel that I have greatly benefited from being under his guidance.

Over the years it has been enjoyable working with the various members of the Cabrera group. In the beginning, it was George Park who was the last person to write a thesis with Laser Switching and truly thought I had the potential to understand how to use SQUIDS. After George graduated, I felt like the odd man out. Everyone left in the group was married, Barron Chugg, Kent Irwin, and Michael Penn. I am greatly indebted to these three. Without their pioneering work, there would be nothing for me to write about. In many ways, I am enjoying the fruits of their labor.

More recently, I've felt like an old man interacting with the newer members of the group. Roland Clark was the first person to join Blas' group after me. He is a truly talented individual. His questions always make me realize how little I know. Andrea Davies is the latest person to join. Her diligence for writing things down is a God-send.

Then, there are the past members of the Cabrera group who were before my time, Adrian Lee and Betty Young. Both of whom, I had the privilege of interacting with

scientifically. I am also grateful for their conversation especially in regards to what my future plans are.

Within the Stanford Physics department, I am eternally grateful to the machine shop. Wolfgang Jung, Karlheinz Mehlke, and Dan Semnides are incredibly skilled machinists who were always willing to help me in my quest to make a better sample holder. In the main office, I wish to thank Marcia for making sure I always got paid, to Cindy Mendel for not yelling at me when I botched a purchase order, to Lori Jung and what's her name for entertaining conversation whenever I stole food from the main office. I would like to thank the late Barbara Dillard for teaching me how to be a good TA and to Olivia Martinez for good conversations regarding all aspects of life.

Outside of the Stanford Physics community, I have been fortunate to be involved in CDMS. I feel very lucky to have had the experience of working with people who think so differently than me yet want the same goal. I've enjoyed interacting with the crew from Berkeley and Santa Barbara which includes Bernard, Dan Akerib, Tom, Rick, Sunil, Walter, Angela, Josef, Andrew, and Dan Bauer. More recently (post thesis work), I have had a truly great time working with the people from Fermilab on CDMS, Mike Crisler, Steve Eichblatt, and Merle Haldeman. In particular, I must thank Steve for distracting me from writing. In the process, we've worked on things which have made reanalysis of a lot of the data in my thesis really easy.

Before CDMS and before QET phonon sensors, I was lucky enough to interact with John Martinis, Rick Welty, and Masoud Radparvar on the DC SQUID arrays. Their willingness to help me learn about SQUID arrays and their advantages really is one of the key technologies which made the work in my thesis possible.

I also need to thank Mike Hennessey. His help with maintenance of lab equipment and supplying me with vacuum equipment was indispensable. I also enjoyed our conversations at 5:30 in the morning when he arrived to work and when I would be

leaving.

Outside of my research group, I am thankful for all my friends in the Alpine Road House, Stu, Dan, Anneli, Andrei, Matthias, and Tony (honorary), the original Applied Physics 3pm frisbee crew, skirt frisbee (Lori, Betsy, Monica, Erin, et. al.), and the new working stiff's frisbee club at 3pm on Sundays.

John, Catherine, and Oscar, thanks for your support.

And, finally, I owe everything I've accomplished to my parents and sister for their unquestioned support throughout my whole 'formal' education process.

Contents

Abstract	iv
Acknowledgements	vi
1 Introduction	1
1.1 Evidence for Dark Matter	1
1.2 Nature of Dark Matter	3
1.2.1 Cosmology	3
1.2.2 Ω	4
1.2.3 Baryonic Dark Matter	5
1.2.4 Nonbaryonic Dark Matter	5
1.2.5 Hot Dark Matter	5
1.2.6 Cold Dark Matter	6
1.3 WIMP detection	7
1.3.1 Expected Rates	7
1.3.2 Detector Requirements	8
1.4 Breakdown of this thesis	9
2 Detector Description	11
2.1 Introduction	11
2.1.1 Phonon Sensors	11

2.1.2	Ionization	14
2.2	Phonon Sensor	14
2.2.1	Electro-Thermal Feedback Transition Edge Sensor	14
2.2.2	Quasi-particle Traps	16
2.2.3	Noise	17
2.2.4	Discussion of Time Constants	20
2.2.5	ETF Stability	24
2.3	Ionization Sensors	27
2.3.1	Circuit	27
2.3.2	Noise	28
2.3.3	Charge Trapping	30
2.4	Fabrication	31
3	Experimental Apparatus	32
3.1	Electronics	34
3.1.1	SQUID Electronics	45
3.1.2	Detector Biasing	46
3.1.3	SRS Amplifiers	48
3.1.4	Q amplifiers	49
3.2	Data Acquisition	49
3.2.1	Hardware	49
3.2.2	Software	52
4	Detector Evolution	53
4.1	Quasiparticle Trap Demonstration	53
4.1.1	W/Al 2-channel device	53
4.1.2	W/Al 2-channel device with Au heat sinks	59
4.2	Full Surface coverage	68

4.2.1	1 cm x 1 cm x 1 mm Phonon only sensors	69
4.2.2	1 cm x 1 cm x 1 mm Phonon and Ionization	73
4.3	Larger Mass	85
4.3.1	First Design	86
4.3.2	Phonons and Ionization	91
4.3.3	Second Design	103
4.4	First large Dark Matter detectors	108
4.4.1	Calibration	110
5	Simulations	114
5.1	Phonon Scattering Simulations	114
5.1.1	4-channel devices	115
5.1.2	100 g devices	117
5.2	Phonon Sensor	123
5.2.1	ETF Stability	123
5.2.2	Quasiparticle Trapping	127
5.3	Putting it all together	130
6	Conclusions	133
6.1	Design constraints for the phonon sensor	133
6.1.1	Performance	135
6.2	Current and Future detector work	135
6.3	CDMS	136
	Bibliography	139
A	Q amplifiers in detail	145
A.1	Noise in a the Charge Amplifier Readout	145
A.2	Ionization Signal to Noise Optimization	149

A.3	Calculating the electronics limit to the rise time	151
A.4	Determining Depth from charge amplifiers	156
A.5	UCB discrete Qamp addendum	158
B	Enhanced Electrothermal Feedback	162
B.1	Enhanced ETF simplified theory [†]	162
B.2	Noise issues with EETF	164
B.2.1	Electronics noise contribution	166
B.2.2	Johnson noise contribution	167
B.2.3	Phonon noise contribution	167
B.3	Fundamental Energy Resolution	168
B.4	Dynamic and source resistance Corrections	171

List of Tables

3.1 Summary of the Noise performance of a two-stage system 44

List of Figures

1.1	Example of a galaxy rotation curve.	2
2.1	Thermal picture of an ETF-TES sensor	15
2.2	Cartoon of Quasiparticle Trapping in a QET phonon sensor	18
2.3	Schematic of the circuit used to voltage bias and readout a QET sensor.	19
2.4	Johnson noise in phonon bias schematic	19
2.5	Example of pulses from four phonon sensor on a $\frac{1}{4}$ g substrate.	21
2.6	Sketch of the $\frac{1}{4}$ g device	21
2.7	Schematic of the Ionization bias and readout circuit.	28
2.8	Sketch of prototype detectors with phonon and ionization sensors.	28
2.9	Sketch of the first 100 g Dark Matter detector.	29
2.10	Ionization circuit for noise analysis	29
3.1	Picture of the Kelvinox 15, KO-15.	33
3.2	Photograph of a mounted 1 cm x 1 cm x 1 mm device	33
3.3	Sketch of the dunk probe for testing the SQUID arrays for use in a liquid Helium storage dewar.	35
3.4	Sketch of the G-10 PC board used for holding the SQUID array chips.	37
3.5	Picture of the SQUID array chip.	37
3.6	Schematic of the bias and readout of the SQUID arrays.	39
3.7	IV Curve of the SQUID array for various input currents.	39

3.8	Typical $V-\Phi$ curve for a SQUID array.	40
3.9	Schematic of the Instruments used and controlled to do a SQUID array noise measurement	41
3.10	Schematic of the bias and readout scheme for the two-stage SQUID system.	42
3.11	Example of the output of the LabView program in EXCEL format of a SQUID noise measurement.	43
3.12	$V-\Phi$ curve of the two stage SQUID system.	44
3.13	Diagram of the flux locked loop system for the SQUID arrays.	46
3.14	Step function response of the SQUID array with the flux feedback electronics.	47
3.15	Simplified Schematic of the flux feedback circuit for the SQUID arrays.	47
3.16	Schematic of the circuit used to voltage bias the phonon sensors.	48
3.17	Sketch of the G-10/fiberglass enclosure to shield the FET radiation from the detector.	49
3.18	Glitch associated with triggering the COMETs.	50
3.19	Noise induced by the COMET digitizers on the signal of interest on a long time base.	51
3.20	Detailed plot (short timebase) of the noise induced by the COMET digitizing.	51
4.1	Single pixel of a QET phonon sensor	54
4.2	Sketch of the experimental setup of the detector and radioactive source	55
4.3	An example of pulses from the first demonstration of Quasiparticle trapping with ETF/TES sensors.	55
4.4	A vs. B plot for a two channel device	57

4.5	Partitioning of phonon energy between two sensors after different amounts of LED exposure	58
4.6	Partitioning of energy between two sensors calculated with different integration times	60
4.7	Examples of injected heat pulses and real pulses	61
4.8	Ibias vs. Isensor and other diagnostic plots	62
4.9	Peak a vs Peak b as a function of bias current	64
4.10	Collected energy in A versus collected energy in B as a function of bias current	65
4.11	Histogram of the sum of the peak height in A and B as function of current bias.	66
4.12	Histogram of the sum of the collected energy in A and B as function of current bias.	66
4.13	Examples of pulses which saturates a phonon sensor by driving the tungsten completely normal.	67
4.14	A sketch (not drawn to scale) of the 1cm x1cm x1mm 1/4g detector and the phonon sensor labeling scheme used to describe the results. .	68
4.15	A sketch of the source and collimator position of the ^{55}Fe used with the 1/4g detectors.	69
4.16	A plot of the energy collected in two sensors (A and B) versus the energy collected in two others (C and D).	69
4.17	Plot of the partitioning of energy between the four sensors for 6 gamma rays.	70
4.18	Plot of the partitioning of energy between the four sensors from 60 gamma rays.	71
4.19	fig:etf19-collection	71
4.20	Histograms of the energy collected in the four phonon sensors.	71

4.21	Delay Plot from a 6 keV gamma source	72
4.22	Histogram of the events from a 6 keV gamma source hitting the center of the detector.	73
4.23	AB versus CD for 60 keV gamma rays in a detector with and without a Au electrode on the backside	75
4.24	Raw plot of the collected energy versus ionization.	75
4.25	Plot of the energy partitioning in the x-direction versus the delay in signals in the x-direction.	76
4.26	Plot of the energy partitioning in the y-direction versus the delay in signals in the y-direction.	77
4.27	Plot of the collected energy versus ionization for events in the middle of the crystal.	77
4.28	2D plot with a rain cloud due to incomplete charge collection.	78
4.29	2D plot with the rain cloud removed by cutting events which occur near the edges of the detector.	78
4.30	Raw 2D plot from exposing the detector to a PuBe neutron source.	79
4.31	Plots used to determine the proper position cuts to eliminate events near the edges of the detector.	80
4.32	2D plot after removing events near the edges.	81
4.33	2D plots of collected energy versus ionization as a function of applied electric field for the ionization to demonstrate the Luke effect.	82
4.34	AB versus CD as a function of applied electric field for events from a 6 keV gamma source.	83
4.35	Seagull plot	83
4.36	2D plots of a neutron calibration and gamma ray calibration corrected so that the recoil energy is plotted versus ionization.	84

4.37 Ionization yield plotted as a function of recoil energy from exposure to a neutron source and a gamma ray source.	85
4.38 Sketch of pixel styles	86
4.39 Affects of an adsorbed Helium layer on a detector	87
4.40 Position sensitivity of a 4 g detector to 6 keV X-rays.	89
4.41 Response of the 4 g detector to the 60 keV gamma ray source.	90
4.42 Plots demonstrating the position dependence to the collected energy .	92
4.43 2D plots of the gamma response	93
4.44 Plot showing space charge buildup.	93
4.45 Gamma-ray and neutron response of the 4 g detector.	95
4.46 IbIs curves for a device with 100 μm tungsten lines.	96
4.47 IbIs curves for a device with 400 μm tungsten lines.	97
4.48 Measurement of the W transition temperature with different levels of heat sinking and radiation shielding.	99
4.49 Photograph of a heat sink.	100
4.50 Thermal crosstalk between phonon sensors.	100
4.51 DC baseline jumps in a detector with 800 μm tungsten lines.	102
4.52 No DC baseline jumps in a detector with 100 μm tungsten lines. . . .	102
4.53 DC baseline jumps in a detector with 400 μm tungsten lines.	102
4.54 Uncorrected and corrected resopnse of the phonon sensors on a 4 g detector.	103
4.55 Phonon sensor response on a 4 g detector in which the IVC walls are below 4K.	104
4.56 Effects on phonon collection in a detector with an Au electrode on the backside.	105
4.57 IbIs curves for a 4 g detector with the IVC walls at 4 K.	106
4.58 IbIs curves for a 4 g detector with the IVC walls less than 4 K.	106

4.59	A sketch of an old short W pixel and a new W pixel	107
4.60	Plot of the power dissipated by the sensor.	107
4.61	Example of pulses from a detector with the new pixel design showing the fast risetime.	108
4.62	Example of pulses from an detector with an old pixel design with slower risetimes.	109
4.63	Sketch of the first 100 Si Dark Matter detector using QET technology.	109
4.64	Raw 2D plot from a gamma source calibration.	110
4.65	Raw 2D plot from a neutron source calibration.	111
4.66	“Bean Plot”	112
4.67	Corrected 2D plot of the neutron response.	112
5.1	Phonon track in a 4 g detector.	115
5.2	Summary of the phonon propagation Monte Carlos in a 4 g device. . .	116
5.3	Phonon track in a 100 g detector.	117
5.4	Summary of the phonon propagaion Monte Carlos.	118
5.5	Summary of the phonon propagation Monte Carlos in a 100 g device assuming calculated phonon transmission coefficients [37]	119
5.6	Summary of phonon propagation Monte Carlos in a 100 g detector with no absorption of phonons in the outer W electrode.	120
5.7	Summary of phonon propagation Monte Carlos in a 100 g detector with grided electrodes.	121
5.8	Sketch of a future detector design with phonon sensors on both sides.	121
5.9	Plot showing the partitioning of phonon energy for different event locations.	122
5.10	Finite difference model of the heat flow in the tungsten meanders. . .	124
5.11	Summary of the results of modeling the heat flow in the W meanders.	125

5.12	Response of the W meander to injection of heat at eight points. . . .	126
5.13	Time evolution of quasiparticles assuming a simple diffusive model. .	128
5.14	Time evolution of quasiparticles assuming a simple diffusive model and four recombination sites possibly due to magnetic flux.	129
5.15	Flux of quasiparticles from the Aluminum fin into the W with and without trapping sites.	130
5.16	Predicted pulse shapes based on models of phonon propagation, quasi- particle diffusion, and ETF response.	132
6.1	Experimental sensitivity to estimating the WIMP cross section. . . .	137
A.1	Schematic of a charge amplifier with signal and noise sources.	145
A.2	The Bode plot of the magnitude of the gain/transimpedance of the charge amplifier shown in figure A.1	146
A.3	Bode plot of the magnitude of $H(s)$	147
A.4	The system function response for a voltage noise source.	147
A.5	Sketch of a typical voltage noise spectrum for the front end compo- nents of a charge amplifier	148
A.6	The contribution of the input voltage noise to the output voltage noise.	148
A.7	Typical input current noise for a charge amplifier.	149
A.8	The contribution of the input current noise to the output voltage noise.	149
A.9	Q amp schematic which includes the blocking capacitor and the input capacitance of the charge amplifier	150
A.10	Schematic of the Q amplifier including noise sources	151
A.11	Simplified Schematic of the Q amplifier	152
A.12	Leading edge behavior of Q pulses assuming a GBW of 1×10^8	157
A.13	Leading edge behavior of Q pulses assuming a GBW of 2×10^9	157
A.14	Leading edge behavior of Q pulses assuming a GBW of 2×10^{10}	158

A.15 Simplified Schematic of the UCB Berkeley Q-amp	160
---	-----

Chapter 1

Introduction

Many types of observations show that galaxies, including our own, are surrounded by massive halos consisting of matter that is "seen" only gravitationally and does not emit or absorb detectable electromagnetic radiation at any known wavelength. The nature of this dark matter is unknown.

This chapter briefly discusses the arguments for the existence of dark matter, the evidence that dark matter consists of as yet undiscovered weakly interacting massive particles (WIMPs) that were produced in the early universe, and the sensitivity requirements for a detector which could directly observe these particles.

1.1 Evidence for Dark Matter

Today, the strongest evidence for dark matter comes from studying of the motion of stars in spiral galaxies. In spiral galaxies, stars lie in a thin disc and travel in circular orbits around a galactic core. The rotation curve for a galaxy is the observed rotational velocity as a function of radial distance from the center of the galaxy. Using measurements of the rotational velocity, we can estimate the radial distribution of the mass of the galaxy by equating the gravitational acceleration with

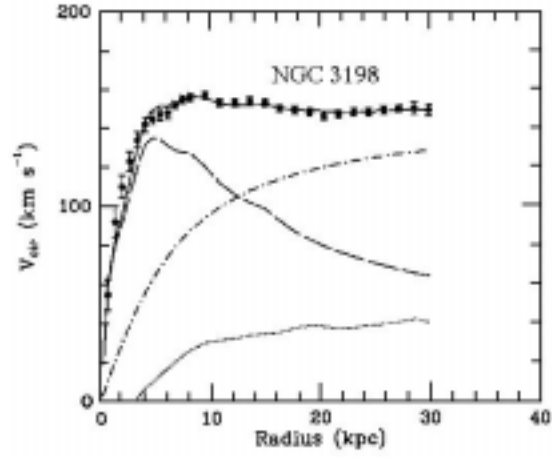


Figure 1.1: Example of a galaxy rotation curve.

the centripetal acceleration:

$$\frac{GM(r)}{r^2} = \frac{v(r)^2}{r} \quad (1.1)$$

where $M(r)$ is the mass within a radius r from the center of the galaxy and $v(r)$ is the velocity of a circular orbit at that radius.

Rotation curves are measured most sensitively by measuring the Doppler shift of the 21 cm line of hydrogen. Measurements of several spiral galaxies by Rubin and others [38] have shown that the rotations curves have a steep rise near the center of the galaxy and are relatively constant out the furthest radii measurable. A clean example of such a curve is show in Fig. 1.1 [3] . The raw data is fitted to a three parameter dark halo fit, solid line. The individual components of the fits are also shown. The dashed curves are for the visible component of the galactic disk which extends to ~ 5 kpc and starts to roll off. The dotted curve is an estimate for the gas component and the dash-dot curve is the dark halo component. The evidence for dark matter lies in the fact that the observed velocity does not show the expected Keplerian decline for distances beyond the optically visible radius of the galaxy. Instead, we see from the graph and Eq.1.1 that a constant $v(r)$ implies that $M(r)$ increases linearly with r beyond the visible component of the galaxy.

Although the exact shape of the dark matter halos can not be determined from these measurements, a simple empirical model for the dark matter halo density was proposed by Caldwell and Ostriker [7] :

$$\rho_d(r) = \frac{\rho_o}{1 + \frac{r^2}{r_c^2}} \quad (1.2)$$

where the central density, ρ_o , and the core radius, r_c are fitted parameters.

1.2 Nature of Dark Matter

1.2.1 Cosmology

The standard model for the universe is the big bang model. The model describes the universe as being homogeneous and isotropic. The dynamics of the universe is described by the evolution of the scale factor which is given by Friedmann equation

$$\left(\frac{\dot{R}}{R}\right)^2 + \frac{k}{R^2} = \frac{8\pi G}{3}\rho \quad (1.3)$$

where R is the scale factor, k is the spatial curvature, G is the gravitational constant, and ρ is density of the universe. The Hubble constant, H , is defined to be $\frac{\dot{R}}{R}$ and describes the expansion of the universe.

By replacing $\frac{\dot{R}}{R}$ with H , and rearranging the Friedmann equation, we arrive at the expression

$$\frac{k}{H^2 R^2} = \frac{\rho}{\frac{3H^2}{8\pi G}} - 1. \quad (1.4)$$

It is useful to define the critical density, ρ_c as

$$\rho_c = \frac{3H^2}{8\pi G} \quad (1.5)$$

and

$$\Omega = \frac{\rho}{\rho_c}. \quad (1.6)$$

As a result, we can rewrite the Friedmann equation in the form:

$$\frac{k}{H^2 R^2} = \Omega - 1 \quad (1.7)$$

There are essentially three possibilities for Ω . For $\Omega > 1$, the universe is said to be closed and that the universe will eventually collapse upon itself. For $\Omega < 1$, the universe is said to be open, and the universe will expand forever. For $\Omega = 1$, the universe is said to be flat, and that as $t \rightarrow \infty$, the universe stops expanding.

Because the Hubble constant is not a constant in time, it is customary to label present day values for H , Ω , ρ , and ρ_c with a subscript “o”. For convenience, it is also common to write the Hubble constant as h_o in units of 100 km/sec/Mpc. The Hubble constant is generally agreed to be $0.5 \leq h_o \leq 1$ and more recently $0.5 \leq h_o \leq 0.75$.

1.2.2 Ω

Attempts have been made to measure Ω by examining very distant objects. For example, a lower limit of $\Omega > 0.2$ can be obtained by using the virial theorem and measurements of the peculiar velocity of the galaxies in clusters or superclusters of galaxies [46]. Estimates of Ω over longer distance scales from large scale flows of galaxies and clusters of galaxies find Ω to be closer to 1 [11, 10].

There are strong theoretical prejudices favoring $\Omega = 1$. Since $\Omega = 1$, is an unstable equilibrium, any small deviation from 1 will grow exponentially with time. The fact that Ω is within an order of magnitude of 1 today indicates that $|\Omega - 1| < 10^{-16}$ at the time of nucleosynthesis. Inflationary theories which provide explanations for the observed homogeneity and isotropy in the universe [12] predict $|\Omega - 1| \lesssim 10^{-60}$.

1.2.3 Baryonic Dark Matter

The strongest limits on Baryonic dark matter are from considering the big bang nucleosynthesis model (BBN). By studying the remaining abundances of the light elements, D, He^3 , He^4 , and Li^7 , the fraction of the critical density which consists of Baryons is bounded by $0.02 \leq \Omega_b \leq 0.14$ for $0.04 \leq h_o \leq 0.7$ [14] .

From observations on the mass to light ratio of galaxies and clusters, the fraction of the critical density from visible matter is less than 0.01 [35] . Consequently, we can conclude that

$$\Omega_{\text{visible}} < \Omega_b < \Omega. \quad (1.8)$$

It follows that some of the dark matter is baryonic and non-baryonic.

The recent MACHO and EROS reports of gravitational microlensing suggest that some of the dark matter in the halo surrounding galaxies may be baryonic. [1, 43] However, theoretical and observational uncertainties make it unlikely that MACHOs makes up the entire dark matter halo[16].

1.2.4 Nonbaryonic Dark Matter

Nonbaryonic Dark Matter is typically classified into two broad classes, Hot (HDM) and Cold (CDM) dark matter. The distinction arises from whether the particle was relativistic (HDM) or non-relativistic (CDM) at the at the start of galaxy formation after the big bang.

1.2.5 Hot Dark Matter

Hot dark matter candidates such as massive neutrinos are no longer thought to be the primary constituent of dark matter. Hot dark matter tends to smooth out

density fluctuations rather than enhance density fluctuation during structure formation during the early universe. Consequently, the first structures to form in a hot dark matter universe are supercluster size objects with galaxy sized object forming later. Although the existence of hot dark matter leads to a picture of the universe with superclusters and voids roughly of the size seen, galaxies are believed to older than superclusters. Furthermore, in order to be consistent with results from the COBE data, superclusters would be just beginning to form at the present time with hardly any smaller-scaled objects such as galaxies [36] . Consequently, because recent observations contradict the predictions from assuming hot dark matter dominated universe, hot dark matter is no longer the preferred possibility for the nature of dark matter.

1.2.6 Cold Dark Matter

A currently popular possibility is that the dark matter is cold. Two possible candidates are axions and WIMPs. The existence of axions were postulated to explain the CP violation in strong interactions. The mass and abundance depend upon models chosen. Experiments to detect axions are being performed to explore this possibility [18] .

Weakly Interacting Massive Particles (WIMPs) are another possible explanation of dark matter and is the focus of the detectors developed in this thesis. These particles are believed to have been produced in thermal equilibrium at early times in the universe. As the universe cools below the temperature associated with the mass (energy) of the WIMP, the number density of the WIMPs drops exponential due to the Boltzman factor. As the universe cools and expands, the number density becomes fixed (freeze-out) because the number density is too low for annihilation to continue in thermal equilibrium. If the annihilation rate were much higher than the expansion rate of the universe all of the WIMPs would have disappeared. If the

annihilation rate were smaller than the expansion rate, the WIMP contribution to the mass of the universe can be estimated by

$$\Omega_\chi h^2 \approx \frac{3 \cdot 10^{-27} \text{cm}^2 \text{sec}^{-2}}{\langle \sigma \rangle |v|} \quad (1.9)$$

where Ω_χ is the normalized density of wimps, σ is the cross section, and v is the velocity of the WIMP [23]. If Ω_χ is of order of 1, then the cross section is an indication of weak interaction physics (hence the name WIMPs). Just as axions were postulated to explain CP violation, supersymmetry predicts the existence of “supersymmetric partner particles”. Many supersymmetric models predict the existence of particles with just the right properties to possibly make up dark matter.

1.3 WIMP detection

1.3.1 Expected Rates

If WIMPs are the dark matter in the universe, one possibility is that the Earth is moving through a sea of these relic particles. The most likely WIMP detecting interaction is coherent scattering off a target nucleus. In general, the cross sections for scattering have both spin-independent and spin-dependent contributions. In most cases, the spin-independent term dominates and is given by

$$\sigma_o^{scalar} = \frac{4m_\chi^2 m_N^4}{\pi (m_\chi + m_N)^2} \left(\frac{f_n}{m_n} \right)^2 \quad (1.10)$$

where m_χ is the mass of the WIMP, m_N is the mass of the target material, f_n is the WIMP-nucleon coupling, and m_n is the average nucleon mass [24]. Assuming a Maxwell-Boltzmann distribution of WIMPs in our galaxy, the rate of interactions

as a function of recoil energy is approximately given by[28]

$$\frac{dR}{dE} = \frac{2\sigma_o\rho_ov_o}{\sqrt{\pi}m_\chi m_N} \frac{1}{rE_o} \exp\left(\frac{-E}{rE_o}\right) (F(E))^2 \quad (1.11)$$

where E is the recoil energy, σ_o is the cross section, ρ_o is the local density, v_o is the WIMP velocity, $r = 4m_\chi m_N/(m_\chi + m_N)^2$, E_o is the kinetic energy of the wimp, and $F(E)$ is a nuclear form factor. Estimates of from galactic modeling suggest that ρ_o is 0.3 GeV/cm^3 , and that there is a Maxwell-Boltzmann distribution of WIMPs with a velocity of $\approx 220 \text{ km/sec}$. The resulting expected event rate for silicon or germanium target material detectors is approximately 1 count/kg/day . with typical recoil energies of order 10 keV .

1.3.2 Detector Requirements

Another important consideration in a dark matter search experiment is an understanding of likely radioactive backgrounds. Besides possible WIMP events occurring at the rate of $1 \text{ count/kev/kg/day}$, a WIMP detector will also be exposed to a variety of natural radioactivity such as cosmic rays, neutrons induced by cosmic rays, γ -rays, x-rays, β -particles, and α -particles. The level of radioactive background determines the sensitivity to detecting dark matter.

In the Cryogenic Dark Matter Search (CDMS) for which the detectors described in this thesis were developed, an active plastic scintillation system surrounds the experiment to veto events correlated to cosmic rays and high energy γ -rays entering the detector system. In addition, the detectors are surrounded by copper, lead, and polyethylene to attenuate γ -rays, x-rays, and neutrons. However, in spite of the radioactive shielding, natural radioactivity in the detector itself and materials near the detector are enough to contaminate the energy spectrum making identification of possible dark matter difficult. The best achieved background rate is ≈ 0.2

count/kg/keV/day at 10 keVee [19] . There are two major ways to reduce the background. The first is the use of detectors capable of distinguishing between events from particles which recoil off of nuclei (WIMPs) and events from particles which recoil off of electrons (γ -rays, x-rays, and β particles). In the detectors described in this thesis, the discrimination is accomplished by the simultaneous measurement of the amount of ionization generated and the amount of phonon energy deposited by a particle hitting the target material. The second technique to reduce background contamination is the use of a detector capable of imaging the location of the particle interaction. Background contamination such as β 's and low energy γ rays interacts close to the surface of the detectors. As a result, by defining a fiducial volume which excludes the surface of the detector, lower background event rates can be achieved. The target goals for CDMS at Stanford University is 0.03 counts/kg/keV/day for nuclear recoils.

1.4 Breakdown of this thesis

The group at Stanford with which I worked on this thesis and a few others around the world have made tremendous progress in the development of detectors for the direct detection and identification of dark matter particles. With this work, I describe the scaling of a silicon based cryogenic particle detector to detect WIMPs. The detectors are part of a new generation of dark matter detectors which are intrinsically able to distinguish nuclear recoil events (WIMP signal) and electronic recoil events (background). Furthermore, the detectors developed as part of this thesis begin to explore the possibility of background suppression because of their ability to image the x, y, and z position of particle hitting the detector.

The remainder of this thesis is organized as follows. Chapter 2 describes the basic principles behind the detection scheme. More emphasis is placed on the phonon

detection scheme because our detector development concentrated on successfully scaling this technique. Chapter 3 describes much of the experimental apparatus developed and used with the detectors as they evolved. In chapter 4, I discuss the various experiments performed as the detectors were scaled from $\frac{1}{4} g$ devices to a 100 g dark matter detector. Chapter 5 summarizes the results of numerical modeling of the detectors to better understand practical design constraints. Finally, in chapter 6, I summarize the results and describe some of the early results of using these detectors in CDMS.

Chapter 2

Detector Description

2.1 Introduction

The detectors are made on ultra pure silicon substrates. The substrates are the actual target material for dark matter and are maintained at temperatures less than 50 mK. When an interaction occurs in the crystal some of the energy goes into the creation of electron-hole pairs and the rest goes into the generation of phonons. Simultaneous measurement of the ionization energy and phonon energy first demonstrated by Shutt et al. [39] makes it possible to discriminate between particles which recoil off nuclei and particles which recoil off electrons. Discrimination between nuclear and electron recoils is possible because nuclear recoils deposit a significantly smaller fraction of their energy into the generation of electron-hole pairs.

2.1.1 Phonon Sensors

In order to develop a dark matter detector, nuclear recoil energies on the order of a few keV must be observed. For nuclear recoil energies < 10 keV, $\approx 90\%$ of the energy is deposited into the phonon system of the silicon. Therefore, it is of tremendous advantage to design detectors which measure the phonon energy.

When a particle interaction occurs in a silicon crystal, energy is deposited in the form of high energy optical phonons and the creation of electron-hole pairs [27, 26]. In very pure silicon, there are two dominant phonon scattering processes, isotope scattering and anharmonic decay. Isotope scattering is an elastic process and results in changing the polarization of the phonon. The time constant for scattering has been calculated and is given by

$$\tau_I = 0.4097 \left(\frac{1 \text{ THz}}{\nu} \right)^4 \mu s \quad (2.1)$$

where ν is the frequency of the phonon [42]. Anharmonic decay is an inelastic process and results in a phonon splitting into two phonons of lesser energy [2]. The time constant for anharmonic decay scales as

$$\tau_{Anh} \propto \left(\frac{1}{\nu} \right)^5. \quad (2.2)$$

According to calculations done by Tamura [41],

$$\tau_{Anh} = 25 \left(\frac{1 \text{ THz}}{\nu} \right)^5 \mu second \quad (2.3)$$

The phonons from a particle interaction decay into a roughly gaussian distribution of acoustic phonons centered around 1 THz ($\approx 4 \text{ meV}$) after a few microseconds. When a phonon decays sufficiently, its mean free path becomes on the same order as the size of the crystal. Then, it can propagate across the crystal without scattering. This type of phonon is termed ballistic. After several milliseconds, the phonons completely thermalize causing a rise in the overall crystal lattice temperature.

Most phonon-mediated cryogenic particle detectors for dark matter are calorimetric and rely on sensitive thermometers to measure very small changes in the temperature of the crystal absorber after the phonons have thermalized within the

absorber. There are several important issues which must be considered when operating detectors of this type. One important issue is the heat capacity of the absorber. Considerable care must be taken to ensure that the heat capacities of the thermometer and crystal are balanced for optimal signal to noise. In addition, the signal strength (temperature change) decreases as the crystal absorber mass is scaled upwards. Another consideration is that of speed. For calorimeters, the speed is limited by the thermalization time constants. The fact that some of the time constants are on the order of tens of milliseconds makes such detectors more susceptible to problems associated with pulse pileup, microphonics, and $1/f$ noise sources. It is also important to tune the thermal conductivities carefully. For example, if the conductivity between the absorber and refrigerator is too strong, the signal (temperature change) will be attenuated. It is important that the conductivity between the thermometer and absorber be much stronger. At low temperatures, these parameters can be difficult to achieve.

The focus of our group at Stanford has been to develop detectors for dark matter searches and neutrino experiments to utilize the information in the distribution of athermal phonons.

One advantage of sensors using athermal phonons is the time constants involved. The time constants are dominated by the phonon collection time and the sensor thermalization time. The detectors described in this thesis operate on timescales on the order of $100\ \mu\text{seconds}$. Another advantage is the less severe restriction on target material heat capacity. To first order, the heat capacity of the absorber does not pose any limitations. Instead, for the sensors described in this thesis, the heat capacity of the active sensing element is a critical parameter. This feature is advantageous for scaling up the absorbers in mass more sensitive dark matter searches. For large absorbers, the amount of phonon sensing material may not need to increase. Because a significant fraction of the athermal phonon distribution is ballistic and because the

final down conversion site is near the initial particle interaction, an array or grid of athermal phonon sensors on the surface of a target crystal is able to resolve the position of the interaction. The ability to determine position information will be a powerful tool in background rejection for Dark Matter searches.

2.1.2 Ionization

The most important background discrimination tool for the CDMS detectors is the electronic and nuclear recoil discrimination. This technique relies on the use of a semiconductor target and the fact that particles which recoil off of a nucleus deposit less of their energy into the generation of electron-hole pairs than events which recoil off an electron. Consequently, by simultaneously measuring the phonon energy and amount of ionization, we are able to determine whether an event was an electronic or nuclear recoil. This technique was first demonstrated by T. Shutt, et al. [39] The ionization signal also provides the best time stamp for when a particle interacts within the crystal absorber because the electron-hole pairs drift across the crystal on time scales much faster than the times involved in measuring the phonon energy. This effect is a very useful tool because it provides a start time for an event to look at the relative timing delays and leading edge structure on the phonon pulses.

2.2 Phonon Sensor

2.2.1 Electro-Thermal Feedback Transition Edge Sensor

The phonon sensor technology described in this work is a continuation of the work begun by previous members of the Stanford group, Kent Irwin and Barron Chugg.

The Electro-Thermal Feedback Transition Edge Sensors (ETF-TES) that we use consist of superconducting thin films of W deposited on a silicon substrate (crystal

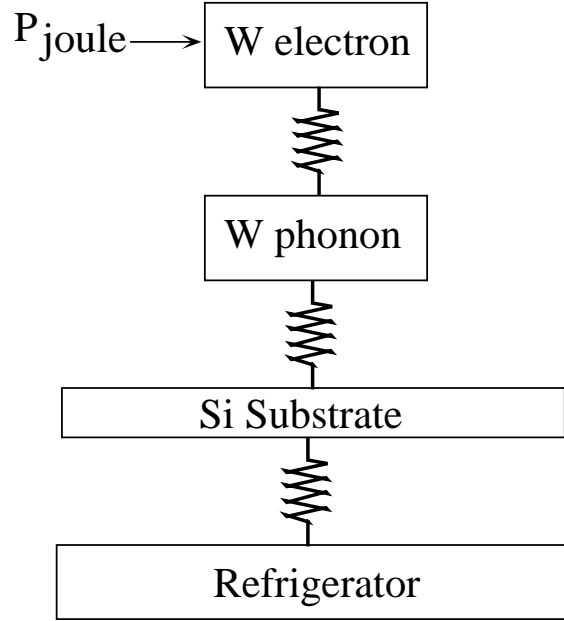


Figure 2.1: Thermal picture of an ETF-TES sensor

absorber). For an ETF-TES, the temperature of the substrate is cooled below the T_c of the superconductor, and the film is voltage biased. A thermal model of the sensor appears in figure 2.1. In our case, the T_c is ≈ 80 mK. Near this temperature, there is electron-phonon decoupling in the tungsten. Consequently, the thermal impedance between the electrons and phonons in the tungsten is the dominant impedance. We can simplify the thermal picture and write the following equation to describe the temperature of the electrons in the tungsten:

$$c_v \frac{dT}{dt} = \frac{V_{bias}^2}{R(T)} - \kappa(T^n - T_s^n), \quad (2.4)$$

where T is the electron temperature of the tungsten, c_v is the electronic heat capacity, V_{bias} is the voltage bias across the sensor, $R(T)$ is the resistance of the sensor, n is the electron-phonon power law exponent, κ is a coupling coefficient, and T_s is the temperature of the substrate. Depending upon the model, n is between 4 and 6. In the temperature range our detector is operated, $n=5$ (electron-phonon decoupling)

and the temperature of the phonons in the W is nearly the same as the temperature of the substrate.

From equation 2.4, one of the biggest advantages of voltage biasing a TES sensor becomes apparent. The Joule heating term (first term) provides negative feedback which allows for stable self-biasing within the sensor's superconducting transition. Other advantages of running with negative electrothermal feedback are described elsewhere [22, 20].

When energy from a particle interaction is coupled into the ETF-TES, the temperature of the electrons in the sensor rises. This causes an increase in the resistance, and consequently a reduction in the Joule heating. Because the slope of the R versus T curve for superconductors is steep for superconductors in the middle of their transition, the dominant cooling mechanism is the reduction in Joule heating. The strength of this negative thermal feedback can be characterized by the dimensionless parameter, α :

$$\alpha = \frac{d(\ln(R))}{d(\ln(T))} = \frac{T}{R} \frac{dR}{dT} \quad (2.5)$$

We monitor the change in resistance by measuring the current flowing through the sensor at a constant voltage bias with a high speed SQUID array. The details of the measurement will be explained elsewhere.

Because the dominant cooling is via the reduction in Joule heating, we are also able to measure the amount of energy deposited into the sensor by integrating the reduction in Joule power over time.

2.2.2 Quasi-particle Traps

For a detector based upon detecting athermal phonons, it is imperative to collect as much of the phonon signal before it thermalizes. This requires that much of the surface area of the absorber(detector) be instrumented, so that when an athermal

phonon reaches the surface the probability of being absorbed in the sensor is improved. For small devices, covering a large fraction of the surface with W is possible. However, for dark matter detectors of larger mass, instrumenting large areas with W is not feasible because of the increased heat capacity of the sensor.

The solution our group has developed involves the use of quasi-particle traps with Transition Edge Sensors [27, 22, 21] . In the solution described in this work, we place large pads of superconducting aluminum in electrical contact with a tungsten meander. When phonons of sufficient energy ($E > 2\Delta_{Al} \approx .36meV$) hit the superconducting aluminum, they can break Cooper pairs, forming quasi-particles. These quasi-particles relax towards the aluminum gap edge, releasing more phonons. If these phonons are sufficiently energetic, they can break more Cooper pairs and form more quasi-particles. These quasi-particles diffuse into the W film where they can deposit their gap energy into the W electron system. A graphical explanation of the process appears in figure 2.2 . The quasi-particle trap design must be chosen so that the quasi-particle diffusion time into the tungsten is much shorter than the quasi-particle recombination time or other quasi-particle loss time constants. This proved to be challenging as we scaled the detectors up in size.

2.2.3 Noise

One of the great advantages of using ETF-TES sensors is the effective suppression of the Johnson noise contribution to the overall noise of the sensor [22, 20] . By extending equation 2.4 to include the johnson noise and phonon noise contributions, one finds that the spectral density of the current noise in the limit of extreme feedback is given by

$$I_{\omega}^2 = \frac{4kT_o}{R_o} \frac{\left(\frac{n^2}{\alpha^2} + \omega^2\tau_{eff}^2\right)}{1 + \omega^2\tau_{eff}^2} + \frac{4kT_o}{R_o} \frac{\frac{n}{2}}{1 + \omega^2\tau_{eff}^2} \quad (2.6)$$

In practice, there are additional sources of noise which must be considered. Figure

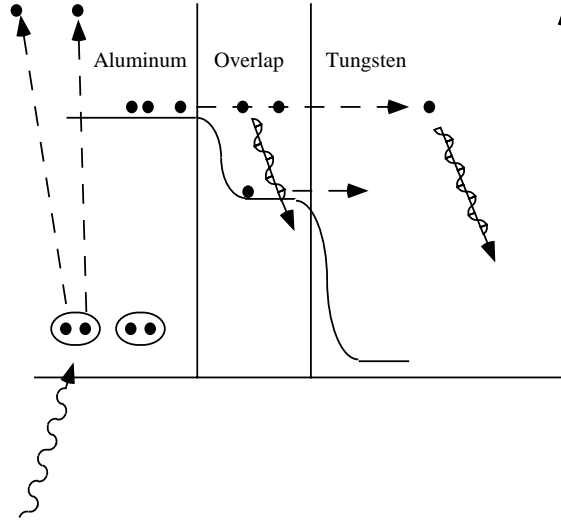


Figure 2.2: A phonon is shown incident upon the Cooper pairs in the Aluminum. The quasiparticles relax to the superconducting gap emitting phonons and breaking more Cooper pairs. Some of the quasiparticles diffuse across the boundary and interact with and deposit energy which is measured into the electrons in the tungsten and others emit phonons (energy which is not collected) into the substrate

2.3 is a schematic of the biasing and readout scheme implemented for the phonon sensors. Figure 2.4 is a schematic with the additional Johnson noise and SQUID noise terms added. From the schematic, it is straightforward to derive the additional noise terms,

$$\begin{aligned}
 i_n^2 = & \frac{4kT_s}{R_s} \left(\frac{R_s}{R_s + R_p + R_{bias}} \right)^2 + \frac{4kT_p}{R_p} \left(\frac{R_p}{R_s + R_p + R_{bias}} \right)^2 \\
 & + \frac{4kT_{bias}}{R_{bias}} \left(\frac{R_{bias}}{R_s + R_p + R_{bias}} \right)^2 + \frac{4kT_B}{R_B} \left(\frac{R_B}{R_B + R_{bias} \parallel (R_p + R_{bias})} \right)^2 \\
 & + i_{SQUID}^2.
 \end{aligned} \tag{2.7}$$

In general, the optimal noise performance in terms of signal to noise ratio is obtained when all the noise terms contribute equally.

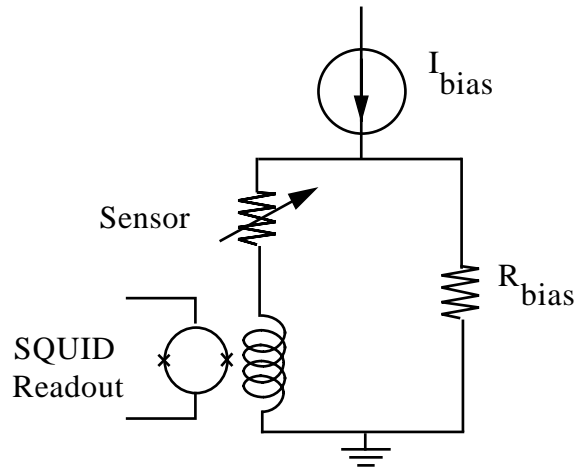


Figure 2.3: Schematic of the circuit used to voltage bias and readout a QET sensor.

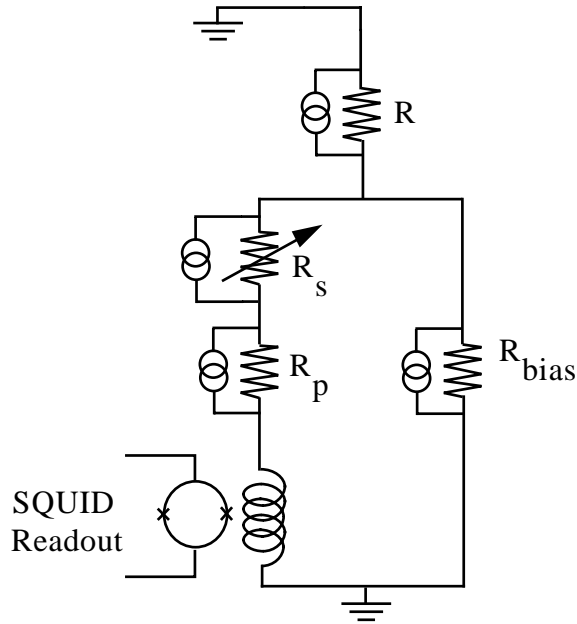


Figure 2.4: A schematic which describes the johnson noise sources in the circuit to bias the phonon sensors. Each resistor has a Norton equivalent current noise source in parallel.

2.2.4 Discussion of Time Constants

There are many sets of time scales involved in Quasi-particle trap assisted ETF-TES (QET) sensors that must be considered when designing a dark matter detector. At the dark matter detector level, the set of three time constants involved are phonon collection time, quasi-particle diffusion time, and electrothermal feedback time. Because of the speed of the TES with ETF, variations in pulse shape occur as a result of variations in phonon and quasi-particle arrival times. In general, every effort was made to decrease the phonon and quasi-particle collection times. There are two primary reasons. The first is that any scheme which can collect phonons or quasi-particles more quickly will improve the overall collection efficiency by reducing losses to mechanisms which occur on longer time scales. The second is that low frequency noise becomes more of a problem because of the longer integration time necessary with longer collection times.

Figure 2.5 is an example of pulses from a $\frac{1}{4}$ g detector. On this device there were four QET sensors patterned on one surface. A sketch of the device appears in figure 2.6. The decay times are very similar and $\sim 60 \mu\text{sec}$. There is variation in the leading edges of the four phonon pulses which is a result of the variation in the phonon flux arrival time at each of the sensors. This variation can be used to extract position information about the initial particle event and will be discussed in more detail later.

A set of time constants which were considered in detail in designing QET sensors involves the coupling of energy from the quasi-particle traps to the W-TES. Figure 2.2 is a diagram of the flow of energy from the production of quasi-particles in the aluminum collection fins to the coupling of energy to the W electron system.

If an athermal phonon is of sufficient energy and is absorbed in the Aluminum, it will break Cooper pairs and form highly energetic quasi-particles. The energy of these

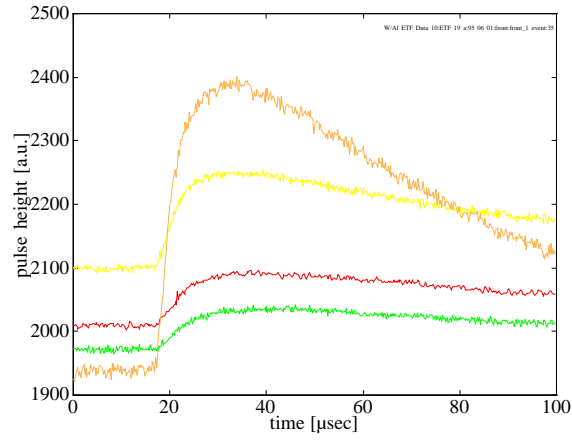


Figure 2.5: Example of pulses from four phonon sensor on a $\frac{1}{4}$ g substrate.

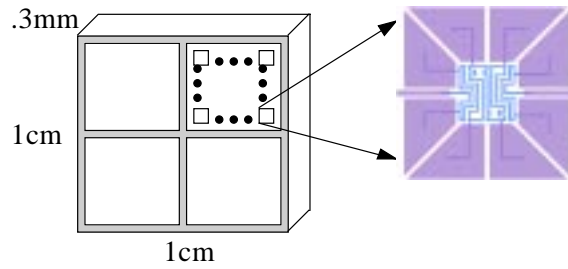


Figure 2.6: Sketch of the $\frac{1}{4}$ g device

quasi-particles will relax towards the superconducting gap of aluminum and release phonons. If the energy of the phonons is greater than twice the gap of aluminum, the phonons can break more Cooper pairs and generate more quasi-particles. If the phonon energy is less than $2\Delta_{Al}$, the phonon is lost back to the substrate. The losses due to sub 2Δ phonons is approximately 50% [4] .

The lifetime of quasi-particles has been estimated by Kaplan et al [25] and measured empirically by others [4, 15, 44] . The lifetime has been found to be extremely sensitive to film quality. For a sensitive dark matter detector, the quasi-particle collection time must be much shorter than the quasi-particle lifetime. The collection time is dependent upon device geometry as well as film quality. Results from scaling up our detectors and the effects on quasi-particle collection efficiency is also discussed later in this work.

A critical region of the QET sensor is the overlap between the W and the Al. At the Al/W interface, there can be additional loss due to phonon emission in the suppressed gap of the proximitized aluminum. Consequently, it is important to minimize the time spent by the quasi-particles in this region. Once the quasi-particles have diffused through the overlap region into the W, they quickly scatter off the electrons in the W. In the W, the electron-electron scattering is 100 times bigger than the electron-phonon scattering rate [6] . Consequently, most of the quasi-particle energy is deposited into the W electron system.

The electrothermal feedback time is also an important consideration in the design of the QET sensors. As Kent Irwin described in earlier work [22] , the inductance of the SQUID input coil which is used to measure the current in the tungsten and the heat capacity of the tungsten can store energy out of phase with each other. If there isn't sufficient damping there are oscillations. These oscillations are referred to as "electrothermal oscillations". By linearizing the differential equations describing the thermal and electrical system in a QET sensor, we can derive and estimate for the

criteria for oscillations.

To derive the criteria for oscillations, we start with the following two equations:

$$c_v \frac{dT}{dt} = \frac{V_{bias}^2}{R(T)} - \kappa(T^n - T_s^n) \quad (2.8)$$

and

$$L \frac{dI}{dt} + iR = V_{bias} \quad (2.9)$$

where L is the inductance of the SQUID input coil. Linearizing around the operating point, we get the following coupled first order differential equations:

$$c_v \dot{\delta T} = 2i_o R_o \delta i + \left(i_o^2 \frac{\alpha_o R_o}{T} - g \right) \delta T \quad (2.10)$$

$$L \dot{\delta i} = -i_o \alpha_o \frac{\delta T}{T} R_o - (R_o + R_{bias}) \delta i \quad (2.11)$$

where δi and δT are the current and temperature excursions around the operating points i_o and T respectively, g is the thermal conductivity to the substrate, and R_{bias} is the source resistance of the voltage bias source. The equations can be written in a more compact form by using the following notation:

$$\frac{1}{\tau_{eff}} = \frac{\frac{i_o^2 R_o \alpha_o}{T} - g}{c_v} \quad (2.12)$$

$$\frac{1}{\tau_{el}} = \frac{R_o + R_{bias}}{L}. \quad (2.13)$$

Using the expressions for τ_{eff} and τ_{el} , the coupled differential equations can be written as

$$\dot{\delta T} = \frac{1}{\tau_{eff}} \delta T + 2 \frac{i_o R_o}{c_v} \delta i \quad (2.14)$$

$$\dot{\delta i} = -\frac{i_o R_o \alpha_o}{LT} \delta T - \frac{1}{\tau_{el}} \delta i. \quad (2.15)$$

The criterion for oscillations can be derived by determining the criterion for imaginary eigenvalues to the matrix

$$M = \begin{pmatrix} \frac{1}{\tau_{eff}} & 2\frac{i_o R_o}{c_v} \\ -\frac{i_o R_o \alpha_o}{LT} & -\frac{1}{\tau_{el}} \end{pmatrix}. \quad (2.16)$$

In the limit of $R_{bias} \ll R_o$ and extreme electrothermal feedback, criterion for oscillation becomes

$$3 - \sqrt{8} < \frac{\tau_{etf}}{\tau_{el}} < 3 + \sqrt{8}. \quad (2.17)$$

This criterion places an upper limit on τ_{el} . As a result, for a given SQUID input coil inductance, there is a lower limit on the operating resistance. If the resistance is too low, the electrical time constant, τ_{el} becomes comparable to the electrothermal feedback time, τ_{etf} and the system starts to oscillate.

2.2.5 ETF Stability

In the QET sensors described in this work, quasi-particles from the Al collection pads are injected at various points along a voltage biased W-TES. A more complete expression to describe the temperature evolution of a TES which includes spatial dependence is given by

$$c_v \frac{dT}{dt} = g \nabla^2 T + i^2 r(T, x) - \kappa(T^n - T_s^n) \quad (2.18)$$

where temperature T is a function of position and time, g is the thermal diffusivity of the W, i is the current flowing through the sensor, and r is the resistance density. For simplicity, I will only consider the 1D case.

Ideally, one designs the sensor so that at the operating point, the temperature is a constant as a function of position. At the aluminum voltage rails, $\frac{\partial T}{\partial x} = 0$

because the thermal conductivity into the aluminum is very poor. If one assumes the previous two statements and linearizes the superconducting transition in the near the operating point, it is possible to explore the stability of the stability of equation 2.18 .

Assume the temperature can be expressed as $T + \delta T$ where T is the quiescent operating temperature. Equation 2.18 becomes

$$c_v^\lambda \frac{d(T + \delta T)}{dt} = \kappa^\lambda \nabla^2 (T + \delta T) + i^2 r - \Sigma^\lambda ((T + \delta T)^n - T_s^n). \quad (2.19)$$

where r is a function of T and position. The Joule heating term in the previous equation can be approximated by

$$i^2 r = i_o^2 r_o + 2i_o r_o \delta i + i_o^2 \delta r \quad (2.20)$$

This leads to

$$c_v^\lambda \frac{d(\delta T)}{dt} = \kappa^\lambda \nabla^2 (\delta T) + 2i_o r_o \delta i + i_o^2 \delta r - \Sigma^\lambda n T^{n-1} \delta T. \quad (2.21)$$

Using Ohm's law leads to an expression for δi :

$$i = \frac{V}{R} \Rightarrow \delta i = -\frac{V}{R^2} \delta R. \quad (2.22)$$

where R is the total resistance of the TES. By using the definition of alpha (equation 2.5) and assuming alpha is constant near our operating point, we can write

$$\delta R = \int \delta r \, dx \quad (2.23)$$

$$\delta r \approx r_o \alpha_o \frac{T}{T_o} \Rightarrow \quad (2.24)$$

$$\delta R = \alpha_o \frac{r_o}{T_o} \int T \, dx \quad (2.25)$$

Equation 2.21 now becomes

$$c_v^\lambda \frac{d(\delta T)}{dt} = \kappa^\lambda \nabla^2 (\delta T) - 2i_o^2 \frac{r_o^2}{R_o} \frac{\alpha_o}{T_o} \int \delta T dx + i_o^2 r_o \frac{\alpha_o T}{T_o} \delta T - \Sigma^\lambda n T^{n-1} \delta T. \quad (2.26)$$

At this point, it is useful to notice two things. The first item is that three terms, the first, second, and last, contribute to a stable solution i.e. when there is a sudden change in temperature δT those three terms cause T to return towards T_o . The second item is that the second term does not contribute to first order to the solution of the differential equation in the 1D case. In fact, by considering only the first order corrections, the spatial solutions for the temperature T must be a linear combinations of sines and cosines. By using the boundary condition that there is no heat flow accross the boundary, we have restricted the solutions to have a form such that the

$$\int \delta T dx = 0. \quad (2.27)$$

In one dimension, equation 2.26 simplifies to

$$c_v^\lambda \frac{d(\delta T)}{dt} = \kappa^\lambda \frac{d^2(\delta T)}{dx^2} + \left(p_o \frac{\alpha_o T}{T_o} - \Sigma^\lambda n T^{n-1} \right) \delta T, \quad (2.28)$$

where p_o is the power dissipated per unit length by the meander. Using separation of variables and the boundary conditions,

$$\delta T = \sum_m A_m e^{-\frac{t}{\tau_m}} \cos \left(\left(\frac{m\pi}{l} \right) x \right), \quad (2.29)$$

where l is the length of the meander. For stable solutions, all of the τ_m must be less than 0. This occurs if

$$-\kappa^\lambda \left(\frac{m\pi}{l} \right)^2 + \frac{p_o \alpha_o}{T_o} - n \Sigma^\lambda T_o^{(n-1)} < 0. \quad (2.30)$$

In steady state where we assume that the meander is an isotherm, we know that the Joule heating term equals the electron-phonon decoupling term,

$$p_o = \Sigma^\lambda (T^n - T_s^n). \quad (2.31)$$

For $T^n \gg T_s^n$, the constraint can be approximated by

$$-\kappa^\lambda \left(\frac{m\pi}{l} \right)^2 + \frac{p_o}{T_o} (\alpha_o - n) \quad (2.32)$$

$$\Rightarrow \frac{p_o}{T_o} (\alpha_o - n) < \kappa^\lambda \left(\frac{m\pi}{l} \right)^2 \quad (2.33)$$

$$\Rightarrow \frac{(\alpha_o - n)}{n (m\pi)^2} < \frac{\kappa^\lambda}{g_{ep}^\lambda}. \quad (2.34)$$

In the last line we have approximated $\frac{np_o}{T_o}$ with the thermal conductivity between the electrons and phonons per unit length, g_{ep}^λ . We can also write the thermal diffusivity, κ^λ in terms of the thermal conductivity of the meander. For simplicity, assume the thermal conductivity is determined by the Wiedeman-Franz law. We can now write the constraint as

$$\frac{g_{wf}}{g_{ep}} > \frac{\frac{\alpha_o}{n} - 1}{(m\pi)^2} \quad (2.35)$$

2.3 Ionization Sensors

2.3.1 Circuit

The ionization measurement is similar to the method used with conventional semiconductor detectors. A schematic is shown in figure 2.7. In the detectors we fabricated with ionization sensors, an electrode is deposited on the side opposite the phonon sensors. The electrode is usually a 30 nm layer of Au with a 10 nm palladium sticking layer. A sketch of a typical 1/4 gram or 4 g is shown in figure 2.8. For the

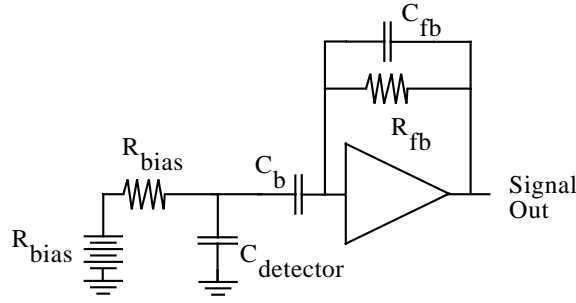


Figure 2.7: Schematic of the Ionization bias and readout circuit.

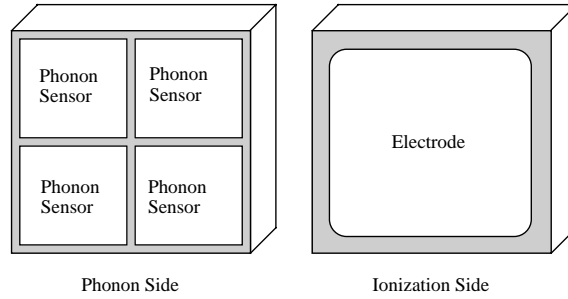


Figure 2.8: Sketch of prototype detectors with phonon and ionization sensors.

100 g detector, two ionization electrodes were patterned on the backside as shown in figure 2.9. On the phonon side, a W film was left along the perimeter to form a good outer ground electrode. In the large detector, there are two sets of electrodes. The outer electrode is used to reject events close to the edge of the detector which may have poor charge collection due to fringing fields associated with the sides of the detector.

2.3.2 Noise

Unlike previous work done by our group, the data in this thesis uses a charge amp to measure the ionization signal. For discrimination at low recoil energies, the noise of the ionization signal may be the limiting factor. To estimate the size of the noise, consider the schematic drawn in figure 2.10. This is a simplified drawing of noise and signal sources in the charge amp circuit. Under the ideal op-amp approximations

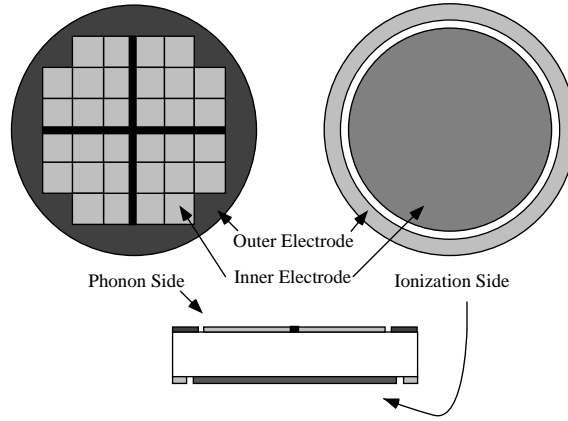


Figure 2.9: Sketch of the first 100 g Dark Matter detector.

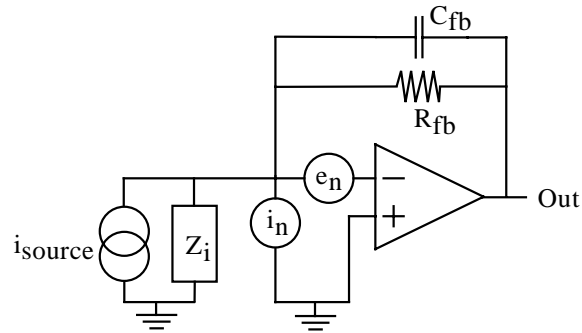


Figure 2.10: Ionization circuit for noise analysis which is dominated by the front end FET noise, v_n and i_n

that the open loop gain of the op-amp is infinite and voltage across the two input terminals is zero, the Laplace transform of the output signal can be written as

$$v_{out} = \frac{R_{fb}}{1 + R_{fb}C_{fb}s} i_{signal}. \quad (2.36)$$

A detailed discussion of the charge amplifier appears in Appendix A. In Appendix A, I show that the voltage noise e_n contribution to the output is given by

$$v_{e_n} = \frac{R_{fb}(C_i + C_{fb})s + 1}{R_{fb}C_{fb}s + 1} e_n \quad (2.37)$$

where the input impedance, Z_i , is treated as an input capacitance, C_i . The current noise, i_n , contribution is simply

$$v_{i_n} = \frac{R_{fb}}{1 + R_{fb}C_{fb}s} i_n. \quad (2.38)$$

In our case, $v_{e_n} \gg v_{i_n}$. Assuming a detector capacitance of 100 pF, a gate capacitance of 50 pF, a voltage noise of $1 \text{ nV}/\sqrt{\text{Hz}}$, the noise will be $\sim 200 \text{ eV FWHM}$. In practice, this is a very difficult performance to achieve because of microphonics.

2.3.3 Charge Trapping

When the silicon based detector is cooled down, it was found to operate in two distinct modes which group has called mode I and mode II [33, 34, 27]. Mode I describes the state of the crystal when it is initially cooled down. At temperatures below 1K, there are no thermally excited free carriers. In fact, it is energetically favorable for the donor and acceptor impurities to be ionized. If for example the silicon is p-type, then at low temperatures n_D of the acceptors and donors where n_D is the density of donor impurities per cubic centimeter will be ionized. $n_A - n_D$ of the acceptors sites will be neutral and overall the crystal will be neutral. The ionized

sites, however, pose a problem. When a particle interaction occurs and generates electron-hole pairs, these ionized sites can trap carriers of the opposite sign. At detector operating temperatures, these trapped charges will not be thermally re-emitted. Consequently, the amount of charge collected at the electrodes is reduced.

The other mode of operation, mode II, occurs when most of the charge trapping sites are filled. In this mode, the crystal is in a long lived non-equilibrium state. There are two ways we commonly use to get into this state. Mike Penn and previous members of our group used long exposures to ionizing radiation. In my work, I initially used to expose the detector to a strong source, but quickly moved to using an LED operated cold.

2.4 Fabrication

The fabrication of the phonon sensors requires photolithographic techniques. A variety of exposure masks for the different metal layers in the various designs were generated using MAGIC and DRACULA. The device fabrication was done in the class 100 clean room facility at the Center for Integrated Systems (CIS) at Stanford University. The actual processing steps are described in Irwin's thesis [22]. Barron Chugg, Roland Clarke, Paul Brink, and Betty Young have been refining the processing further.

Chapter 3

Experimental Apparatus

The superconducting transition temperature of the Tungsten used in the phonon sensors is between 70-100 mK. Therefore, we use a dilution refrigerator to cool the detectors. For the small prototype detectors (2 cm x 2 cm x 4 mm or smaller), an Oxford Instruments Kelvinox-15 was used. For the 100 g detector, we used the large 75 μ W refrigerator in the Center for Particle Astrophysics at the University of California, Berkeley.

The Kelvinox-15 has a base temperature near 40 mK. It was commissioned with much effort by previous members of this research group, K. Irwin and B. Chugg. The sample stage and cryogenic electronic mounts were made from OFHC copper and were gold-plated. The gold plating was done without nickel underplating to reduce stray magnetic fields.

The refrigerator is small and is lowered by hand into a glass dewar set. Because of its small size, multiple cooldowns can be accomplished in a long working day, pictures of the fridge and dewar set is in figure 3.1. In the center of the picture on the left side is of the KO-15 held up in a probe stand. In the picture on the right, the tall black object is a anodized aluminum probe stand which hold a glass dewar set.



Figure 3.1: Picture of the Kelvinox 15, KO-15.

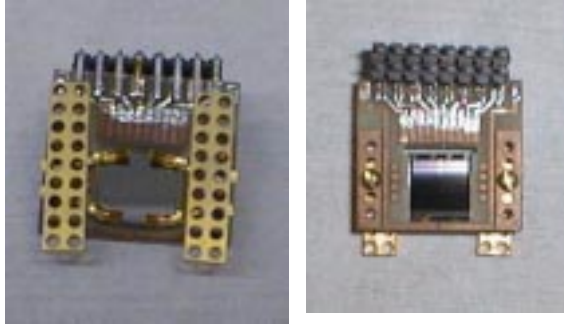


Figure 3.2: Photograph of a mounted 1 cm x 1 cm x 1 mm device

Around the glass dewar set and hidden by the probe stand is an annealed and de-gaussed mu-metal shield. Several layers of niobium foil are wrapped around the brass IVC of the KO-15 to further reduce magnetic fields at the detectors and cryogenic electronics. Also pictured is a protective stack of lead bricks which surround the fridge and dewar set. There is a hole bored through the stack to allow placement of an external radioactive source close to the dewar and detectors.

The prototype detectors were mounted in specially designed holders which were attached to the sample stage mounted at the mixing chamber. An example of a holder for a 1 cm x 1 cm device is shown in figure 3.2. Heat sinking of the detector is accomplished through the use of Au plated Cu-Be fingers. These Cu-Be fingers are commonly used to make electrical seals in screen room doors.

3.1 Electronics

Much of my time as a graduate student has been spent understanding and building up the electronics for these detectors. The most critical ingredient has been the recent development of high-bandwidth dc-SQUID systems to measure fast current pulses. We entered into a collaboration with people from NIST (John Martinis) and HYPRES Corporation (Rick Welty and Masoud Radparvar) to develop high speed SQUID arrays for our application. Our target goals were $1\text{ pA}/\sqrt{Hz}$ input noise with a bandwidth of 1 MHz. The input coil inductance also needed to be close to $0.25\text{ }\mu\text{H}$ to maintain a fast rise time.

Typical dc-SQUID systems involve the use of a single dc-SQUID coupled to expensive room temperature electronics through a complicated impedance matching scheme which preserves the noise performance of the dc-SQUID. Usually, the SQUIDs are operated with some form of a lock-in technique at a frequency less than 100 kHz. This scheme severely limits the bandwidth. Welty and Martinis demonstrated that a series array of dc-SQUIDs operating coherently could be used to boost the signal by the number of SQUIDs in the array. By using an array of 100 SQUIDs, they were able to use conventional high-speed room temperature electronics to amplify the signal [45] .

As part of the collaboration, I setup a test facility for characterizing the performance of the SQUID arrays. Because of earlier work done by our research group (G. Park, C. Cunningham, M. Huber, and J. Tate) with low noise SQUID systems, an old liquid helium storage dewar dunk probe was available for converting into a test system for the SQUID arrays. A drawing of the probe appears in figure 3.3 .

A SQUID is mounted on a G-10 boat near the bottom of a 41 inch long, $\frac{7}{8}$ inch outer diameter stainless steel tube. The bottom of the tube is welded to a stainless cylinder. A $\frac{1}{4}$ – 20 stainless allen head screw attaches the tube to the G-10 boat

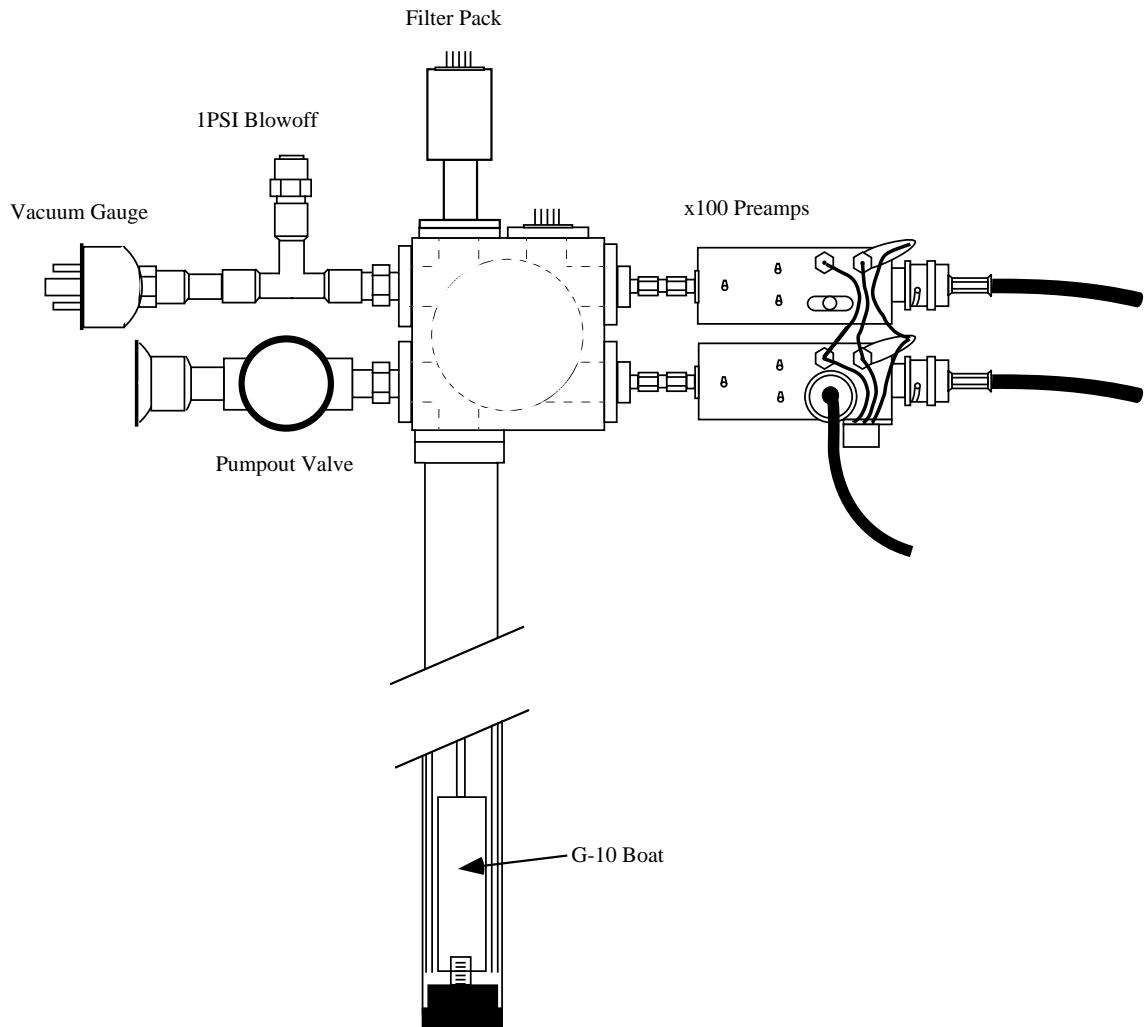


Figure 3.3: Sketch of the dunk probe for testing the SQUID arrays for use in a liquid Helium storage dewar.

assembly. A copper end cap fits over the allen head screw and makes an indium vacuum seal against the bottom of the cylinder.

The probe head is made from an aluminum block with a central cylinder hollowed out. Across the central tunnel via front and back covers which hermitically seal the block with viton O-rings. Eight other access ports are along the perimeter of the box. The stainless tube mentioned previously attaches to one of the side ports. On another side is a pair of hermetic SMA coaxial feedthroughs. On the opposite of the feedthroughs, a Varian 531 thermocouple gauge, a 1 psi blow off valve, and NW16 valve for pumping out the probe are attached. On the top side (opposite the SS tube), two nine pin hermetic connectors are used for additional slow speed wiring of the probe.

To cool the probe, the probe is pumped out with a mechanical pump below 50 mTorr. If the vacuum holds, approximately 2 Torr of helium exchange gas is added. The probe is then lowered slowly into a liquid helium storage dewar to cool the probe to 4 K.

To hold the SQUID chips for testing, I designed several chip holders as the SQUID chip designs evolved. An example of one of the chip holders is shown in figure 3.4. On the top a 50 mil spacing connector is attached. This board plugs into its mating connector on the G-10 boat. This connector is used to electrically connect the SQUID arrays to the coaxial lines, bias lines for single SQUIDs for two-stage SQUID amplifier mode, feedback lines for the single SQUID and array of SQUIDS, and heater coils. On the opposite end of the chip holder, there are copper pads for soldering wires to connect to the input coil. The wires for the input coils are twisted pairs and run up to one of the nine pine hermetic feedthroughs. On the backside of the chip holder, a $\frac{1}{4}$ in x $\frac{1}{4}$ in square is milled out for the placement of a small piece of niobium foil for magnetic shielding of the SQUID.

Each SQUID chip is fabricated with two sets of SQUID arrays. A sketch of a

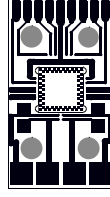


Figure 3.4: Sketch of the G-10 PC board used for holding the SQUID array chips.

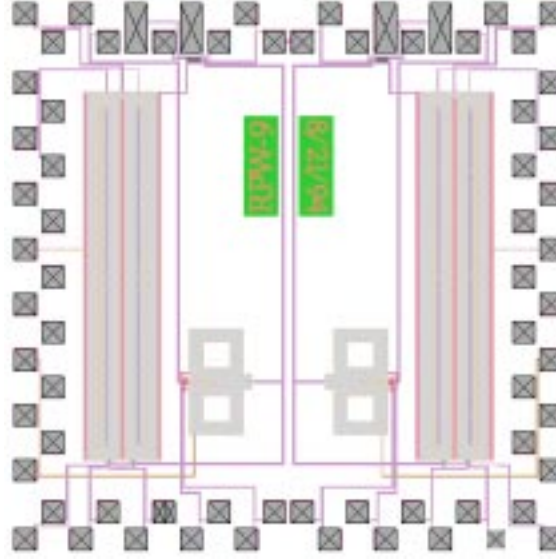


Figure 3.5: Picture of the SQUID array chip.

SQUID chip appears in figure 3.5. The small squares along the perimeter of the chip are bonding pads. The two long bars on the left and right side are the SQUID arrays. The figure 8 shaped devices are part of the single SQUID which is the input stage of a two stage SQUID system which is described later.

With the SQUID probe, we are able to measure the performance of both channels of SQUID arrays in a single cooldown. The room temperature electronics for the arrays were provided by John Martinis. They are directly mounted on the probe.

Figure 3.6 is a schematic of a SQUID array with the readout electronics. The arrays are operated with a constant current bias, and the corresponding voltage signal is measured. For a dc-SQUID, the amount of flux coupled to the SQUID loop alters the IV curve with a period of Φ_0 . Consequently, as shown in figure 3.7,

the voltage measured at a fixed current bias can vary between v_1 and v_2 . In this figure, the x-axis is zero offset by the current bias. The difference between v_1 and v_2 is known as the modulation depth. Current flowing through the input coil or feedback coil alters the amount of flux coupled to a SQUID linearly to first order. A voltage vs Φ ($V\Phi$) curve for a SQUID array is shown in figure 3.8. The modulation depth (amplitude of the $V\Phi$ curve) should grow linearly as the number of SQUIDs in the array. However, the presence of trapped flux near and in the array can alter the size and shape of the $V\Phi$ curve. The trapped flux can cause the signals from the individual SQUIDs in the array to be out of phase and consequently causing destructive interference or degradation of the $V\Phi$ curve. To remove the trapped flux, there are several options. The easiest option is to “zap” the SQUID array. There is a switch on the room temperature electronics which momentarily applies either two or five volts across the array. This process causes enough current to flow through the SQUIDs to drive the array normal and heat the SQUIDs above their T_c . Upon cooling some of the trapped flux may leave reducing the overall trapped flux and improving the $V\Phi$ curve. This extreme measure has been found to work rather well. It has been more effective than other alternatives. One alternative is to use the heater coil patterned on the chip to heat the SQUIDs above their T_c . Another alternative is to raise the probe out of the liquid helium. If the probe is raised high enough, the probe warms about the T_c of the array. After the arrays become resistive, the probe is re-cooled slowly to reduce the amount of eddy currents which could cause trapped flux in the array.

Finding a suitably sized and smooth $V\Phi$ curve is known as tuning the SQUIDs. Once the SQUIDs have been suitably tuned, the noise performance can be measured. A sketch of the system to measure the noise is shown in figure 3.9. The noise is measured as a function of the current flowing through the input coil. The current through the coil is ramped through at least one Φ_0 . The current is provided by a

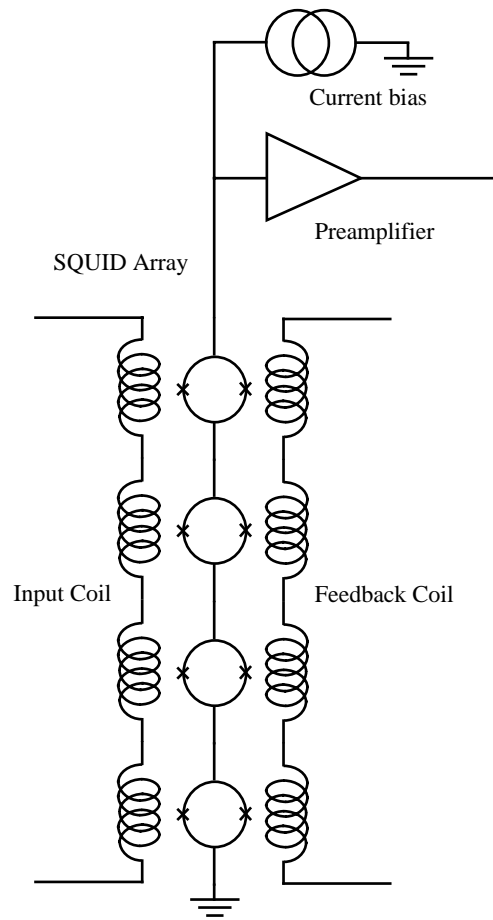


Figure 3.6: Schematic of the bias and readout of the SQUID arrays. The four SQUIDs represent the array which actually consists of at least 100 SQUIDs.

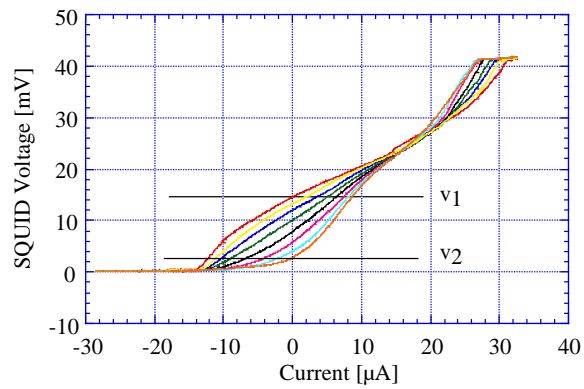


Figure 3.7: IV Curve of the SQUID array for various input currents.

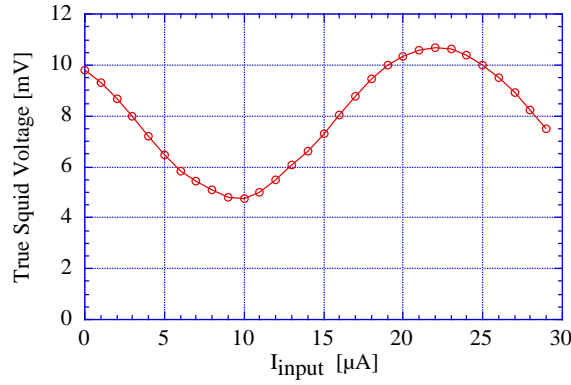


Figure 3.8: Typical $V-\Phi$ curve for a SQUID array.

low noise battery powered current source. The amount of current is controlled by a computer via a stepper motor connected to a knob on the current source. This mechanical coupling was done to reduce any rf noise generated by the computer from coupling into the Josephson junctions and being aliased down to lower frequencies. The voltage noise at each input current level is measured using an HP33565 Signal Analyzer. In addition, an IV curve for the SQUID array is recorded at each current level using a function generator and a PM3310 digital scope.

With this setup, we have been able to test many SQUID chips. Using the results of these tests, Rick Welty, et al. have been able to improve the design and performance of the SQUID arrays.

As mentioned previously, the SQUID chips have a single SQUID which can be used as the input stage of a two stage current amplifier [45]. By jumpering the appropriate pads on the SQUID chip using a wire bonder, one can form the two stage SQUID amplifier depicted in figure 3.10. The single SQUID first stage is voltage biased. This is in contrast to the SQUID arrays which are current biased. The voltage bias is accomplished using a small shunt resistor across the single SQUID and a current bias. The shunt resistor and the current bias keep the voltage across the SQUID constant. As the flux coupled to the single SQUID is varied by changing the current flowing through the input coil of the single SQUID, the current flowing

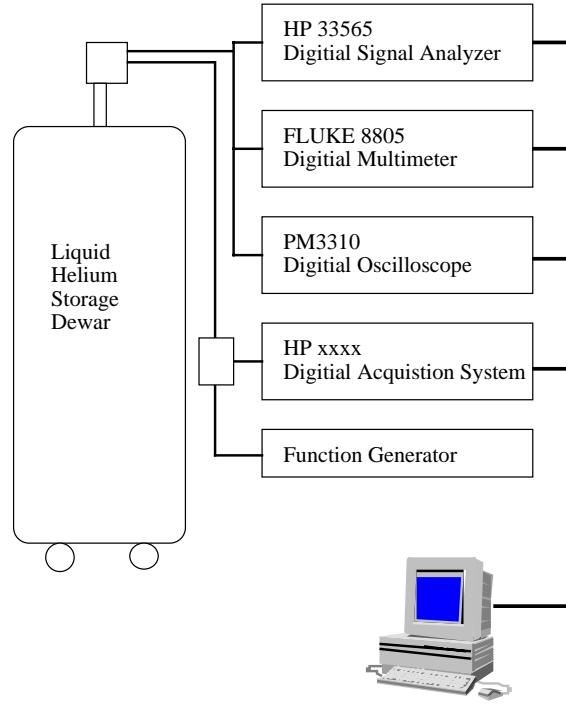


Figure 3.9: Schematic of the Instruments used and controlled to do a SQUID array noise measurement

through the single SQUID varies and is measured by the SQUID array. In essence the SQUID array acts as an impedance matching circuit to the room temperature electronics. With this system, the low noise performance of a single SQUID is easily achieved without complex and costly electronics. Operation of this system is straightforward and several noise measurements were done in this configuration. In general, the noise performance was slightly better than the SQUID arrays, however the added complexity of an additional bias line and dynamic range make this solution less attractive.

Figure 3.11 shows typical graphs which summarize the noise measurements of a SQUID array. The upper left curve is the $V\Phi$ curve. Below the $V\Phi$ is the voltage noise measurement by the spectrum analyzer at the output of the pre-amplifiers. The voltage noise is referenced back as an input current noise by calculating the $\frac{dV}{dI}$ from the $V\Phi$ curve. The resulting current noise is plotted in lower left corner

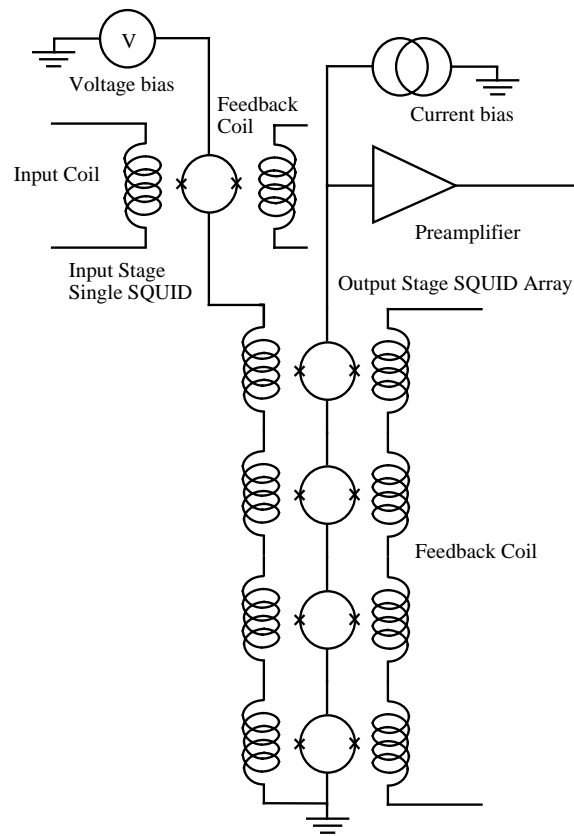


Figure 3.10: Schematic of the bias and readout scheme for the two-stage SQUID system.

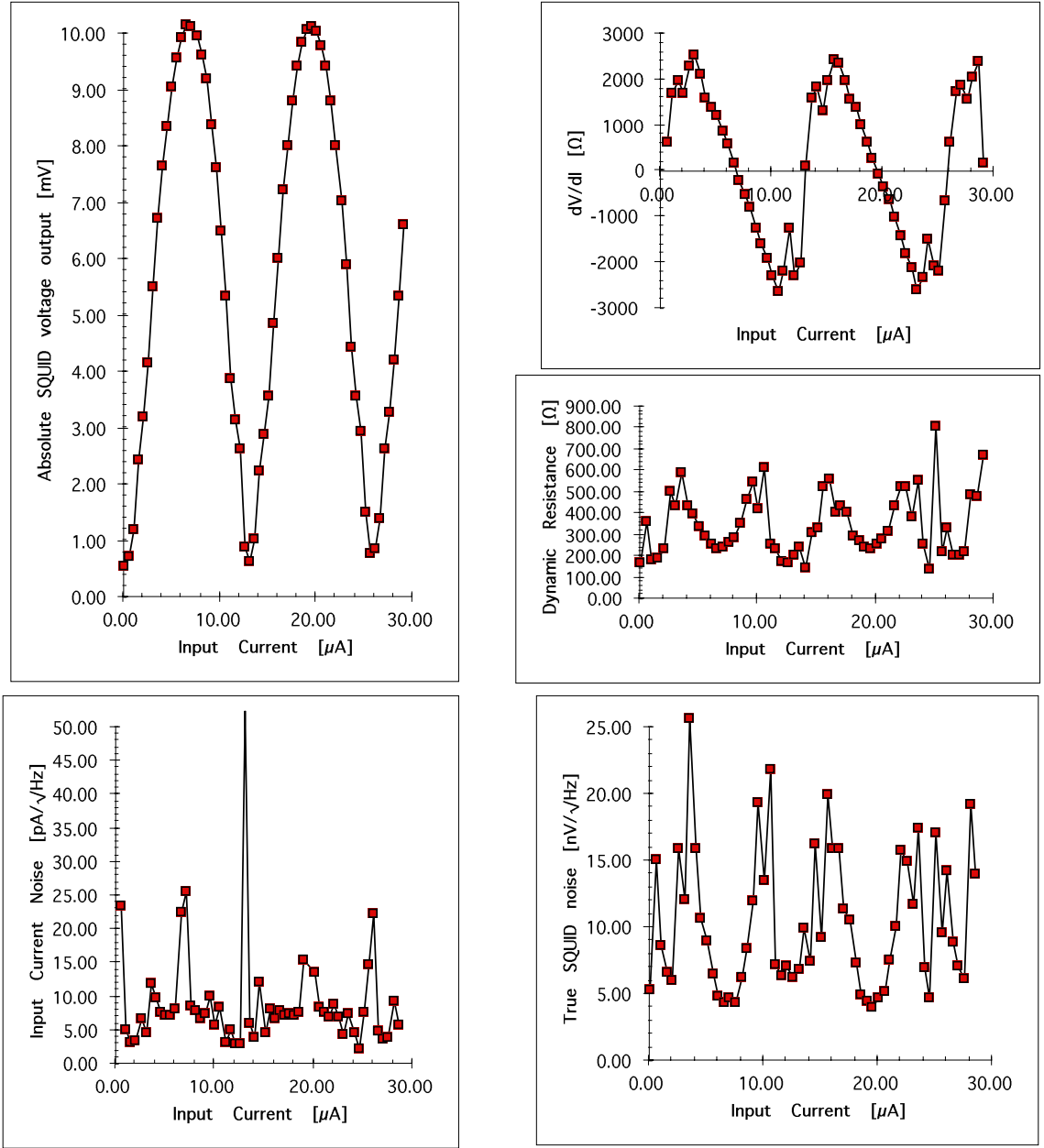


Figure 3.11: Example of the output of the LabView program in EXCEL format of a SQUID noise measurement.

of figure 3.11. The current noise appears to diverge then the $V\Phi$ curve are at its minimum and maximum.

For the two-stage device, the analysis is a bit more complex. The $V\Phi$ curve is considerably more complex. The simplest explanation is that it is a modulation of

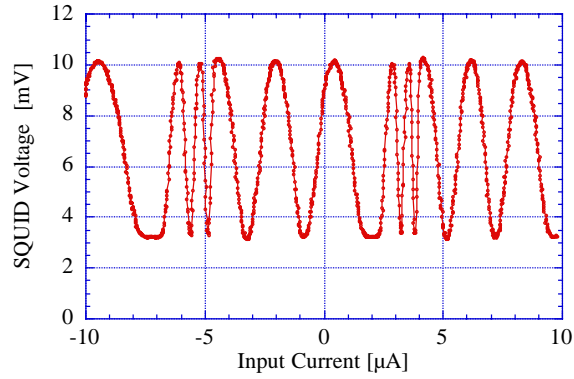


Figure 3.12: V - Φ curve of the two stage SQUID system. The V - Φ curve of the first stage SQUID is modulated by the V - Φ curve of the second stage SQUID array.

Current Bias [mA]	Current Noise [pA/ \sqrt{Hz}]
0.34	Not measured
2.46	2.3
3.4	1.9
4.2	2.7
5.48	3.0

Table 3.1: Summary of the Noise performance of a two-stage system

a modulation. Instead of measuring the noise at each input coil value, the noise is measured where the $V\Phi$ curve is the steepest. The higher slope tends to give the best noise performance. Figure 3.12 shows an example of a $V\Phi$ curve. The results of measurements of the noise at various points along the $V\Phi$ curve are tabulated in table 3.1 .

By testing a variety of SQUID array design ideas, improvements were made in the performance of these devices. More recently, Chad Fertig and Andrea Davies have made further improvements to the SQUID test probe. At the present time, we are able to use the setup to quickly test a SQUID chip and determine if its performance meets our requirements for use with a detector.

3.1.1 SQUID Electronics

The electronics for operating the SQUID arrays consists of two parts, a x100 preamplifier and a SQUID feedback unit. The preamplifier is actually a bit complicated. It consists of two gain stage amplifier to give a net gain of 100. The first stage uses a low voltage and current noise FET op-amp with a 1 Mhz bandwidth. In addition to the gain, the preamp unit contains the SQUID array current bias circuitry which has a source impedance of $\sim 20 \text{ k}\Omega$. The preamp also contains the necessary switches and voltage levels to “zap” the SQUID array. The feedback unit is used in conjunction with the feedback coil of the SQUID array to linearize the response of the SQUID. Unlike most conventional SQUID feedback systems which utilize a lock-in technique, this feedback system is analogous to an “op-amp” feedback. In any feedback system there is a summing node. In this case, it is at the SQUID loop(s). A sketch of the feedback system appears in figure 3.13. As current flows through the input coil, the SQUID electronics responds so that the current passing through the feedback coil exactly cancels the flux coupled into the SQUID loop by the input coil. The amount of current passing through the feedback coil depends upon the ratio of the coupling between the input coil and the SQUID loop and the coupling between the feedback coil and SQUID loop. Typically, we wire bond the SQUID arrays so that the feedback coil has a coupling which is $\frac{1}{8}$ of the input coil. As a result, the amount of signal feedback is $\frac{1}{8}$ which implies that the signal in the feedback coil is 8 times that of the signal in the input coil. Since, the output of the SQUID feedback unit is a voltage, the voltage generated at the output will be $8 \cdot R_{fb} \cdot i_{in}$. The noise performance of the system can be adjusted by changing the point on the $V\Phi$ curve which the feedback unit locks upon.

An important aspect of using the SQUID arrays is their high bandwidth. Figure 3.14 shows the response of the feedback system to a voltage step. The rise time

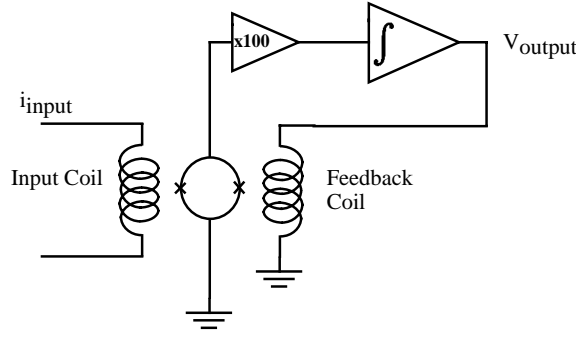


Figure 3.13: Diagram of the flux locked loop system for the SQUID arrays.

is of order 200 ns indicating a bandwidth around ≈ 1 MHz. From the schematics for the preamplifier and feedback unit, the room temperature SQUID electronics can be described by the schematic in figure 3.15. Using basic circuit analysis, the response of the system is given by

$$v_{out} = i_{in} R_{fb} \kappa \frac{100 f \left(\frac{R_1}{R_{int}} \right) \tau_{int} s}{100 f \left(\frac{R_1}{R_{int}} \right) \tau_{int} s + \frac{\kappa R_{fb} (s + \omega_o) \tau_{int} s}{\zeta}} \quad (3.1)$$

where κ is the ratio of the flux coupling between the input and feedback coil (which is typically 8 in our case), ω_o is the bandwidth of the x100 gain pre-amplifier, $\tau_{int} = R_{fb} C_{fb}$, and ζ is the transfer function of the SQUID array at the lockpoint, $\frac{dV_{out}}{dI_{in}}$. Using typical values one finds the bandwidth to be near 1 MHz.

3.1.2 Detector Biasing

To operate the QET phonon sensors, a constant voltage bias is required. This bias is accomplished by placing a small shunt resistor in parallel with the series combination of the SQUID input coil and phonon sensor and applying a current across the parallel network. This is depicted in figure 3.16. The shunt resistor R_b is $\approx 20 \text{ m}\Omega$, and the sensor resistance is anywhere between 0.25Ω and 4Ω . The current source is actually a voltage source in series with a $7 \text{ k}\Omega$ resistor. Since the

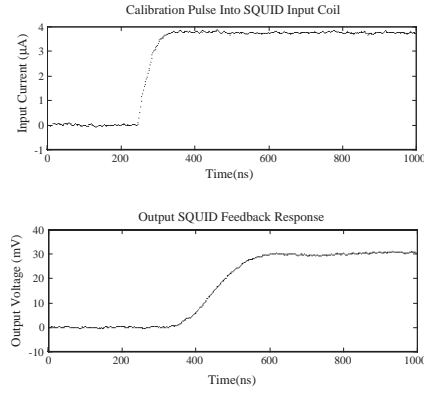


Figure 3.14: Step function response of the SQUID array with the flux feedback electronics.

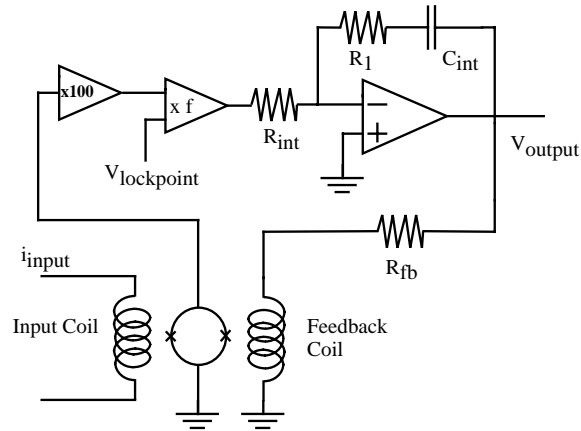


Figure 3.15: Simplified Schematic of the flux feedback circuit for the SQUID arrays.

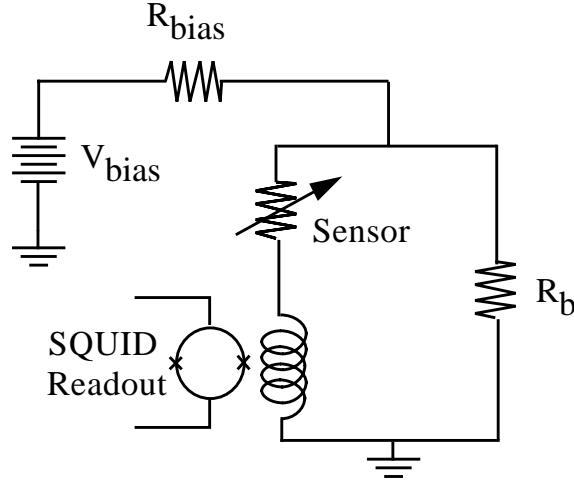


Figure 3.16: Schematic of the circuit used to voltage bias the phonon sensors.

$7\text{ k}\Omega$ resistor is $> 20\text{ m}\Omega$, the bias current is $\frac{V_{\text{bias}}}{7\text{ k}\Omega}$. At the present time, we are using voltage sources which utilize the LT1021-7V precision voltage reference and which can be controlled from 0 to 7 volts with 1000 steps.

3.1.3 SRS Amplifiers

Before the signals can be digitized by the data acquisition system (DAQ), the output from the SQUID feedback units must be amplified. However, the signal from the feedback units sits upon a DC offset which depends upon the feedback lock point and the quiescent current flowing through the sensor. This voltage level is typically between $\pm 0.5\text{ V}$. The signal of interest are small (mV) changes around this value. Consequently, we use SRS 560 amplifiers operating in their ‘A-B’ mode to subtract this DC offset and add gain. The SRS amplifiers can be AC-coupled if desired and also add filtering for anti-aliasing for the digitizers.

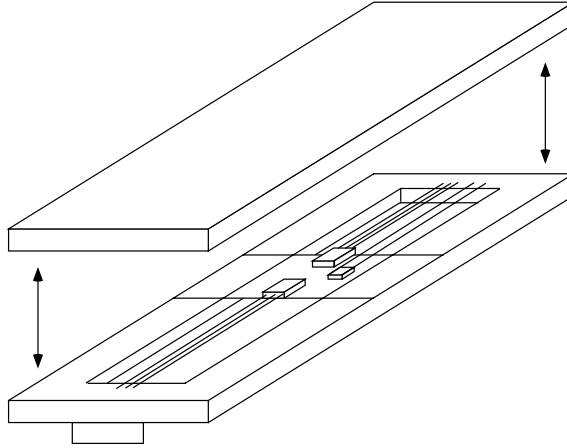


Figure 3.17: Sketch of the G-10/fiberglass enclosure to shield the FET radiation from the detector.

3.1.4 Q amplifiers

The charge amplifier consists of a cold Si-JFET coupled to an A250 charge pre-amplifier. The Si J-FET is a SONY 2SK152. It is housed in a G-10 enclosure mounted at the 1K pot. A sketch is shown in figure 3.17. The FETs are enclosed in G-10 to eliminate the infra-red radiation generated when they are operating. I found that attempts to operate the phonon sensors with unshielded FETs were difficult because the infra-red radiation would add a heat load to the sensor causing it to be driven normal.

3.2 Data Acquisition

3.2.1 Hardware

Most of the data presented in this thesis was taken with 12 bit 5 MHz VME COMET digitizers. The SRS amplifiers provided anti-aliasing filters. Each COMET has four channels of digitization which can each operate up to 5 Mhz. In the course of using these digitizers, we have found three flaws in the design which have yet to be

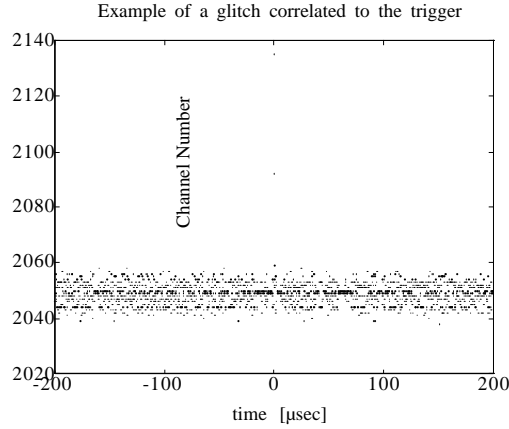


Figure 3.18: Glitch associated with triggering the COMETs.

corrected by the company. The first is the presence of a glitch in the signal measured by each digitizer whenever it is triggered. Figure 3.18 is an example of a glitch when the input is shorted. The time $t=0$ corresponds to the time of the trigger. Another problem is the presence of excessive noise present at the input of each channel when it is digitizing pretrigger information. Figure 3.19 is a plot of the trigger signal which is a square wave and the voltage measured at the input across a 50 resistor using a digital oscilloscope. Region A is the time when the COMET's are digitizing; and region B is the time when the digitizers are off. Apparently, the noise from clocking the digitizers is being fed into the front amplifiers of the COMETs. Figure 3.20 is a graph plot of the signal near the trigger pulse. The digitizers were programmed to stop 200 sec after the pulse. The final problem is the inaccuracy of the gains. The digitizers shipped from the manufacturer had a front end gain of 1.22 instead of 1. This mistake meant that the range of the digitizer was $\pm \frac{1}{1.22}$ instead of ± 1 . We have modified the front end circuit to correct this problem.

The triggering for the COMET digitizers was done by summing and shaping a second copy of the pulses from the SRS amplifiers. The shaped pulse was then put through a threshold detection module to generate a trigger. The summing, shaping, and trigger threshold logic were all accomplished using NIM modules.

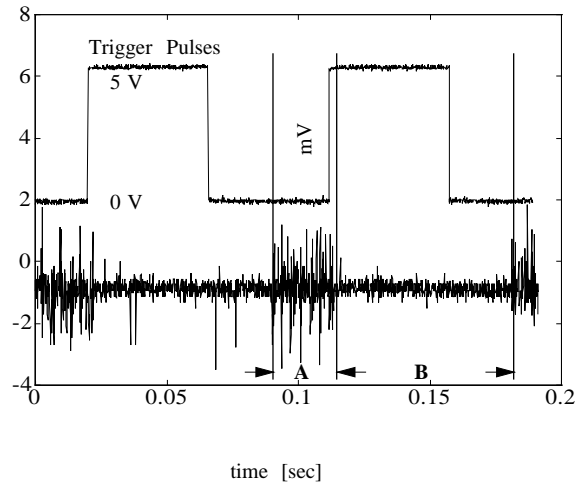


Figure 3.19: Noise induced by the COMET digitizers on the signal of interest on a long time base.

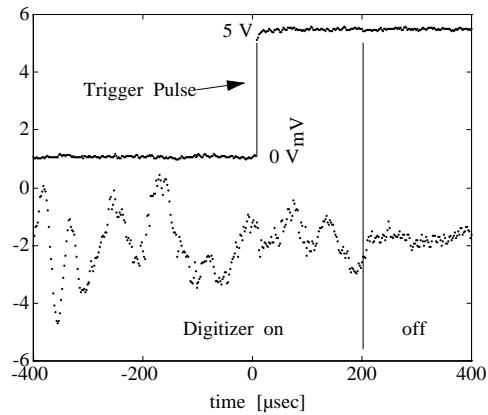


Figure 3.20: Detailed plot (short timebase) of the noise induced by the COMET digitizing.

Because of the problem of glitches and noise in some of the COMET digitizer channels, we only use two out of four the channels in a digitizer card. Most of the data runs required the use of two COMET digitizers. Unfortunately, I made an error in synchronizing the trigger for the data taken with two COMETs. I did not blank the trigger while the COMETs were being armed. Because I was not able to simultaneously arm the trigger for both COMETs, there are a class of recorded events which contains halves from two events. The COMETs are operated in a mode which disables them after receiving a trigger pulse. Because of the asynchronous arming, it is possible for an event to trigger one COMET before the second is armed. As a result, the recorded event is actually two halves of two events.

3.2.2 Software

The software for the DAQ is written in LabView. It is not a particularly elegant piece of code despite several redesigns. Within LabView, the digitizers and if neccessary multimeters and refrigerator temperature controller are setup and controlled. Despite LabView's inefficient use of CPU and memory resources on the DAQ computer, the DAQ program is able to generate cumulative diagnostic plots for immediate inspection to determine the quality of the data as it is collected. The output of the LabView programs are Matlab binary files for more detailed offline analysis.

Chapter 4

Detector Evolution

4.1 Quasiparticle Trap Demonstration

4.1.1 W/Al 2-channel device

In order to scale up a detector with a practical mass for a dark matter search, we must be able to use a larger size target material. However, in order to scale up in mass and maintain good energy and position resolution with TES sensors, a large fraction of the surface area of the detector has to be instrumented. Using large areas of tungsten is not practical because of decrease in sensitivity due to the increase in heat capacity.

However, as Irwin reported [22], it is possible to make devices which utilize quasiparticle trapping with tungsten transition edge sensors. In our device, large aluminum pads were electrically connected to an array of tungsten meanders. A sketch of part of a phonon sensor appears in figure 4.1. Athermal phonons from the initial event couple into the aluminum and create quasiparticles. The quasiparticles diffuse into the tungsten which is voltage biased in the middle of its transition. The quasiparticles from the aluminum interact with the electrons in the tungsten and

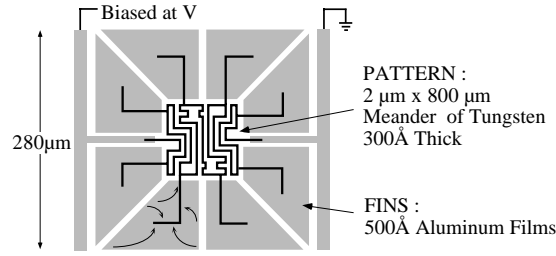


Figure 4.1: Single pixel of a QET phonon sensor

deposit energy in the tungsten's electron system. The resulting increase in electron temperature is observed as a drop in current flowing through the voltage biased tungsten meanders.

The results presented in this section are from a 2 channel W/Al device on a 1 cm x 1 cm x 1 mm silicon substrate. Each phonon sensor consists of 200 tungsten meanders electrically connected in parallel with a normal resistance near 2Ω . The meanders are $800\mu\text{m}$ long, $2\mu\text{m}$ wide, and 30 nm thick. There are eight quasi-particle traps connected to the meander at equally spaced intervals along the meander. The channels are each 2 mm x 4 mm and are spaced 5 mm apart center to center and are centered on the chip.

X-rays from an ^{55}Fe source were collimated into a line and were incident upon the backside of the detector. A sketch of the setup appears in figure 4.2 . Figure 4.3 is an example of the pulses in each channel for a 6 keV X-ray hitting the backside of the detector.

A useful feature of this type of phonon sensor, which utilizes extreme negative electrothermal feedback, is the ability to self-calibrate the sensor. Because the dominant cooling mechanism in the tungsten TES is the reduction in joule heating, the amount of energy deposited into the TES can be calculated by integrating the reduction in joule heating over the length of the pulse. In practice, low frequency noise places an upper limit on the maximum integration time before introducing additional noise.

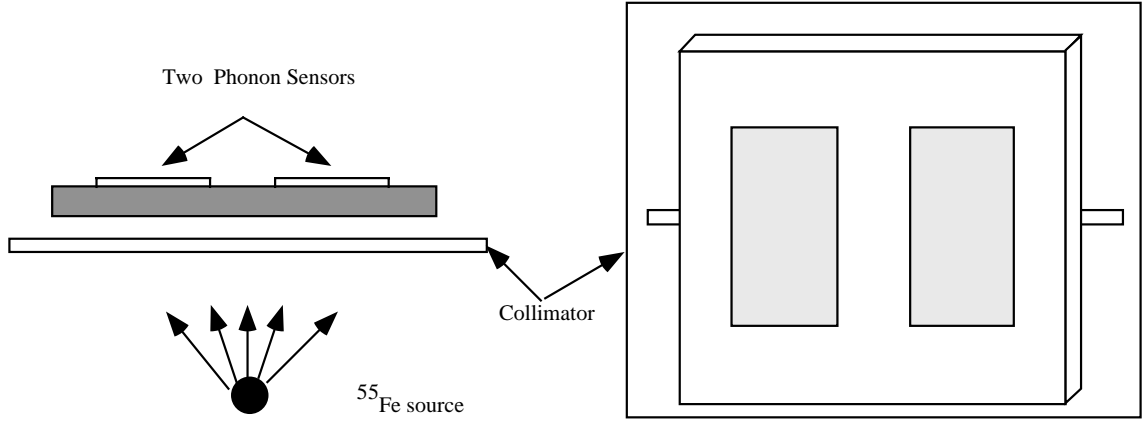


Figure 4.2: Sketch of the experimental setup of the detector and radioactive source

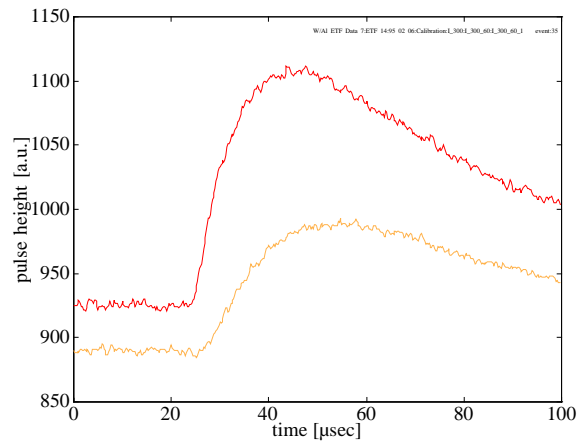


Figure 4.3: An example of pulses from the first demonstration of Quasiparticle trapping with ETF/TES sensors.

Figure 4.4 is a plot of the energy collected in one sensor versus the energy collected in the other for 6 keV X-rays hitting the backside of the detector. There are many interesting features in this picture. One interesting feature is that the total energy collected in the band of events from the 6 keV source is less than 6 keV. This discrepancy is a measure of the overall collection efficiency. There are several loss mechanisms. One loss term can be attributed to not collecting the athermal phonon energy in the aluminum films before the athermal phonon distribution is no longer sufficiently energetic to break Cooper pairs in the aluminum. A second related loss term is the emission of sub-gap phonons as the initial quasiparticles generated in the aluminum scatter within the aluminum generating phonons and more quasiparticles at the superconducting gap of Al. The phonons generated in the aluminum which are of energy less than $2\Delta_{Al}$ are emitted into the substrate and are not collected. The expected loss at this stage is approximately 50% [4]. There are further losses due to quasiparticle recombination and to local trapping as the quasiparticles in the aluminum diffuse towards the tungsten. At the Al/W interface, there is another inefficiency related to the transmission coefficient for the quasiparticles into the W. And finally, once the energy from the quasiparticles couples into the electron system of the W, there is a small inefficiency in the negative ETF collection. For example, for pulses which are a factor of 10 faster than the intrinsic time constant, only $\frac{10}{11}$ of the initial energy is measured/removed via ETF and $\frac{1}{11}$ is lost to the substrate.

Charge Trapping

One factor contributing to incomplete collection of the total deposited energy is the presence of charge traps in the silicon. When a particle interacts in the silicon substrate, the energy deposited generates phonons and electron-hole pairs. However, on short time scales, the electron-hole pairs can recombine and generate phonons which will also be measured by the sensor. It has been observed that our TES phonon

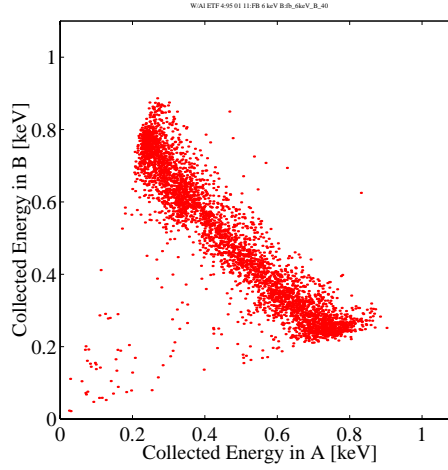


Figure 4.4: “A vs. B” plot for a two channel device. This demonstrates the partitioning of energy between the two phonon sensors.

sensors operate in two modes which differ in the density of charge trapping sites. When the silicon crystal is initially cooled down (mode 1), there is a distribution of ionized majority and minority dopant sites which are in thermal equilibrium. These ionized sites depending upon their polarity can trap an electron or hole before they recombine releasing only a fraction of its potential energy into the generation of phonon energy. Despite the high purity of the silicon substrate, the density of charge traps is high enough to significantly reduce the phonon signal. One method of neutralizing the ionized impurities is to expose the detector to a large amount of ionizing radiation. After a prolonged exposure, the silicon crystal is in long-lived metastable state (mode 2) in which nearly all the impurity sites have been neutralized. A previous graduate student, Mike Penn, and others have made detailed studies of the dynamics of mode 2 [34, 40] .

In Mike’s work, he used a strong radioactive source to neutralize his devices. For the development of dark matter detectors, this is not practical. The length of time and strength of source required quickly becomes prohibitive as the mass of the detector increases. Furthermore, a dark matter detector would be enclosed

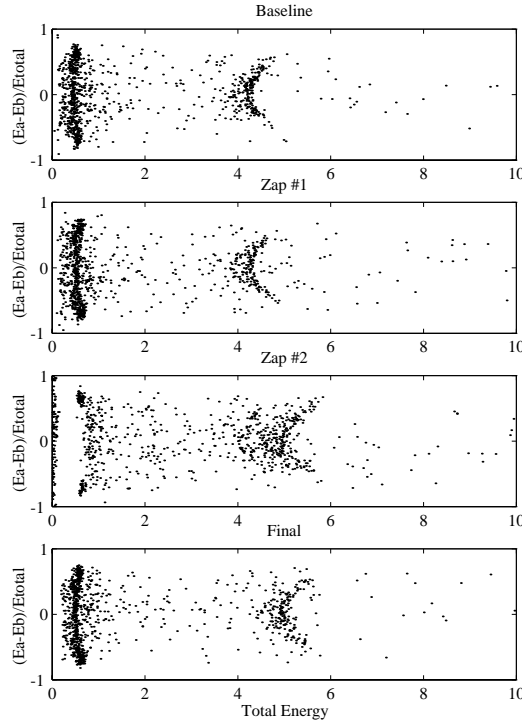


Figure 4.5: Partitioning of phonon energy between two sensors after different amounts of LED exposure. The upper most plot is before any LED exposure, the remaining plots are after more LED light exposure.

in an environment well shielded from ionizing radiation. From discussions with Betty Young and other research groups, we decided to try light from an LED to generate electron hole pairs. The LED choosen was bought from Radio Shack and has a forward voltage drop of 1.4 V at room temperature and 1.8 V at the detector operating temperature. In figure 4.5 , I've plotted the partitioning of energy between the two sensors $\frac{E_a - E_b}{E_{total}}$ as function of total collected energy for events from an ^{241}Am source after illuminating the detector with an LED for different amounts of integrated time. The disappearance of the lower peak and appearance of the second peak corresponds to the crystal going from mode 1 to mode 2.

Position information

Another feature in figure 4.4 is the slight curvature of the band of events from the ^{55}Fe source.

The slight curvature in figure 4.4 and strong curvature in the total energy collected versus energy partitioning in figure 4.5 is an indication of the position sensitivity in this type of athermal detector. When a pulse occurs between the two detectors, the energy is shared equally between the two detectors. Events which occur directly under one sensor lead to the maximum pulse height or collected energy in one sensor and a minimum signal in the other. When events occur further towards the edge, the energy from the event begins to be shared more equally between the two sensors. The deconvolution of the position information from the energy distribution is complicated because the data folds back on itself.

4.1.2 W/Al 2-channel device with Au heat sinks

Low frequency noise

One of the advantages of a sensor operating in extreme negative electrothermal feedback is that the signal can be integrated and yield the actual amount of energy removed via this mechanism. In fact, in the absence of low frequency noise, it is to one's advantage to integrate the signal for as long as possible. Figure 4.6 is a plot of the signal in sensor A versus the signal in sensor B. The signals were calculated in three different ways. In the left most plot, the signals from the sensors are determined by determining the peak height. Using the same data set as in the left hand plot, I calculated the integral of the signal. This appears in the right most plot. As one can see, the noise is much higher in the right most plot. In contrast, the plot in the middle was generated by calculating the integral of the signal above a certain frequency. In essence, the raw pulse data was AC coupled with a digital filter and

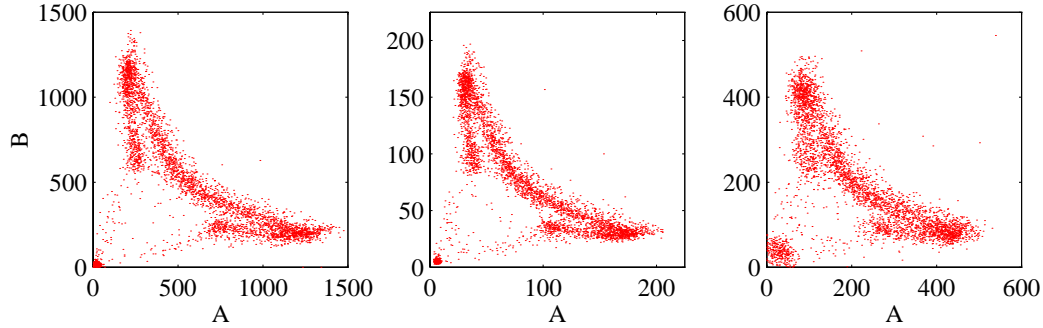


Figure 4.6: The three plots show the partitioning of energy between two phonon sensors calculated in three different ways. The left most plot is a plot of the pulse height in one versus the pulse height in the other. The middle and right plots are integrals of pulses in one versus the other. The middle plot has a shorter integration time the right plot. The units in the left plot are digitizer bins; the units for the middle and right plots are eV.

then integrated. For the data presented in this thesis, the “integrals” calculated are done in this way. Emperically, I have found that this gives the best energy resolution. Basically, the digital AC filtering reduces the sensitivity of the “integrals” to low frequency noise such as $1/f$ noise and AC line pickup.

Position Information

Figure 4.6 is another demonstration of the position dependence of the observed signal. The presence of Au pads on the backside of the sample are sites where the athermal phonons within the silicon can be absorbed or down converted below the collection threshold set by the Al quasiparticle collection fins. In this case the Au pads on the back side absorb enough phonons to remove the ambiguity between events towards the edge and events towards the middle of the crystal. For events towards the edge, more of the athermal phonons are absorbed by the gold before they can diffuse to the other sensor. As a result, there is a drop in collected energy for events which fold back in the energy partitioning.

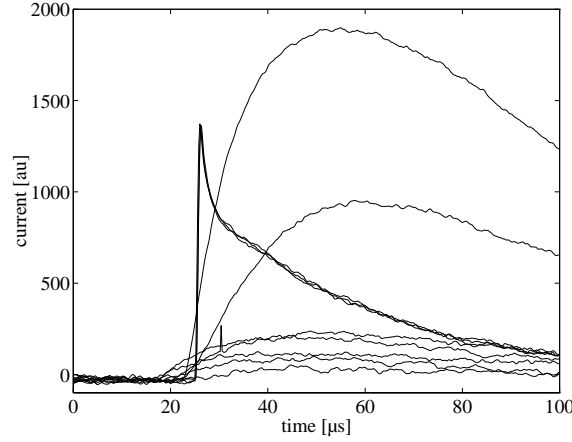


Figure 4.7: This plot is an example of real pulses from 60 keV gamma rays and injected heat pulses. The heat pulses have the fast rise time and sharp peak.

Detector performance

One of the most interesting questions to answer with these devices is determining the time constants which are involved in the pulse shape. In figure 4.7, we see examples of pulses in one sensor from 60 keV gamma rays and heat pulses. The heat pulses were generated by injecting a short tail pulse into the sensor bias line. The heat pulses are the pulses which appear with a very fast rise time and fast decay time. The sharp peaking which occurs in the beginning of the heat pulse is due to crosstalk between the bias lines and readout. The decay time of the heat pulses is a measure of the ETF time constant which in this sensor was $\sim 40 \mu\text{s}$. In contrast, the decay time from the gamma ray events were $\sim 100 \mu\text{s}$. Consequently, it appears the pulse shape is strongly dependent upon the time constants involved with quasiparticle collection/diffusion from the Al to W and the flux of athermal phonon energy incident upon the Al. Another extremely useful plot for characterizing a sensor is a plot of the sensor current as a function of voltage bias. In fact, our group likes to call the plot an “IbIs” plot because the sensor current (I_s) is plotted as a function of the bias current (I_b) across the bias resistor which forms the voltage bias. The “IbIs” plot is analogous to a load curve for bolometers [29]. The “IbIs”

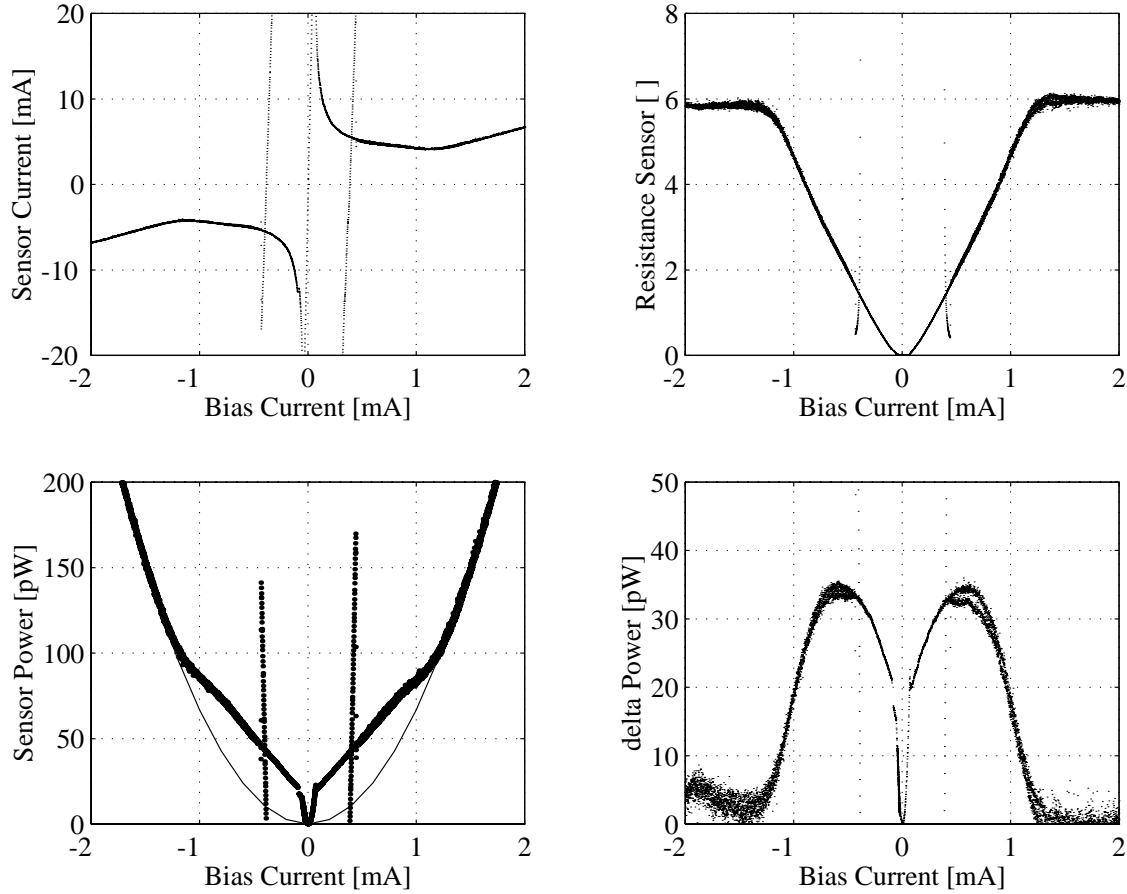


Figure 4.8: The upper left plot is a plot of the current bias (I_b) versus the sensor current (I_s). This is otherwise known as an “ $I_b I_s$ ” plot. With this plot, the sensor resistance and power dissipation can be computed (other plots).

curve for on phonon sensors on this detector appears in the graph in the upper left hand corner of figure 4.8. The graph in the upper right hand corner is the detector resistance as a function of current bias. For large bias currents, the detector reaches its normal resistance value of $\sim 6 \Omega$. In the graph in the lower left corner, the darker line is the power dissipated by the sensor as a function of current bias. The thin line is a plot of the power the sensor would have dissipated if it were completely normal. The vertical lines below 0.5 mA are artifacts due to the fact the sensor can

be superconducting at low bias. For the points along the dark curve which deviate from the normal resistance power parabola, sensor is self biased via electrothermal feedback. The sensors are operated with a bias current in this region. The difference between the operating point powers (quiescent power) and completely normal power is the curve shown in the graph in the lower right corner of figure 4.8. In essence, this curve represents the maximum possible rate at which the sensor can be cooled as a function of bias current.

The IbIs data presented in figure 4.8 is particularly interesting. At the time, it indicated that the sensor was behaving a little differently than we expected. To first order, one expects that the power dissipated by the sensor should be roughly constant. This would manifest itself in a hyperbolic shape to the IbIs curve for points in which the sensor is self biased and in a nearly horizontal line (constant power) in the sensor power versus bias current for self biased operating points. At the higher operating point bias, the power curve is close to being horizontal before clearly taking a downward slope a lower bias. It appears the downward turn occurs at a bias close to where the cooling rate is a maximum.

Because of the unexpected shapes in the IbIs curves, I took data at a variety of operating points for events from a 60 keV gamma source. Figures 4.9 and 4.10 summarize the results. Figure 4.9 are plots of the signal peaks in sensor A versus sensor B. There are two immediate things to notice. The first is that the current pulse for a given gamma ray energy diminishes as the bias of the sensor increases. Also, there does not appear to be a severe suppression of signal for events shared between the two sensors. This is because the 60 keV gammas from the external ^{241}Am source must pass through a lead collimator placed just above the detector which only allows events to hit the middle of the crystal. In contrast, figure 4.10 contains plots of the integrals (collected energies) as a function of sensor bias. It is interesting to note that the bias which is optimal for collecting the most energy is

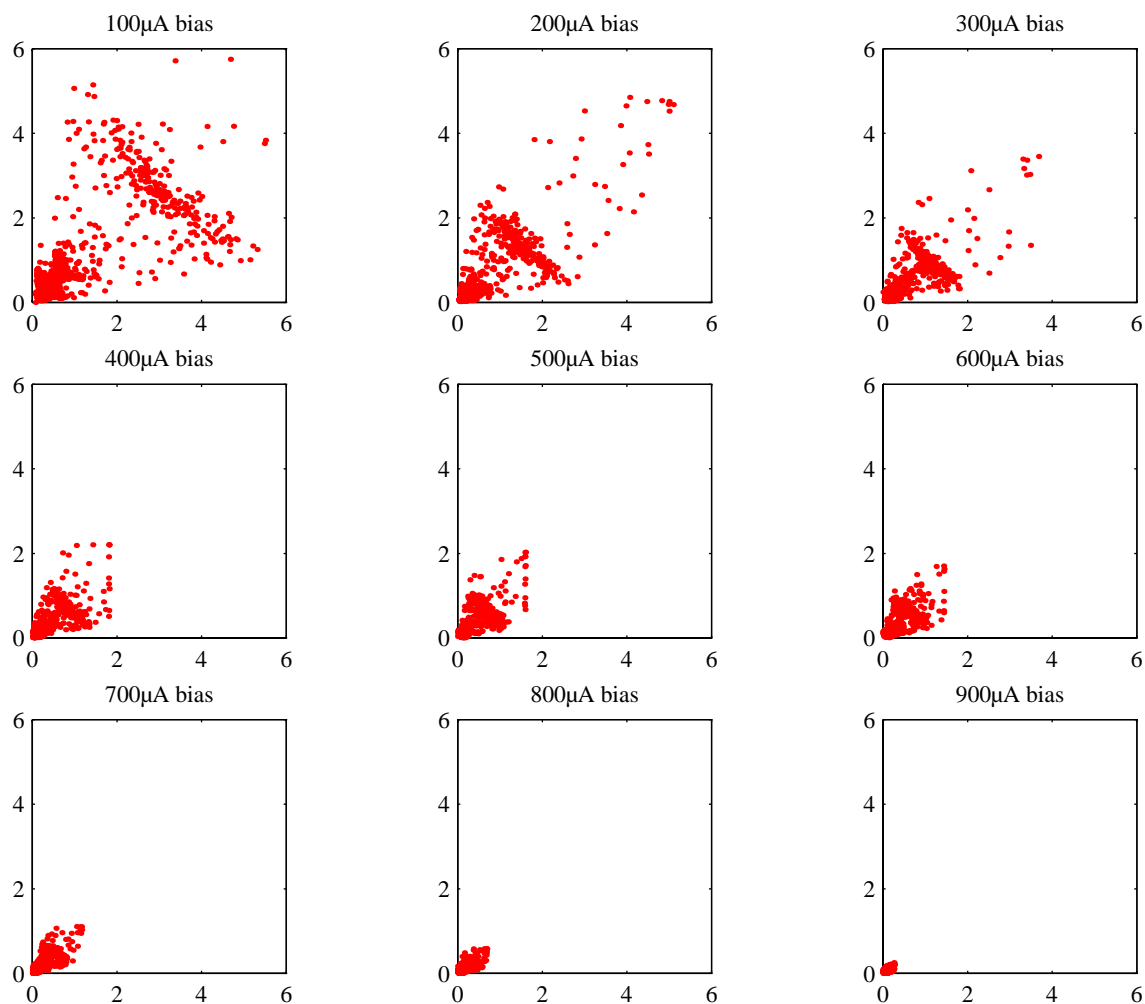


Figure 4.9: Peak a vs Peak b as a function of bias current. These plots show that the largest signals in a and b when measuring only the peak height occur at the lowest current biases.

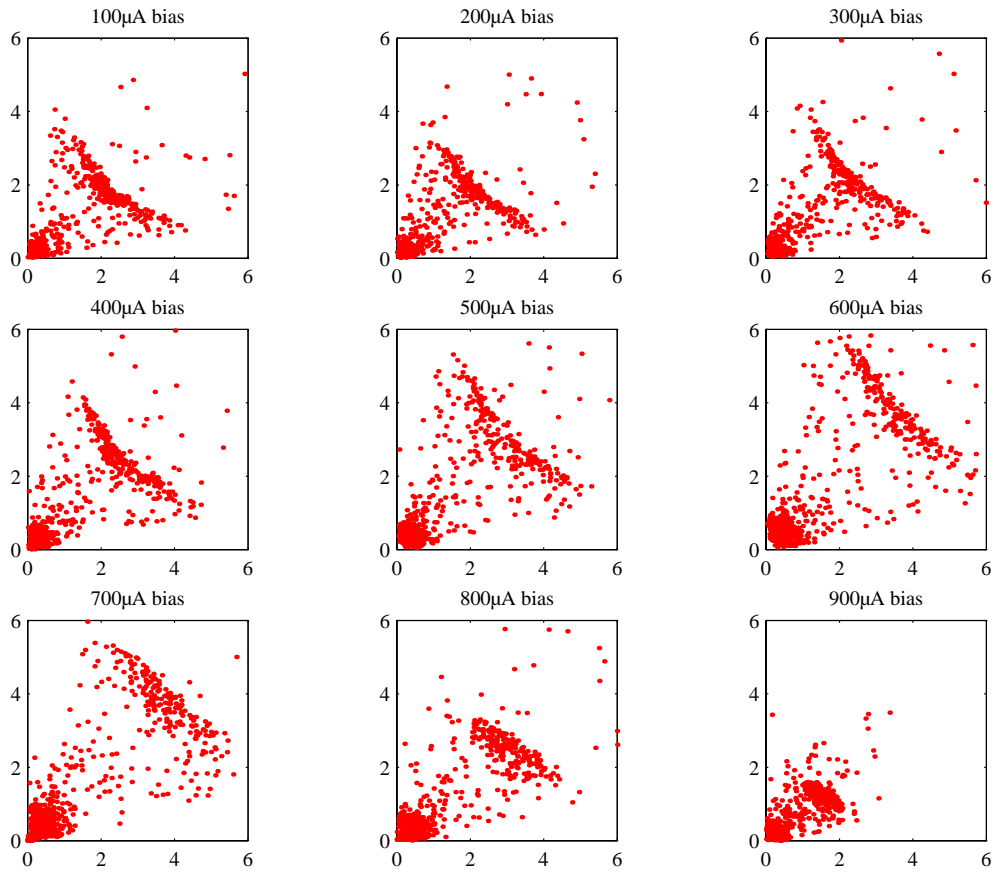


Figure 4.10: Collected energy in A versus collected energy in B as a function of bias current. The largest signal (collected energy) occurs at a bias of $600\mu\text{A}$.

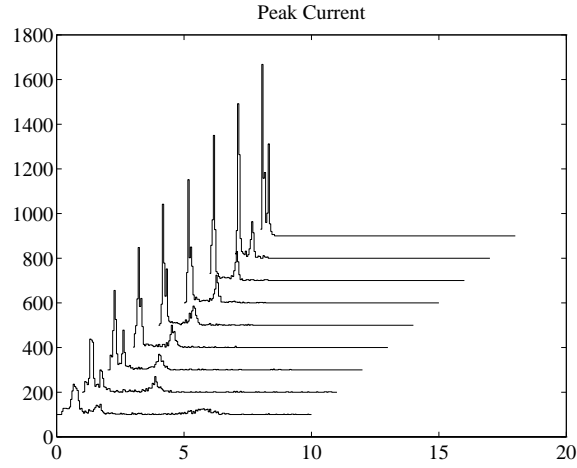


Figure 4.11: Histogram of the sum of the peak height in A and B as function of current bias.

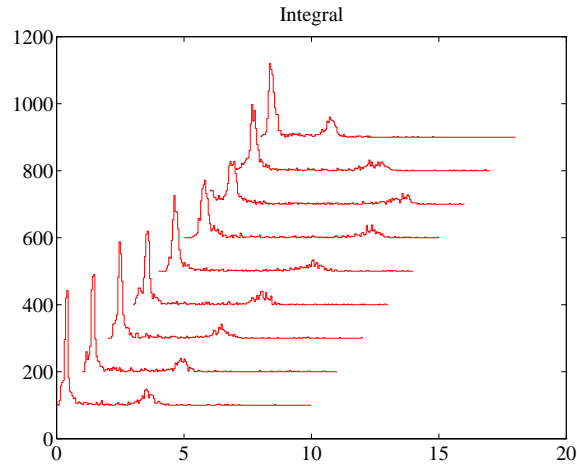


Figure 4.12: Histogram of the sum of the collected energy in A and B as function of current bias.

close to the bias at which the maximum possible cooling rate can occur.

Figures 4.11 and 4.12 summarize the previous plots. In figure 4.11, I have plotted a histogram of the sum of the peak height measured in sensors A and B as a function of bias. The bias value in microamps forms the horizontal baseline for the histograms. So for maximum peak heights, it is beneficial to operate the detector at lower biases. In contrast the histograms in figure 4.12 indicate that for maximum collected energy it is better to bias near $600 \mu a$.

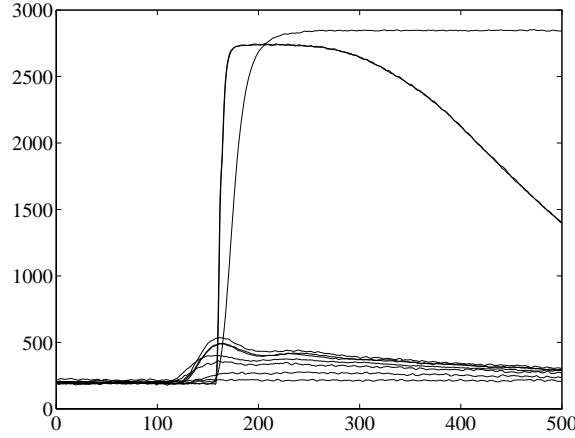


Figure 4.13: Examples of pulses which saturates a phonon sensor by driving the tungsten completely normal.

The most likely explanation for the discrepancy for the optimal bias point for maximum peak height and maximum collected energy is that the sensor may not be entirely resistive at lower biases. In essence, at low biases there is insufficient power along the meander and the thermal conduction along the W meanders is poor enough that phase separation can occur in which part of the meander is superconducting and part is resistive. As a result, energy which is coupled into portions of the meander which are superconducting don't immediately result in a resistance change and consequently observed signal. Instead, some of the energy is used to heat the meander until it is resistive. This energy is never collected via electrothermal feedback. Another piece of evidence supporting this hypothesis appears in figure 4.13. The pulses of interest are the ones which appear to saturate. The pulse which saturates at a lower value are pulses from my attempt to inject heat pulses which completely drive the sensor normal. When the sensor is completely normal, the current through the saturates hence the clipped appearance to the pulse. The pulse which is clipped at a value above the injected pulse is due to a muon. If one calculates the resistance of the sensor for the clipped portion of the injected heat pulse, the resistance is lower than that of the resistance calculated for the clipped portion of the muon event. In

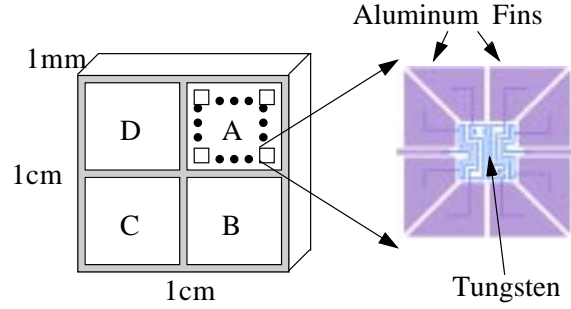


Figure 4.14: A sketch (not drawn to scale) of the 1cm x 1cm x 1mm 1/4g detector and the phonon sensor labeling scheme used to describe the results.

fact, the muon event does drive the sensor completely normal, while the injected heat pulse does not. I believe that the sensor is phase separated at this bias (200 μ A) and I was only able to drive the resistive portion normal.

4.2 Full Surface coverage

A critically important aspect of a dark matter experiment is a large detector mass. For detectors based on athermal phonon detection, one would like to cover as much of the detector surface with phonon sensors. As mentioned previously, one would like to collect as much of the athermal phonon energy before it thermalizes. In the detectors described in this thesis, the first step was to demonstrate reasonable phonon collection efficiency with aluminum quasiparticle traps. In the next sections, I will describe results from covering most of one surface of the silicon crystal substrate with phonon sensors. A sketch of cm x 1 cm x 1 mm detector with full surface coverage with phonon sensors is shown in figure 4.14 .

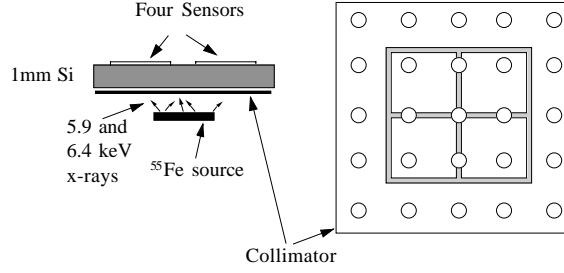


Figure 4.15: A sketch of the source and collimator position of the ^{55}Fe used with the 1/4g detectors.

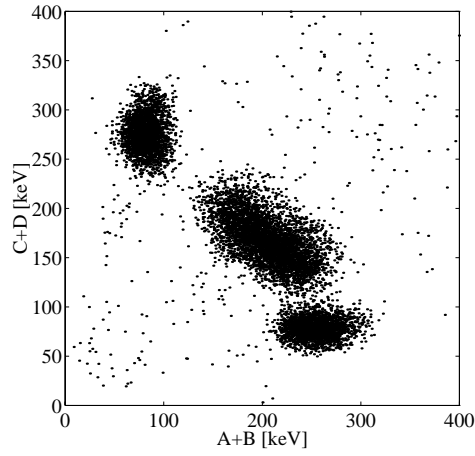


Figure 4.16: A plot of the energy collected in two sensors (A and B) versus the energy collected in two others (C and D).

4.2.1 1 cm x 1 cm x 1 mm Phonon only sensors

2D Position information

Figure 4.15 is a cartoon which describes the experimental setup used to test the response of a our four phonon sensor detector on a $\frac{1}{4}\text{g}$ Si substrate. Not shown in the diagram is the lead collimator placed above the phonon sensor side for collimating the x-rays from the external 60 keV source (^{241}Am). The detector response to the x-rays from the ^{55}Fe source which pass through the 5x5 grid of holes is shown in figure 4.16. The energy collected in sensors A and B are added and plotted against the sum of the energy collected in sensors C and D. The three populations demonstrate

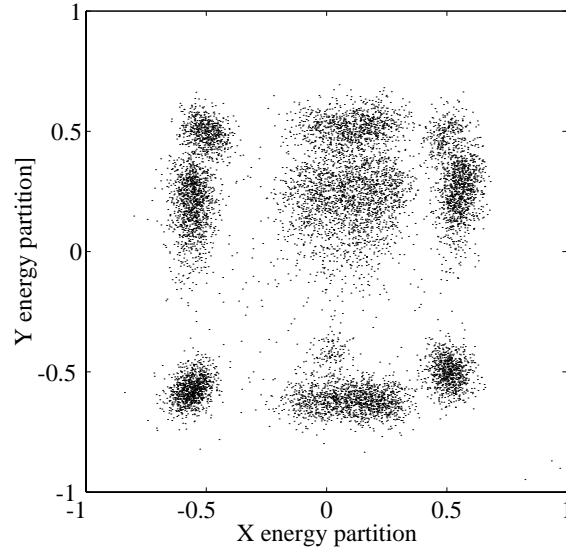


Figure 4.17: Plot of the partitioning of energy between the four sensors for 6 gamma rays.

that the partitioning of energy between pairs of sensors gives a sense of the spatial location of the event. However, one would expect that the three populations would form a better 45° line. The fact that the line is not a good diagonal indicates that the four sensors do not have similar sensitivity.

For notational simplicity, it is convenient to use AB to describe the sum of the signals in sensors A and B, CD to describe the sum of C and D, and similarly for AD, BC, and ABCD. Because the spatial location of an event results in a partitioning of the energy between the four sensors, it is convenient to parameterize the distribution by looking at the difference between AB and CD normalized by ABCD (total energy). In some sense, $\frac{AB-CD}{ABCD}$ is a measure of the x position of the event. Figure 4.17 is a plot of the energy partitioning in the x direction $\frac{AB-CD}{ABCD}$ versus $\frac{AD-BC}{ABCD}$ for events from the ^{55}Fe source. A 3x3 partitioning of the events is evident. A tenth population appears in the faint collection of points above the lowest center population. The slight asymmetries in the corners are evidence that the collimator is not centered with respect to the sensors. Figure 4.18 is a similar energy partitioning plot for

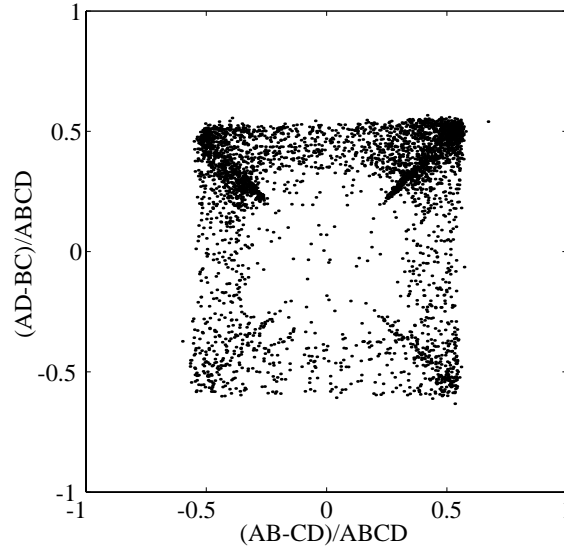


Figure 4.18: Plot of the partitioning of energy between the four sensors from 60 gamma rays.

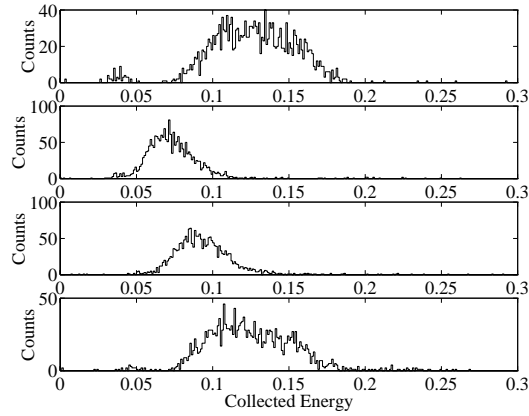


Figure 4.19: fig:etf19-collection

Figure 4.20: Histograms of the energy collected in the four phonon sensors, A-D, top to bottom for events from a Am^{241} .

the 60 keV's coming from the external source, but collimated to illuminate only the center portion of the detector. One important feature to note, is that for events which occur directly under one sensor, only 50 percent of the total collected energy is collected by that sensor. The remaining 50 percent is collected by the other three.

Figure 4.20 is a set of histograms for each sensors for the amount of energy

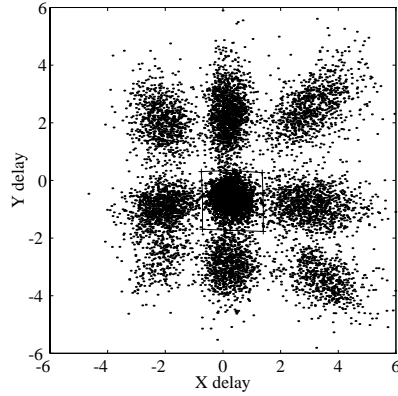


Figure 4.21: Delay Plot from a 6 keV gamma source

collected from events from the 6 keV source. From these histograms, it appears that sensors A and D are more sensitive. However, in fact the collection is very similar and the perceived reduced sensitivity is a result of the 6 keV x-rays not uniformly illuminating the detector. In fact, the collimator is shifted towards A and D. A much clearer method to extract position information is to look at the delay in the start time of the pulses. By looking at the difference in time of the start of the pulses formed by summing the signal from different pairs of sensors, we get the graph in figure 4.21. The x coordinate is determined by calculating the difference in start time for the pulses formed by AB and CD. Similarly, the y-coordinate is from the difference in start time between AD and BC. Because the QET sensor technology is sensitive to athermal phonons and sensor response time and readout time are sufficiently fast, we are able to see the propagation delay in the phonon time-of-flight from the initial event location to the sensors. The fact that the center population is shifted below zero also demonstrates that the collimator is shifted towards A and D because the delay in phonon sensors B and C will be greater because the events hit closer to A and D and further from B and C.

From figure 4.21, it is apparent that the delay parameterization of the position information is much less sensitive to the non-uniform sensor response. Using the

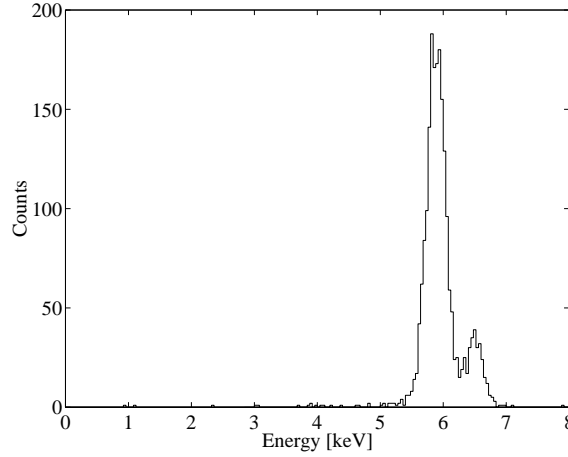


Figure 4.22: Histogram of the events from a 6 keV gamma source hitting the center of the detector. Both the K_α and K_β lines are visible.

delay information, we could attempt to do a first order position dependent correction to the collected energy for the sensors with poor collection. However, without such a correction, we still can see that the detector has good energy resolution. Figure 4.22 is a histogram of the total signal from all four sensor for events which passed through the center hole. The cut for determining which points passed through the hole is determined by the events which are within the square drawn around the center population in xy delay figure 4.21. In this figure, the collected energy was rescaled to the energy of the K^α 5.9 keV and K^β 6.4 keV gammas rays from the Fe^{55} source. The energy resolution is ~ 300 eV FWHM.

4.2.2 1 cm x 1 cm x 1 mm Phonon and Ionization

In the new generation dark matter experiments like CDMS of which our group is a member, dark matter detectors have some form of radioactive background rejection. In the CDMS detectors, the discrimination is based upon the measurement of phonon energy and ionization yield for a given event. In the following section, I describe the results from the first detector which has QET athermal phonon sensors and an

ionization electrode.

Effects of the electrode

One of the first questions to answer was the effect of the electrode on the phonon signal. In figure 4.23, I've plotted the energy collected in AB versus CD for events from the 60 keV source for the sensor described in the previous section and the sensor described in this section. The only difference is the presence of a $\sim 20\text{nm}$ thick Au electrode on the side opposite the phonon sensors. One notices immediately, that more energy is collected in the phonon sensor only device. One also would expect the graph to be symmetric about a radial 45° line. However, because of different sensor sensitivities this is not the case. If one "corrects" the energy collected so that all the sensors have the same response, then the total phonon energy collected in the detector with the electrode is 50% of the phonon energy collected in the detector with only phonon sensors. Some of the "correction" in energy collection is due to $\approx 10\%$ uncertainty in the shunt resistor which sets the bias voltage. Another subtle feature in figure 4.23 is that more of the events are pulled closer to the x- and y-axis because of athermal phonon losses associated with the Au electrode so that much less of the athermal phonon reaches the more distant sensors.

Discrimination-Gamma response

For a dark matter detector, it is important to understand the detector's ability to discriminate between electronic and nuclear recoils. The plot in figure 4.24 is the detectors response to the external ^{241}Am illuminated on the phonon-side (front) passing through a centering collimator. The x-axis is the total collected phonon energy, and the y-axis is the size of the ionization charge pulse. This type of plot will be referred to as a 2D plot. For radiation which recoils off electrons such as gamma rays and x-rays, the amount of charge per deposited energy is roughly constant and

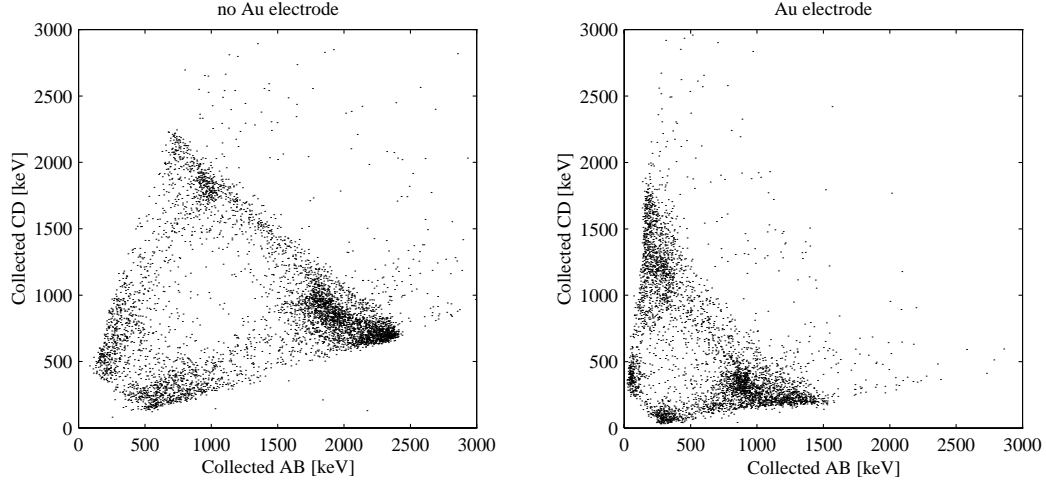


Figure 4.23: AB versus CD for 60 keV gamma rays in a detector without a Au electrode on the backside (left figure) and with a Au electrode (right).

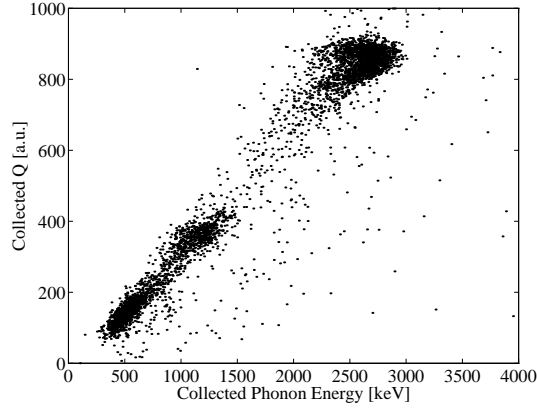


Figure 4.24: Raw plot of the collected energy versus ionization.

is parameterized by a quantity called the yield. In Si, the charge yield is $\frac{1}{3.8} \text{ eV}^{-1}$ of deposited energy. For radiation which recoils off of the Si nucleus, the charge yield is about three times smaller. The difference in charge yield is the origin of the discrimination.

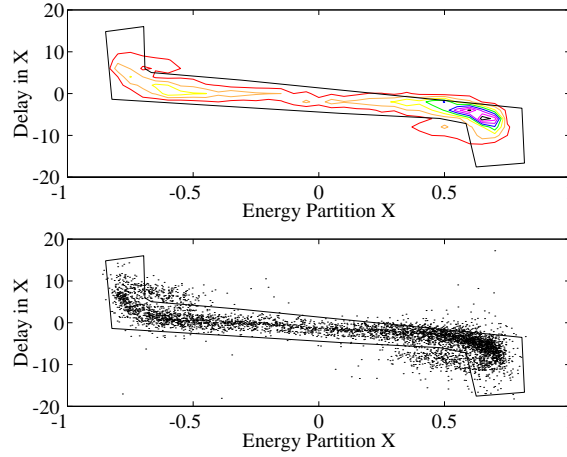


Figure 4.25: Plot of the energy partitioning in the x-direction versus the delay in signals in the x-direction. The upper plot is a contour plot of the lower plot. The odd shaped polygon encloses events which occur with a central x-position.

In figure 4.24, there is a significant population of events which do not fall on the “gamma line”. These events suffer from incomplete charge collection. Incomplete collection can occur near the edges of the crystal where there may be space charge build up. Near these edges, the electric field will not be uniform and is also reduced which causes degraded charge collection. The lower charge collection at low electric fields in silicon was studied by Mike Penn [34].

Using the athermal phonon signal, it is possible to remove/veto events which occur near the edges. In figure 4.25 and 4.26, delay in phonon signals is plotted versus the energy partitioning. In both figures, the upper plot is a contour plot of the lower plot. By plotting the delay versus energy partitioning, it is apparent why the delay is a better measure of the spatial position. As was described earlier, events which occur towards the edge of the crystal and away from the center of a sensor begin to share more of the energy with other phonon sensors. This causes a degeneracy in the energy partitioning versus position.

In both figure 4.25 and 4.26, I’ve drawn in a polygon around points which are not near the edge. A 2D plot of the points which correspond to those points away

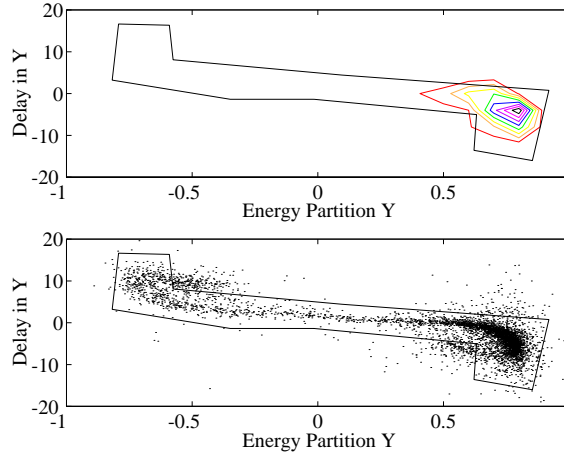


Figure 4.26: Plot of the energy partitioning in the y-direction versus the delay in signals in the y-direction. The upper plot is a contour plot of the lower plot. The odd shaped polygon encloses events which occur with a central y-position.

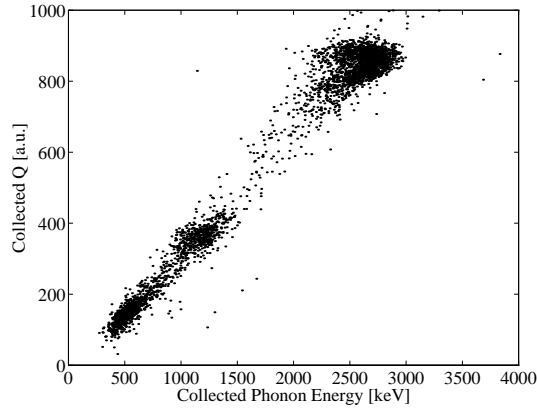


Figure 4.27: Plot of the collected energy versus ionization for events in the middle of the crystal.

from the edge appears in figure 4.27. Note that there are many fewer off diagonal points which were due to incomplete charge collection.

Another demonstration of the power of having some position information is shown in the next two figures. Figure 4.28 is a 2D plot from the detector using the same external 60 keV source positioned on the opposite of the detector. In this case, there is no lead collimator so the 60 keV events occur throughout the Si detector. Because of space charge build up near the edges, there is a reduced field near the edges. In

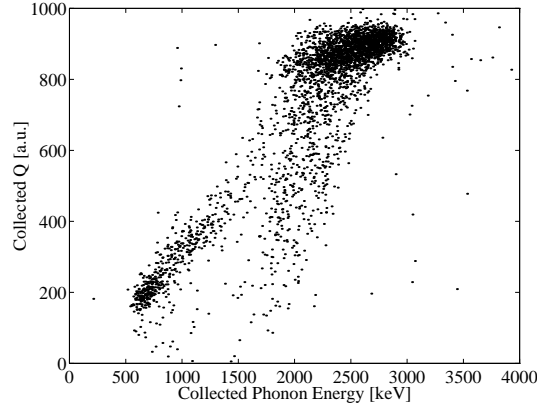


Figure 4.28: 2D plot with a rain cloud due to incomplete charge collection.

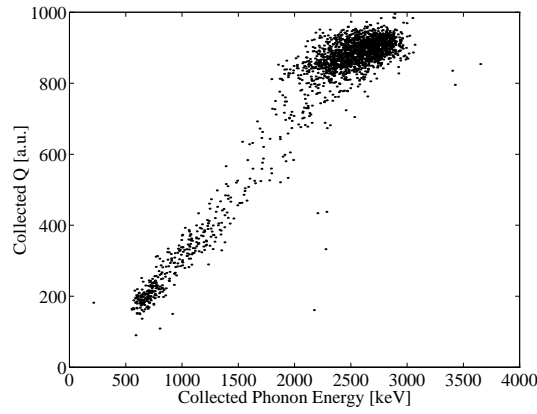


Figure 4.29: 2D plot with the rain cloud removed by cutting events which occur near the edges of the detector.

regions of reduced field there is a reduced collection of the charge. The result is the appearance of a “rain cloud” in the 2D plot where the “cloud” is formed by the events with complete charge collection and the “rain” are the events with incomplete charge signal. The fact that the rain appears to fall at a slope is due to Neganov-Luke effect [32, 30] which will be described later. If I apply the same position cut as used to clean up the 2D plot from front side illumination, I get the 2D plot shown in figure 4.29

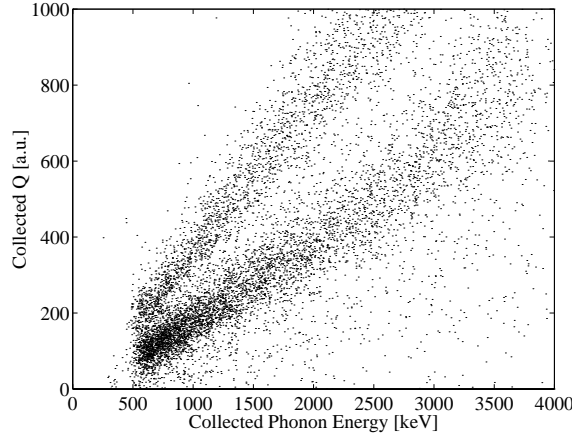


Figure 4.30: Raw 2D plot from exposing the detector to a PuBe neutron source.

Discrimination-Neutron response

To calibrate the neutron response of the detector, a PuBe neutron source was used. It is not only a source of neutrons but also of gamma rays. The 2D plot without any corrections is shown in figure 4.30. There are two radial bands. The upper band is due to gamma rays. The lower band is due to neutrons which have a lower charge yield.

Figure 4.31 summarizes the parameters used to clean up the 2D plot. An interesting feature to notice is that the energy partitioning peaks at 75%. This value is due to two effects. One is that the Au electrode on the backside is a source of athermal phonon loss. Consequently, for events which occur directly under one sensor some of the phonons are lost before they can diffuse to the other sensors. In fact for events closer to the phonon sensor side in depth, less of the phonon energy will be shared. The other is due to the Neganov-Luke effect. Neganov-Luke effect is that the electron-holes which drift across the crystal emit phonons associated with the work being done by the electric field to drift them across the crystal. In effect, there is an additional qV of phonon energy contribution where q is the amount of ionization and V is the voltage bias applied for the ionization measurement. These

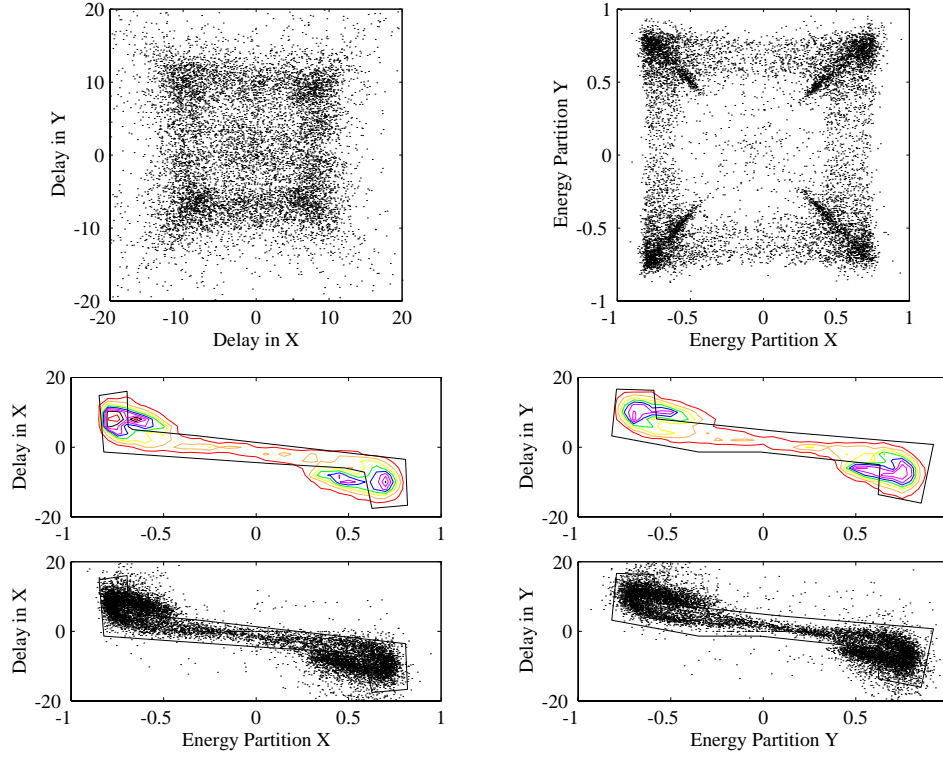


Figure 4.31: Plots used to determine the proper position cuts to eliminate events near the edges of the detector.

phonons are emitted from a line formed by the drift of electrons and holes across the crystal and accentuate the amount of energy absorbed in one sensor. The resulting 2D plot which uses the same cut which cleaned up the 60 keV gamma calibration data appears in figure 4.32 .

Ionization

As was mentioned previously, the work done on the electron hole pairs as they drift across a crystal in an electric field appears in the form of athermal phonons which can be observed by the phonon sensors. In figures 4.33 and 4.34 , the collected phonon energy is plotted versus the collected ionization signal for various voltage

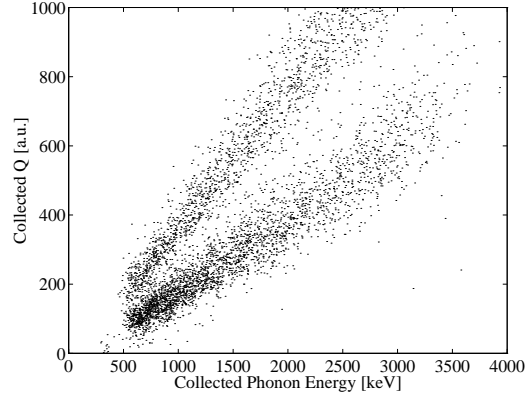


Figure 4.32: 2D plot after removing events near the edges.

biases applied across the crystal. Figure 4.33 is for events from the 60 keV source. One can see that as a function of voltage bias across the crystal, the ionization is relatively constant, but the phonon energy increases. Figure 4.34 shows the Luke effect for events from the 6 keV source passing through the 5x5 grid. In this case, we can see that at low fields the position information is difficult at low electric fields. As the voltage is increased, the phonon signal becomes large enough that extracting position information is easier.

From Mike Penn's work [34], it is well documented that the collection of charge at low temperatures and at low electric fields in silicon is very difficult, primarily because it is difficult to grow ultra pure silicon crystals. Because of impurities, charges drifted in low electric fields are easily trapped at impurity sites. In figure 4.35, the collected charge signal is plotted as a function of the voltage bias. For higher voltage biases, the charge is more efficiently collected.

Recoil energy

In principle, it would seem advantageous to operate the detector at high fields. However, the signal of interest in a dark matter detector is the amount of energy initially deposited by the incoming particle, recoil energy. To obtain the recoil energy

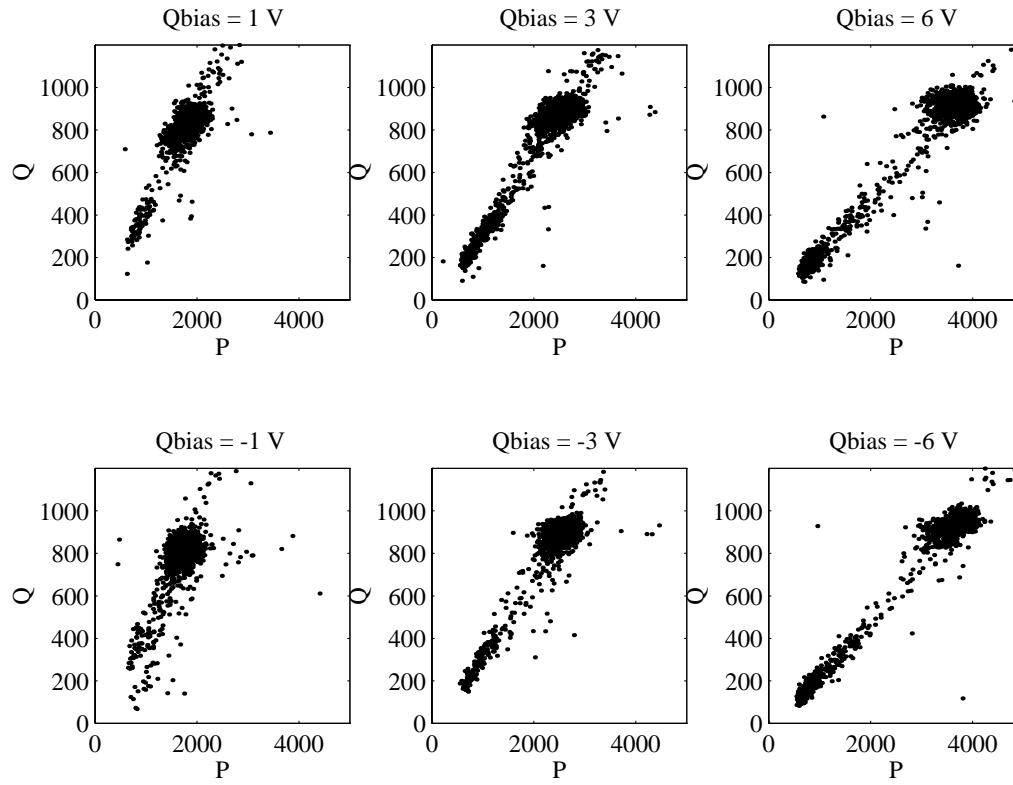


Figure 4.33: 2D plots of collected energy versus ionization as a function of applied electric field for the ionization to demonstrate the Luke effect.

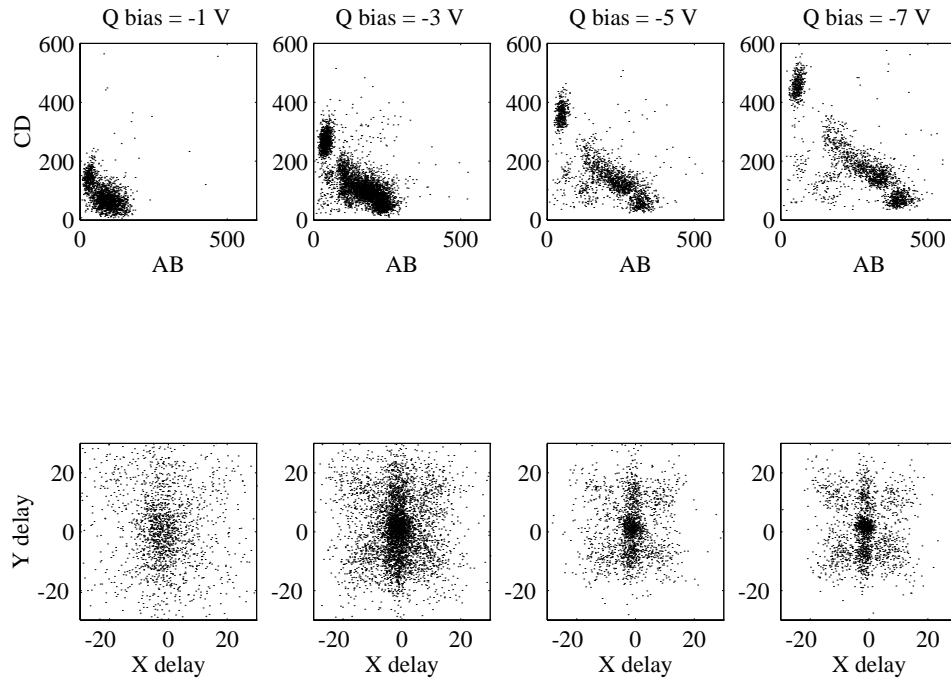


Figure 4.34: AB versus CD as a function of applied electric field for events from a 6 keV gamma source.

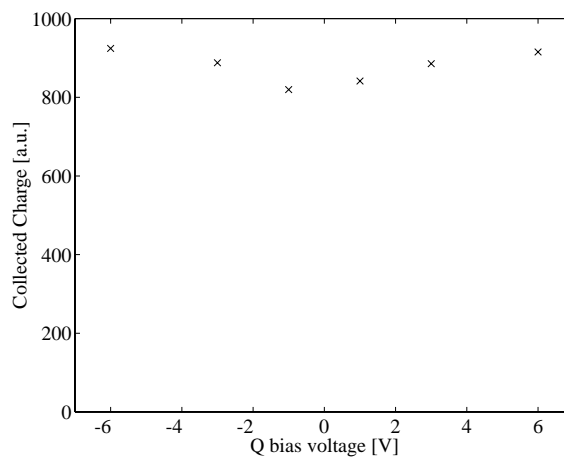


Figure 4.35: Seagull plot

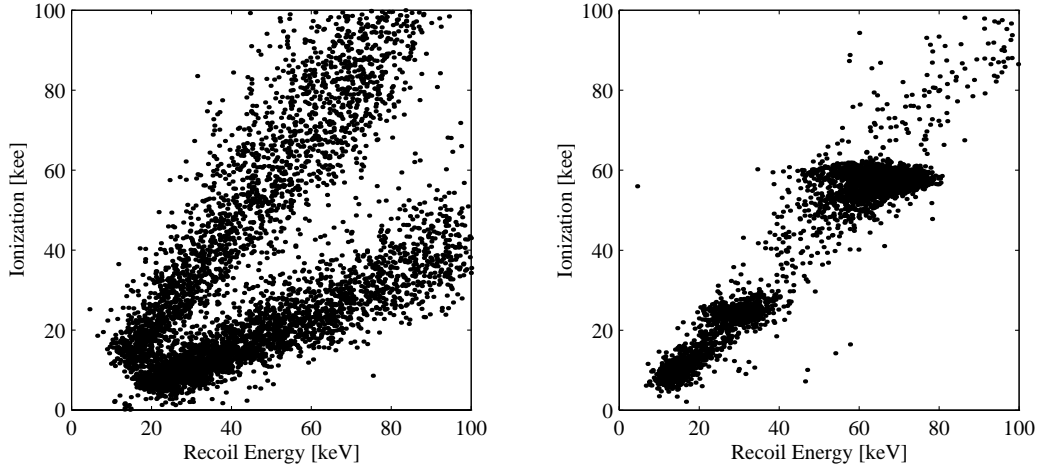


Figure 4.36: 2D plots of a neutron calibration and gamma ray calibration corrected so that the recoil energy is plotted versus ionization.

the luke phonon signal must be subtracted from the observed phonon signal. At very high fields the noise in the ionization measurement will dominate over the intrinsic noise in the phonon measurement. Ideally, one chooses an electric field where the ionization noise contribution to the noise in determining the recoil energy is equal to the intrinsic phonon measurement noise. This value tends to occur at low electric fields.

In figure 4.36, I've plotted the gamma and neutron calibration data after subtracting the Luke effect contribution to the data and after using the 60 keV peak as a calibration point. Ideally, the smearing in the phonon signal can be taken out before the Negenov-Luke correction using x, y, and z position information. In figure 4.37, I've plotted natural log of the ratio of the charge signal divided by the phonon signal as a function of recoil energy. I've also renormalized the graph so that an electronic recoil appears at the ratio of 1. Consequently, the nuclear recoil band appears at about a 40% of the electronic recoil. I've also plotted a histogram of the ratio of Q/E , where E is the recoil energy. By looking at the gamma response and the neutron response, we are able to measure the discrimination between nuclear

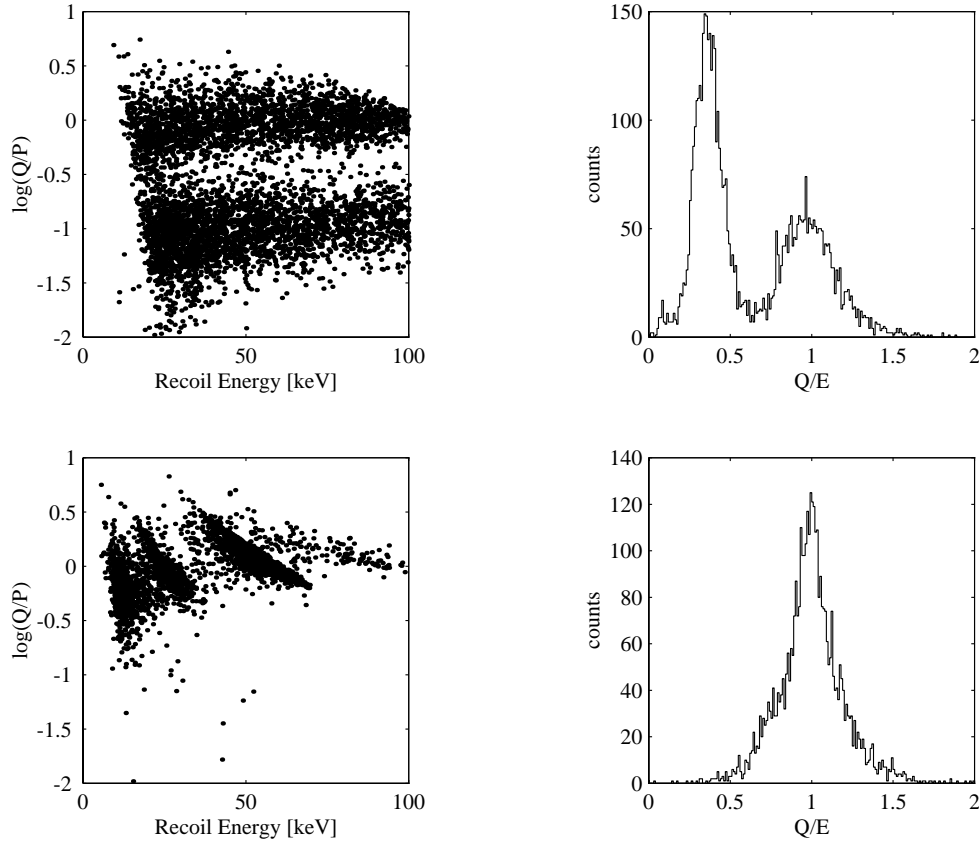


Figure 4.37: Ionization yield plotted as a function of recoil energy from exposure to a neutron source and a gamma ray source. The smearing of the 60 keV peak is due to position dependence and uncertainty in the Luke correction.

recoils and electronic recoils. From the data, the gamma rejection efficiency is $> 99\%$ down to 20 keV in recoil energy.

4.3 Larger Mass

For a dark matter detector, it is important to use as large a detector as possible. The final plans were to build dark matter detectors on 1 cm thick 3 in diameter Si and Ge wafers. However, going from 1 cm x 1 cm x 1 mm to the large detector seemed too large of a jump. Furthermore, the first QET mask designs with the 1 cm x 1 cm

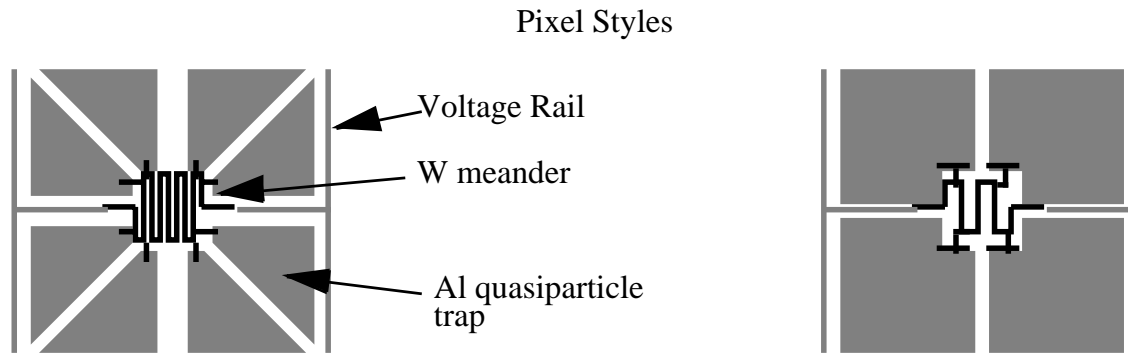


Figure 4.38: Sketch of the two phonon pixel styles. The one on the left is for the small prototype devices. The one on the right is the design for the larger mass detectors.

devices wouldn't scale to cover the surface of a 3 in wafer. The normal resistance would be too low. As a result, our group fabricated 2 cm x 2 cm x 4 mm detectors. Two type of phonon sensor designs were used. The first type was identical to the one used on the earlier devices. The second type was a design which could scale to cover a full wafer. A drawing of the two types of phonon sensor pixels is shown in figure 4.38 .

4.3.1 First Design

Phonon only device

Figure 4.39 shows the response of the detector to x-rays from the ^{55}Fe source passing through the 5x5 grid collimator. The main purpose of this plot is to demonstrate the effects of what is believed to be an adsorbed helium layer.

When we initially cool the dilution refrigerator, we use helium exchange gas to cool from 77K to 4K. At 4K, the helium exchange gas is pumped out until the leak rate is below 3×10^{-6} cc/Atm $^{-1}$. When the 1K pot is turned on, most of the remaining exchange gas adsorbs onto it. From private conversations [13] , it is believed that the first monolayer of He adsorbed to surfaces has a binding energy of many tens of

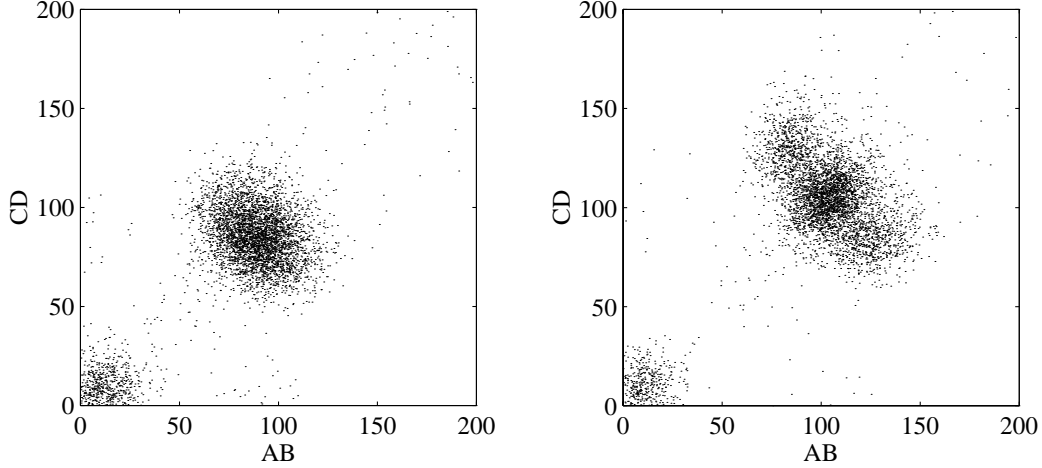


Figure 4.39: These plots show the effects of an adsorbed Helium layer on a detector. The figure on the left has a layer, the one on the right does not.

K. The second monolayer is believed to be $\sim 9\text{K}$. As a result, not only has the 1K pot adsorbed helium, but the walls of the IVC which are at 4K also have helium layers. As time goes on, the liquid helium level drops and the top portions of the IVC warm above 4K . Any helium adsorbed on these surfaces can come off and find its way to colder portions of the refrigerator. Most probably to go the 1K pot, but some find their way to the sensor. An adsorbed helium layer is a good phonon absorber and will degrade our signal.

We have developed a technique which we have called a “double pumpout” to reduce the effects of the adsorbed helium layer. The technique has evolved to the point where the name is now a misnomer. It used to be common for the devices to be cooled in the conventional manner to base temperature. After some running time, there would be some question as to whether an adsorbed helium layer had formed yet. As a result, the probe would be warmed to above 4K and all the helium

exchange gas would be pumped out. The dilution unit was warmed above 4K by removing the liquid helium surrounding the IVC and using the heaters on the still and mixing chamber. After the IVC was pumped out to a leak rate less than 3×10^{-9} cc/Atm $^{-1}$ at a temperature which was somewhere between 4K and 77K (the RuO resistor was typically between 1.05 and 1.03 k Ω where 1.012 is 77K and 1.2 is 4K). The sample would be recooled by adding liquid helium back into the refrigerator, by turning on the 1K pot, and by circulating the He 3 /He 4 mixture. After about an hour or several hours depending upon how warm the sample stage got and how much thermal mass was at the sample stage, the refrigerator would cool normally to base temperature. Because of the two pumpouts of the exchange gas, these runs (cooldowns) were said to have undergone a “double pumpout”.

The standard cool down procedure now known as the “double pumpout” is to pump out the exchange gas only once in the beginning of the run. As liquid helium is being added to the refrigerator for the first time and the temperature is cooling from 77K to 4K, one begins to pump out the exchange gas right before the mixing chamber thermometer reaches 4K. Inevitably, the pumpout proceeds slower than the liquid helium transfer and the mixing chamber thermometer eventually reads 4K. At this point, the liquid helium transfer is stopped and the liquid helium is siphoned out completely (or reduced to a level below the IVC). If it is necessary heat is applied using the heaters, and the exchange gas is completely removed to a leak rate level measurement of 3×10^{-9} cc/Atm $^{-1}$ at a temperature above 4K. At this point, the cooldown procedure continues as described before. Figure 4.39 shows the detector response before the pumpout in the plot on the left side and the response after in the other plot. One effect is that it blurs the ability to extract some position information from the partitioning of energy, and another effect is that the adsorbed helium layer attenuates the signal.

Another important point from figure 4.39 is that the total collected energy (200

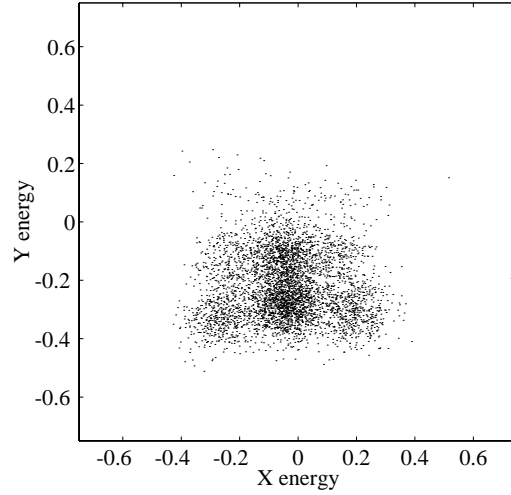


Figure 4.40: Position sensitivity of a 4 g detector to 6 keV X-rays.

eV) in this device, which only has phonon sensors, is similar to the total collected energy in the smaller device (300 eV), despite a factor of 16 increase in volume/mass. This is definitive proof that the phonon detection scheme is based on observing athermal phonons and that the detection scheme to first order is independent of absorber heat capacity!

Figure 4.40 shows the energy partitioning response in X and Y of the detector to the 6 keV source passing through the collimator of 5x5 holes. In this run, the source was placed off center of the grid. Consequently on the lower half of the sensor was illuminated.

In figure 4.41, the events from illuminating the crystal with a 60 keV source on the front side are shown in an AB vs CD plot. One significant feature is that the 60 keV band is smeared. The slightly hyperbolic bend is due to position dependence, but some of the apparent width in the band is due to non uniform sensor response. Another feature to notice are the population events which lie close to either the x- or y-axis. These appear to be out of the expected distribution of points on the graph. These points are due to a trigger artifact. The problem is that two digitizer cards each with their own trigger input were used to digitize the four channels. Because

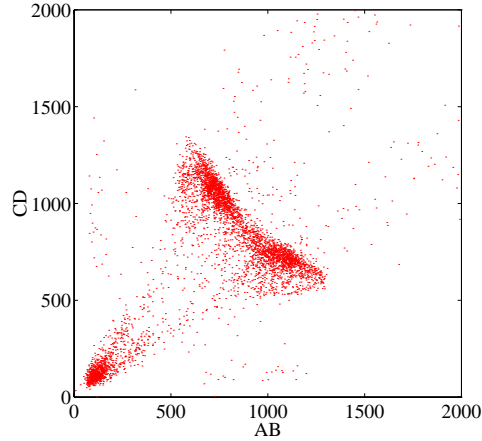


Figure 4.41: Response of the 4g detector to the 60 keV gamma ray source.

of the software system used to acquire the data, the trigger inputs for each card could not be enabled simultaneously. As a result, for a small fraction of events it happened that a trigger occurred when one digitizer was armed, and one not. When this occurs, two of the phonon signals are from one event and the other are from the later event. Unfortunately, I did not correct for this artifact until after most of the data was taken for this thesis. In figure 4.42, I've plotted the total collected energy versus the energy partitioning and delay estimates of the X and Y position. One can see that the positive y direction has a deficit in collection. This causes a blurring in the resolution as a function of X position. The deficit in collection is probably due to breaks in the wiring of the phonon sensor. Often, there is damage to parts of the phonon sensors which are close to the edge of the crystal. This is primarily due to problems with the adhesion of the blue sticky tape used to protect the surface when dicing a 3in wafer of detectors. I've also been known to accidentally scratch a phonon sensor with a pair of tweezers when mounting a detector. Consequently, different numbers of phonon sensing pixels are connected for each sensor. Another possible reason for deficit in collection of energy is an artifact from the technique used to calculate the collected energy integrals. In my analysis, I assumed a shunt

resistance of $20\text{ m}\Omega$. The actual values for the shunt resistors are within 10% of this number. The uncertainties in the shunt resistance, result in uncertainties in the voltage bias and consequently the reduction in joule heating. On reanalysis, I found that a 10% correction is not large enough to symmetrize the partitioning of energy. The reduction in collected energy is also accompanied by an asymmetry in the distribution of relative delays. Because the delays are computed by looking at the 40% crossing point of the pulse, the asymmetry in the distribution of delays indicates there is a difference in pulse shape. Because the signal to noise ratio of a 60 keV γ -ray is high, I believe that it is more likely that a significant fraction of the reduced energy collection and skewed delayed distribution is a result of sensor damage.

4.3.2 Phonons and Ionization

In addition to looking at the performance of a phonon sensor only detector, a detector with both phonons sensors and an ionization sensor was fabricated and tested. Figure 4.43 shows the detectors response to the 60 keV gamma calibration source. The plot on the left hand side is a 2D plot of all the events. From the graph, it is clear that there are many off axis events (off the gamma line). Using knowledge about the position extracted from the delays and energy partitioning, the 2D plot can be cleaned up and is shown in the graph in figure 4.43 on the right side. In this device, the phonon sensors do not butt up against each other towards the center. Instead the exposed silicon on the phonon sensor side appears to form a window frame with a nice cross through the center. As a result, the 2D plot data has been cleaned up by looking at events which occur primarily under one sensor where the electric field is uniform.

Another cut which was applied to make the 2D plot look better is partially explained by figure 4.44 . In this figure, I've plotted the ratio of the charge signal

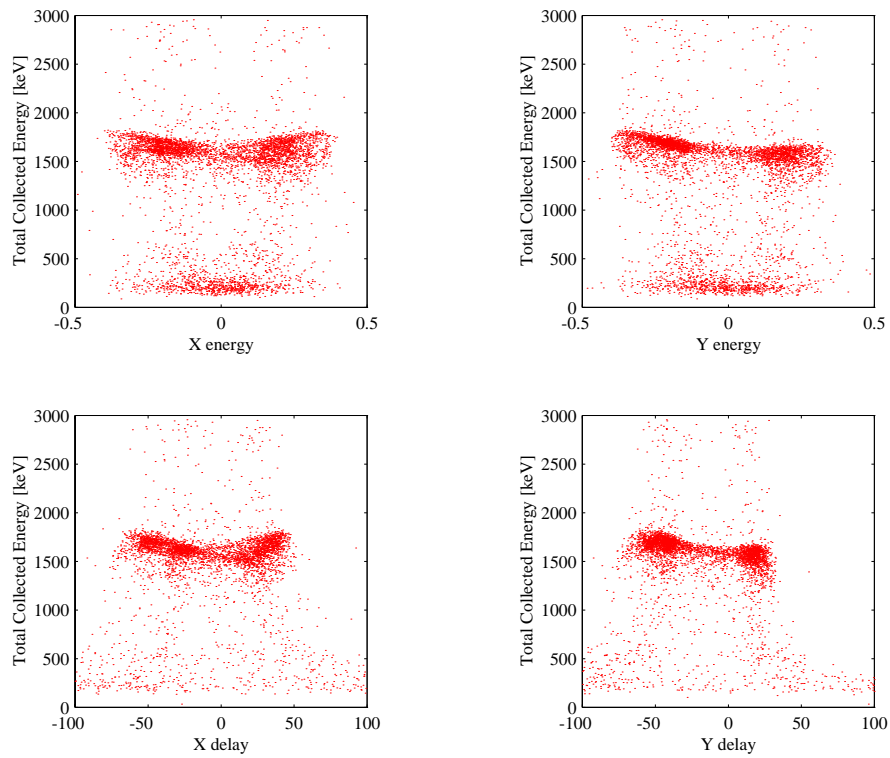


Figure 4.42: These plots show that the detector response (collected energy) is not uniform through the detector.

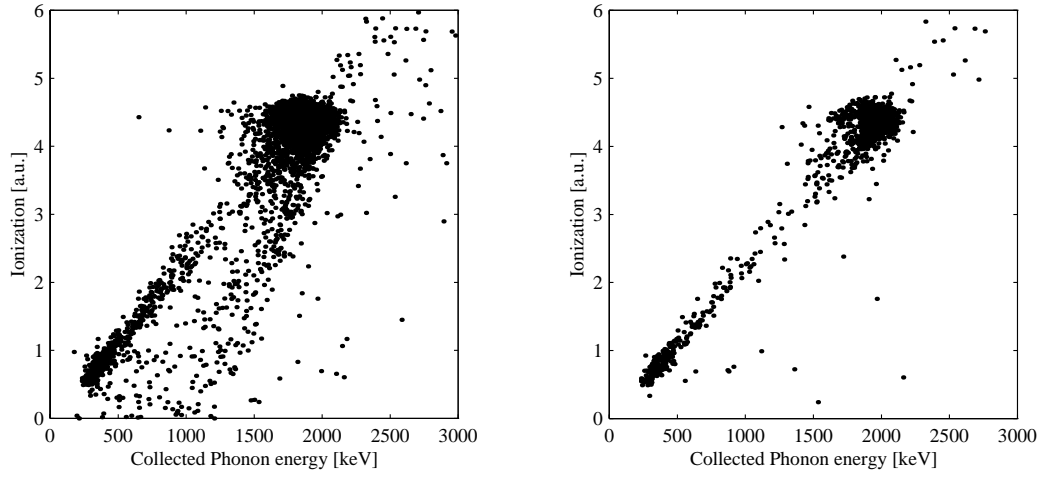


Figure 4.43: The left plot shows the 2D plot using all the events which hit the detector from a gamma source. The right plot only contains events which hit near the center of the detector.

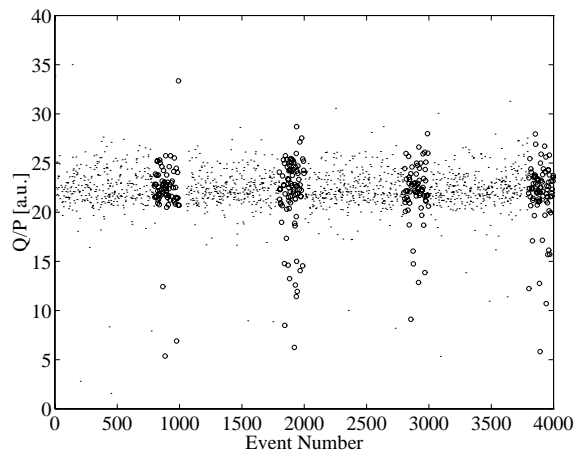


Figure 4.44: Plot showing space charge build up after nearly every 1000 events.

divided by the phonon signal. For events along the gamma line, this is a constant. When acquiring data for this gamma calibration, every 1000 events the crystal was grounded for a minute. This was done to reduce the space charge build up on each electrode. As the detector is exposed to more and more radiation, charges can build up at the two electrode surfaces. These unrecombined charges setup a field which oppose field imposed by the bias. The resulting reduced field in certain areas can yield events with incomplete charge collection. In figure 4.44, I've highlighted with circles the last 300 events before grounding the crystal. From the data, it is clear that the charge collection degrades while the detector is biased. As a result, it is beneficial to only look at the first 700 or so events after each grounding period.

Figure 4.45 are the 2D plots after exposing this detector to a PuBe neutron source. The plot the left side contains all the events which caused a trigger, and the plot the right side is the result of cutting on the position and event after grounding to reduce the number of events due to incomplete charge collection. Basically, this device is also able to discriminate between nuclear and electronic recoils.

IbIs curves

As was mentioned earlier, the IbIs curves are a useful diagnostic when looking at a phonon sensor. Figure 4.46 contains a plot of the IbIs curves as well as plots of quantities which can be extracted from an IbIs curve such as the resistance and power dissipated by the sensor. The IbIs curve in this figure is from the detector with only four phonon sensors. These sensors consist of a parallel array of 2 micron wide by 100 micron long tungsten meanders. In contrast, the IbIs curve in figure 4.47 is from the detector with an ionization electrode. It consists of tungsten meanders which are 2 microns by 400 microns. In both figures, the IbIs curve which appears in the top left corner. The nearly vertical portion in the center of the plot occurs when the sensor is superconducting and the deviation from an infinite slope is due to

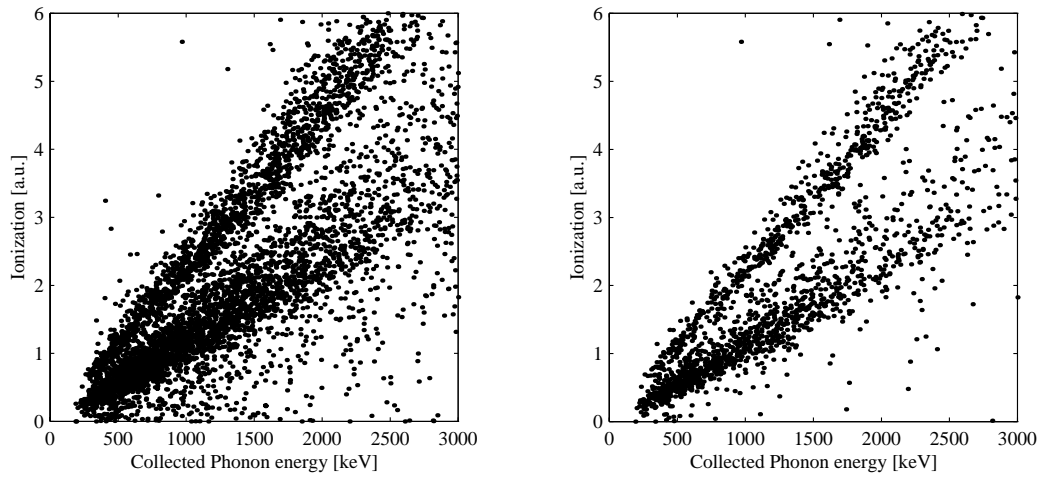


Figure 4.45: Gamma-ray and neutron response of the 4 g detector.

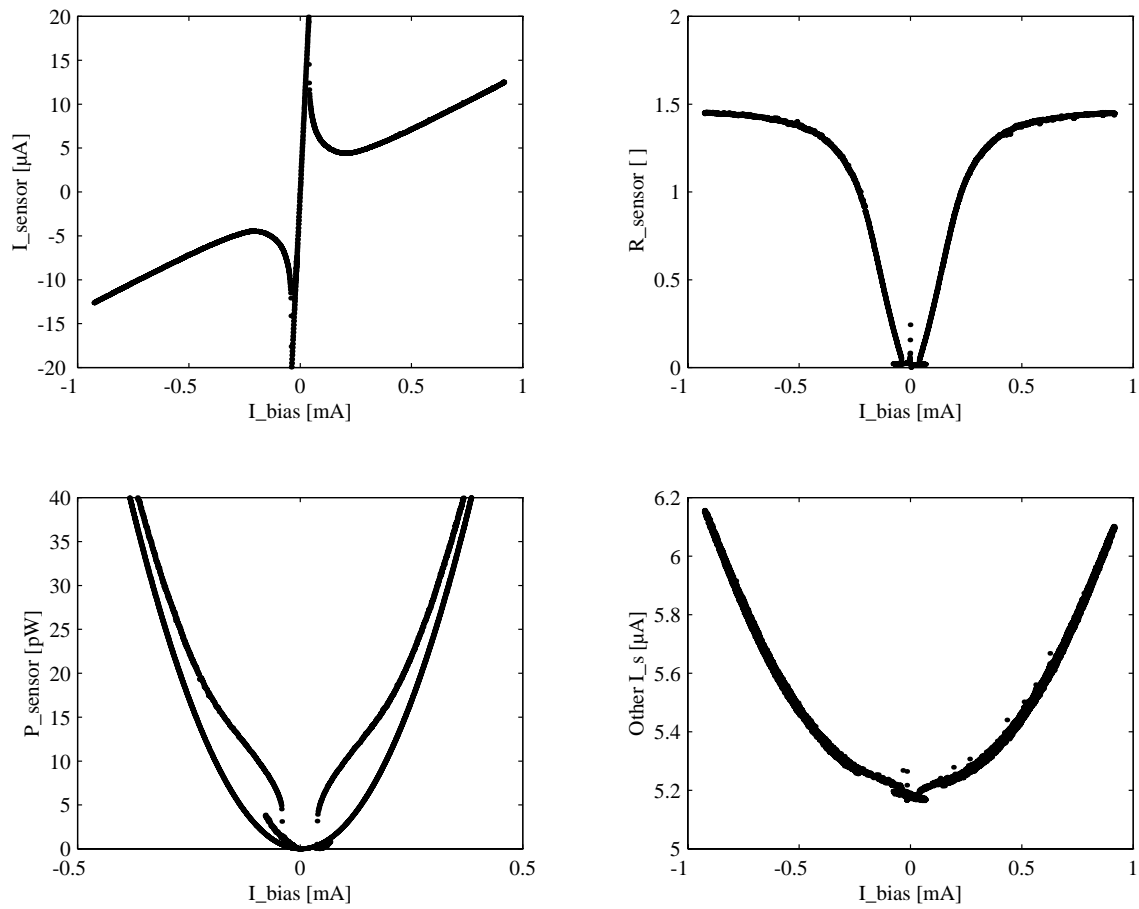
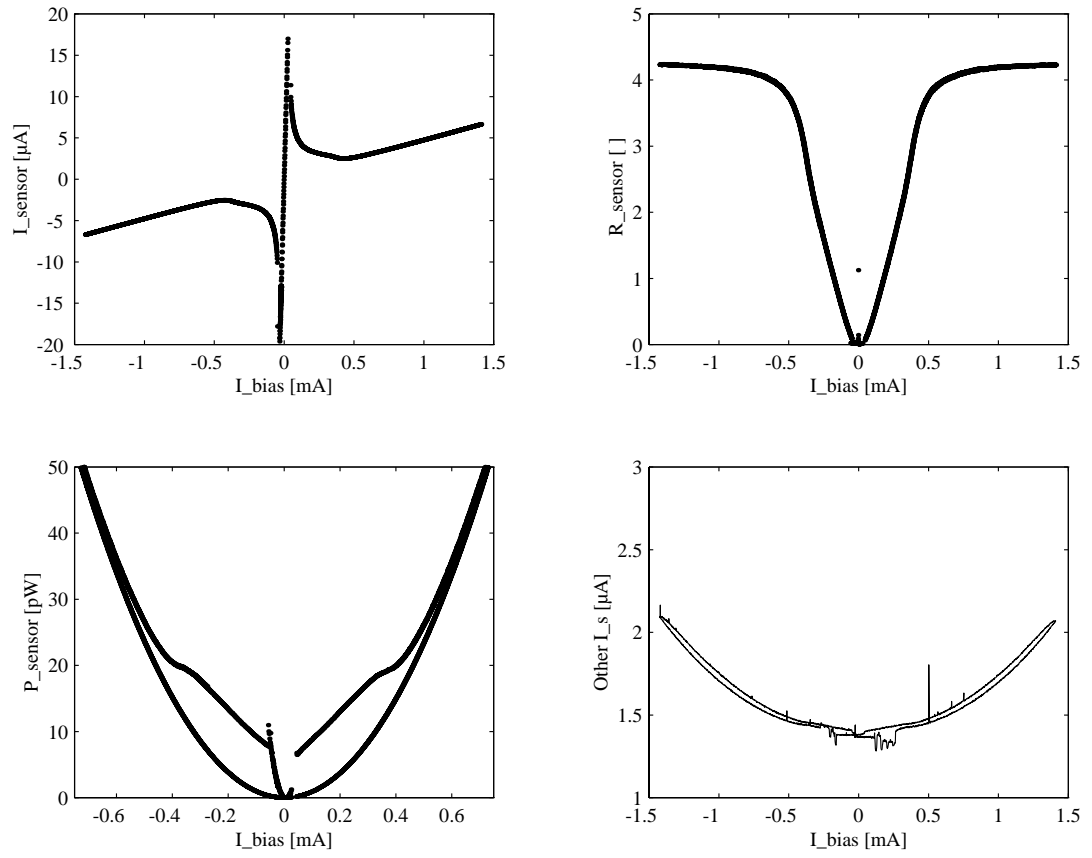


Figure 4.46: IbIs curves for a device with $100\text{ }\mu\text{m}$ tungsten lines.

Figure 4.47: IbIs curves for a device with 400 μm tungsten lines.

stray lead resistance. One would expect the normal resistance to be four times larger in the second device because of its longer length. However, because of variation in feature size control and different numbers of connected parallel pixels, the number isn't exactly four. One of the most interesting plots is in the lower right corner. It is a plot of the sensor current in another sensor which is biased in the middle of its transition. If there were an electrical crosstalk between two sensors, one would expect a linear coupling between the two signals. However, this crosstalk appears quadratic. In fact, I believe it is a sign that there is thermal crosstalk between the two sensors. Basically, when one sensor is driven normal, enough heat is being dumped into the crystal, that the change in crystal temperature causes a small change in the quiescent operating point of the other sensor. In figure 4.47, the rate of change of the bias current is faster than the sweep in 4.46. As a result, there is a small hysteresis loop in 4.47 because the crystal temperature lags slightly. I have observed that the hysteresis loop can be removed by sweeping more slowly.

Heat Sinking

After observing the thermal crosstalk in the phonon only device, steps were taken to improve the heat sinking when running the phonon and ionization device. We choose to evaluate the improvements in heat sinking by measuring the transition temperature for each of the sensors. Figure 4.48 shows the measurement for the four runs. The plot labelled Run 35 was the T_c measured with the original heat sinking shown in figure 4.49. For Run 36, the wires leading to the detector were heat sunk at the mixing chamber instead of coming straight from the 1K pot. In Run 37, I placed a copper shield over the phonon sensor to shield the sensors from direct line of site from the 4K photons coming from the IVC. And finally in Run 39, I added a huge heat sinking crystal shown in figure 4.49.

The initially suprising result was that a copper shield placed over the phonon

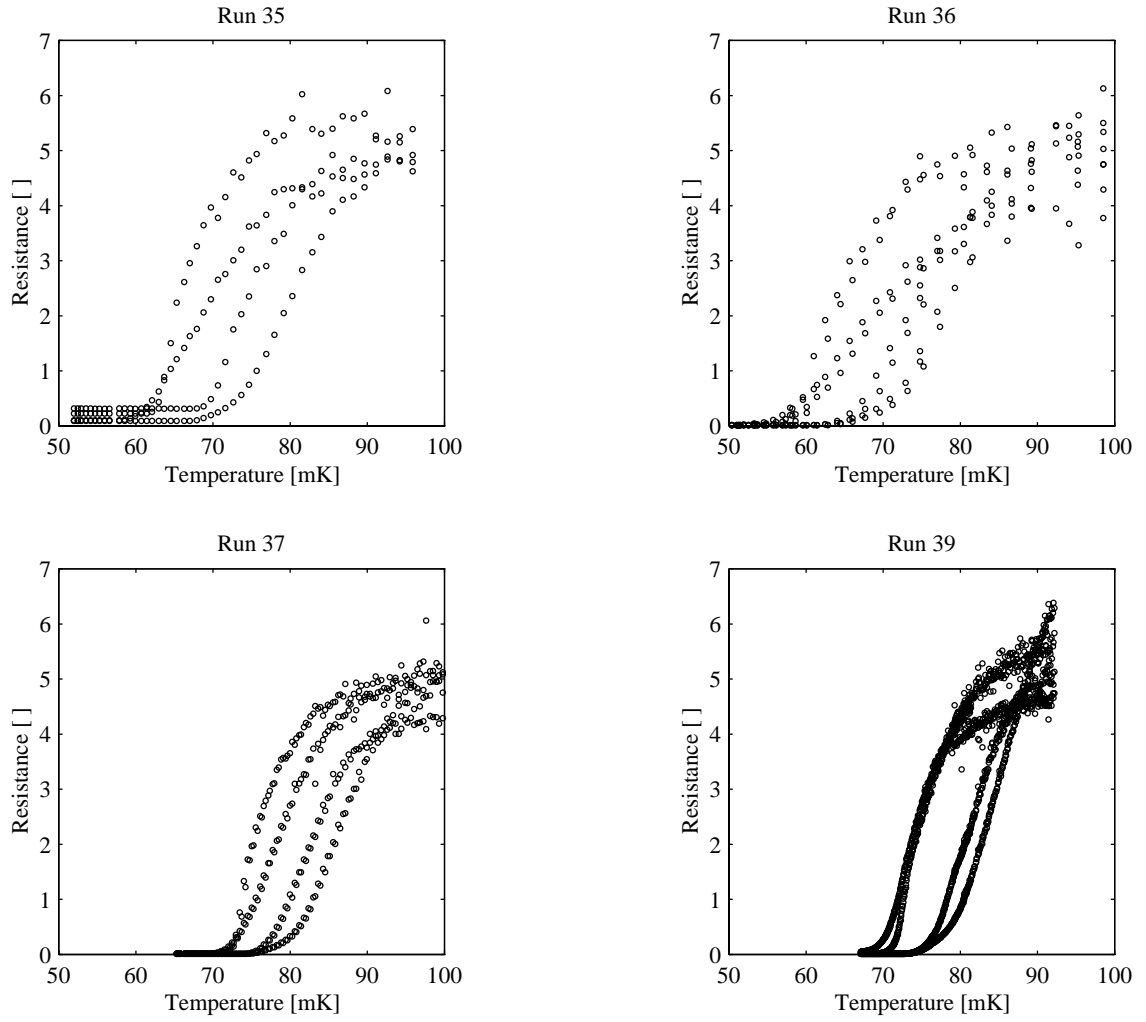


Figure 4.48: Measurement of the W transition temperature with different levels of heat sinking and radiation shielding.

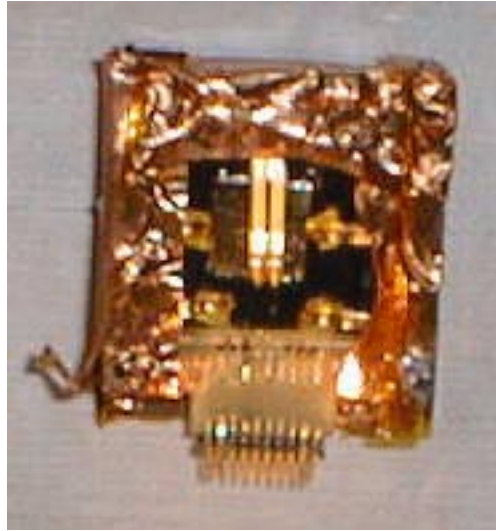


Figure 4.49: Photograph of a heat sink.

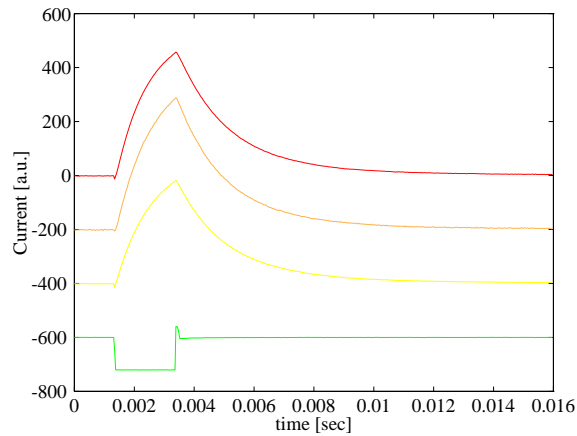


Figure 4.50: Thermal crosstalk between phonon sensors.

sensors shifted the T_c measurement by nearly ten milliKelvin. The black body radiation from the 4K IVC was a heatload on the sensor because the 4K photons were of sufficient energy to break Cooper pairs in the Al which diffused into the W. The only sign that the heat sinking had an effect was that adding a large heat sink reduced the spread in the T_c variation from sensor to sensor. Ultimately, I realized that measuring the T_c for various heat sinking strategies does not really test heat sinking, but heat loading.

Given the thermal crosstalk between sensors, an interesting experiment is to use one sensor as a heater by driving it completely normal, and watch the response of the other sensors. In figure 4.50, I've plotted the results of adding a top hat pulse to the bias of one sensor to drive it completely normal. As expected there is an exponential like rise and fall response in the remaining sensors. In fact, I found that the tails decay with two time constants. The first time constant is 1.7 ms and second is 7.6 ms. The 1.7 ms decay is the dominant term in the decay. My hypothesis is that one time constant is due to the W phonon to Si phonon coupling; and the second is due to the Si to sample holder coupling. Further measurements could be done to resolve this question.

Meander length

Early in the development of the TES phonon sensor design, I realized that there were DC jumps in the quiescent operating current. These jumps seemed to occur after a large event which saturates a sensor was detected. It was hypothesized that such behavior was due to superconducting to normal phase separation along an individual tungsten meander. Based on the model described in chapter 3, an estimate for the maximum length for a meander can be made for no jumps. However, because of large uncertainty in some of the parameters, it was necessary to experimentally test for the maximum length. Figures 4.51, 4.53, and 4.52 are plots of the dc baseline as function of events. For 800 micron meanders, there are clearly baseline jumps. In the 100 micron meander data, there are no jumps. From the plot of the 400 micron data, there appears to be two quiescent bias states. It is difficult to believe that there are two distinct because such an artifact can be caused by poorly tuned SQUID arrays jumping and slightly changing their lockpoint. However, because of the behavior of sensor B, it appears that 400 microns might be close to the edge of a stable uniform meander length.

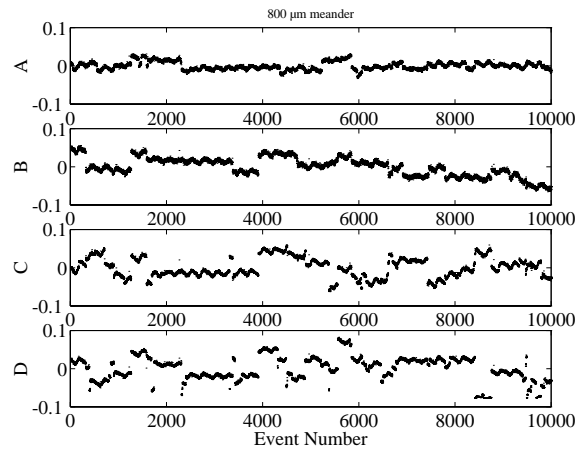


Figure 4.51: DC baseline jumps in a detector with 800 μm tungsten lines.

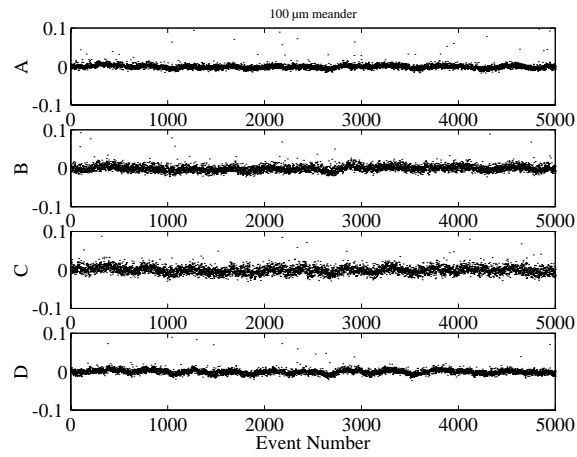


Figure 4.52: No DC baseline jumps in a detector with 100 μm tungsten lines.

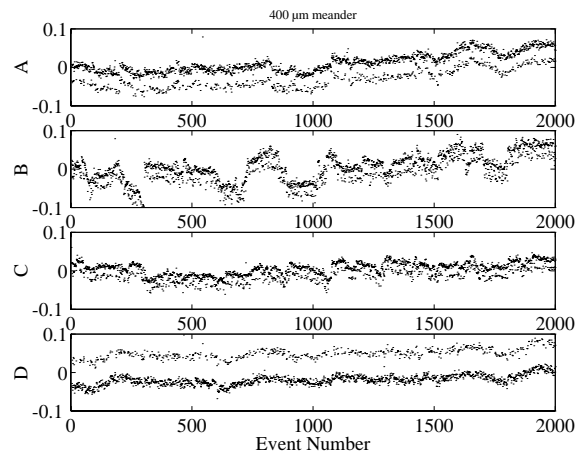


Figure 4.53: DC baseline jumps in a detector with 400 μm tungsten lines.

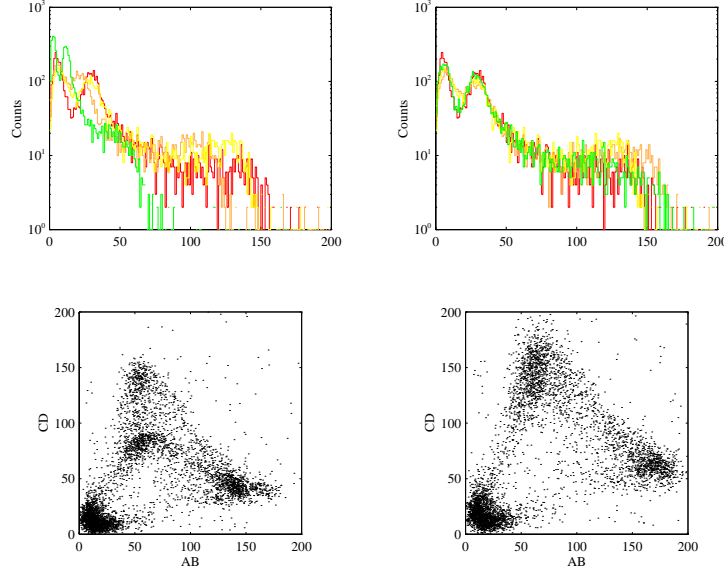


Figure 4.54: Uncorrected (left) and corrected (right) response of the phonon sensors on a 4g detector.

4.3.3 Second Design

To cover a 3in diameter, 1 cm thick detector, we needed to use a new phonon sensor/pixel design. From noise considerations and voltage bias source impedance, it is preferable for the operating point to be around $\frac{1}{4}\Omega$. As a result, a normal resistance of $\sim 1\Omega$ for the W was necessary. Based on the earlier results, we decided to use 1 cm x 1 cm fields on the full wafer detector which could be patterned and tested on 2 cm x 2 cm x 4 mm devices. In each 1 cm² field, there was a 5x5 grid of W meander pixels. A sketch of one appears in figure 4.38 .

Phonon only device

Figure 4.54 summarizes the results from illuminating a detector based on the new phonon sensor pixel design with a 60 keV source. The plots in the left column represent the raw data from the device. In the top plot, histograms of the energy spectrum for each sensor are shown. In the lower plot, the energy collected in AB is

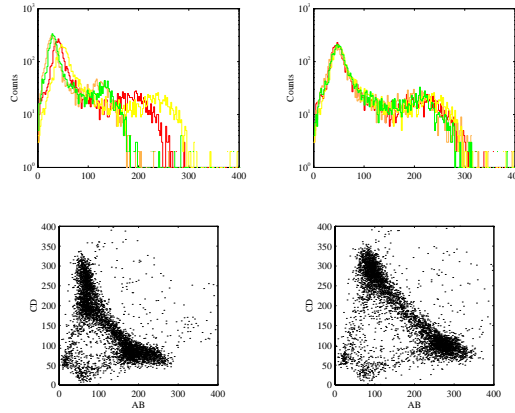


Figure 4.55: Phonon sensor response on a 4g detector in which the IVC walls are below 4K.

plotted versus CD. From the two plots, it is apparent that there is a large difference in performance between sensors. However, if the data from three of the sensors is renormalized so that the collected energy spectra for those three sensors matches the energy spectra of the best sensor, one gets the plots shown in the second column. With one multiplicative factor per sensor which took into account the variation in shunt resistors and damage in one sensor, the histograms overlap and the AB vs CD plot looks more symmetric.

The most significant result from this device is that the energy collected by this device for 60 keV's is one order of magnitude worse than the detectors based on the previous design. One thought was that because the amount of Al quasiparticle collection area per W meander was increased by an order of magnitude, it was possible that the 4K photons from the IVC could be an appreciable heat load which could cause degraded phonon sensor performance.

By pumping on the liquid helium bath, we were able to reduce to the IVC below 4K. The effect on the detector response is shown in figure 4.55. As was expected, there was a performance improvement, but the improvement was only a factor of 1.5. Again the plots on the left side are the raw data, and the plots on the right side

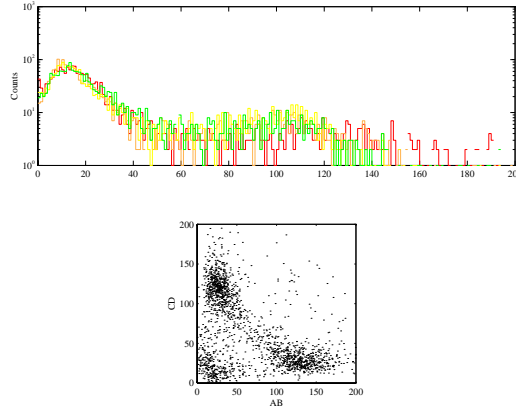


Figure 4.56: Effects on phonon collection in a detector with an Au electrode on the backside.

are plots obtained by symmetrizing the sensor responses.

Effect of a Au electrode

We also fabricated a device with a Au electrode. Figure 4.56 show the effects of a Au electrode on the phonon signals. As we saw in previous devices, the presence of an Au electrode reduces the collected phonon energy by a factor of two.

IbIs curves

In figures 4.57 and 4.58, I've plotted the IbIs curves for one of the phonon sensors on the detector with the Au electrode. As expected the normal resistance is approximately 8 ohms. On the full wafer design, there are 8 1cm x 1cm fields connected in parallel per quadrant of the phonon sensor side. Another important feature is that the power dissipated by the sensor in the self biasing region is roughly constant. This is because the W meander is 200 microns which is sufficiently short to avoid phase separation at lower biases. In addition, the amount of non current carrying tungsten was reduced. In the older designs with shorter meanders, there was a significant length of tungsten between the quasiparticle trap and the biased

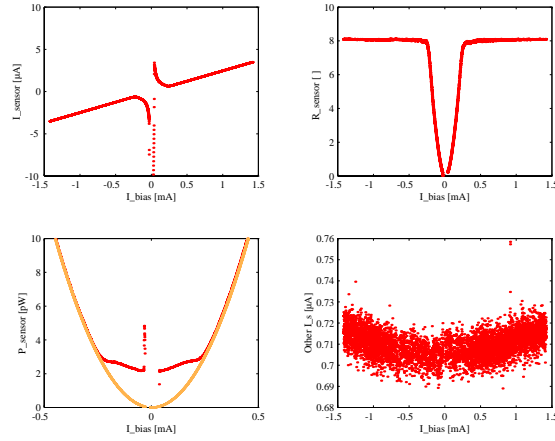


Figure 4.57: IbIs curves for a 4 g detector with the IVC walls at 4 K.

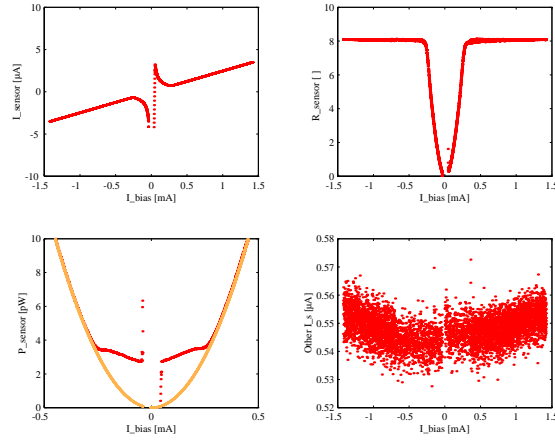


Figure 4.58: IbIs curves for a 4 g detector with the IVC walls less than 4 K.

tungsten. A sketch of an older short meander W pixel and new pixel appears in figure 4.59.

Figure fig:etf45-ibis-pump shows the IbIs curve when the liquid helium jacket is pumped on. As was hypothesized earlier there was less of a heat load on the phonon sensors. As a result the power dissipated in the self biasing state is higher. A plot of the quiescent power as a function of bias current for a 4K IVC and a pumped helium bath IVC is shown in 4.60 . The curve traced by the thin line is the power

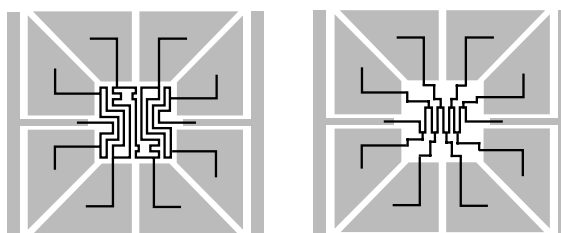


Figure 4.59: A sketch of an old short W pixel and a new W pixel

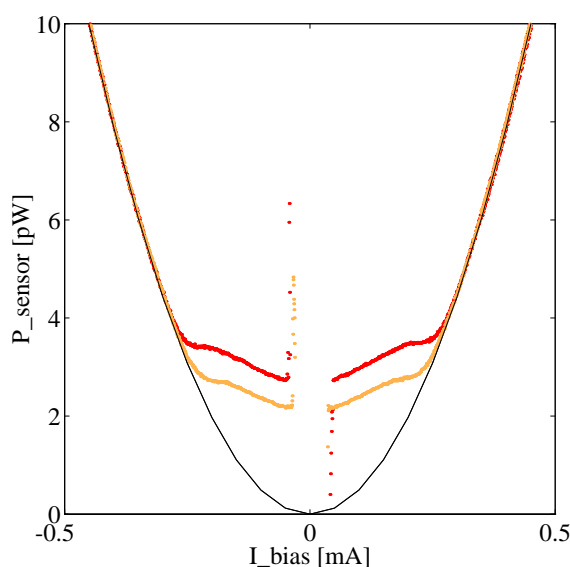


Figure 4.60: Plot of the power dissipated by the sensor when the IVC is less than 4 K (upper curve), when the IVC is 4 K (middle curve), and if the sensor were always normal.

dissipated if the sensor were completely normal. The middle curve is the power curve traced out when the IVC is 4 K, and upper curve it the power curve when the liquid helium jacket is being pumped. It is difficult to fit the IR power loading to the Stephan-Boltzman predicted value because of the uncertainty in the temperature of the pumped liquid helium bath.

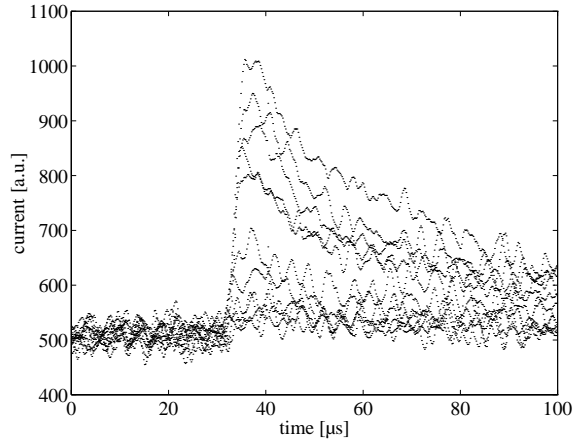


Figure 4.61: Example of pulses from a detector with the new pixel design showing the fast risetime.

Risetimes

The reduction in collection efficiency by a factor of ten was startling. However, the pulse shape gives clues to possible loss mechanisms. Figures 4.61 and 4.62 are plots of the leading edge pulse shapes from devices with the new phonon pixel design and the old design respectively. The pulses are due to a 60 keV source. The most striking feature besides the poorer signal to noise, is the sharp rise time in the pulses with the new phonon design. There is very little variation and is close to being L/R limited where L is the inductance of the SQUID input coil and R is the operating resistance of the sensor. In addition to the fast rise in the pulses, the pulses appear to decay quickly. In fact, the decay time is similar to what is expected to be the ETF time constant. Unlike earlier devices, the diffusion of quasiparticles and the slow arrival of phonon energy does not appear to lengthen the pulse.

4.4 First large Dark Matter detectors

Using the QET phonon sensor design which scales to cover a full 3 in wafer and which we tested in the 2 cm x 2 cm devices, Roland Clarke and Paul Brink made a 100 g

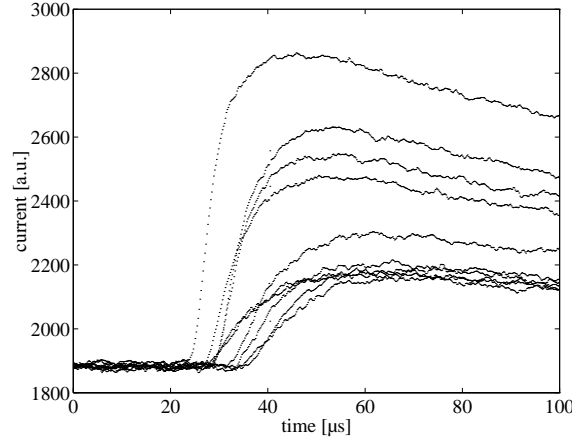


Figure 4.62: Example of pulses from a detector with an old pixel design with slower risetimes.

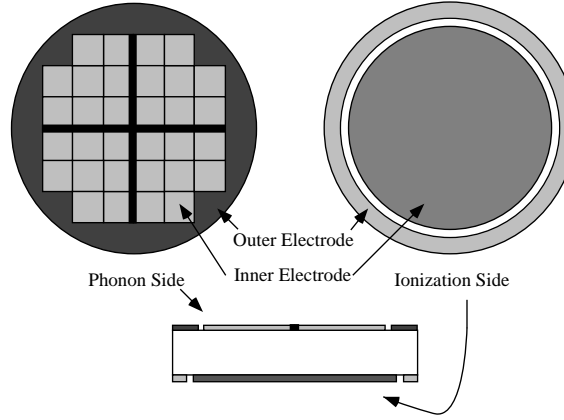


Figure 4.63: Sketch of the first 100 Si Dark Matter detector using QET technology.

3 in in diameter and 1 cm thick Si dark matter detector. Roughly in the space of two years, the research in our group went from a detector with two tungsten pads on a .08 g silicon substrate, to a 4 channel pixelated phonon sensor on a 100 g substrate. A sketch of the first 100g detector appears in figure 4.63 .

In this section, I will briefly present some of the results from the first 100g Si CDMS dark matter detector. The bulk of this work is due to the strong efforts of Roland Clarke, and will be more completely described in his thesis. It is also only through the generosity and graciousness of our CfPA colleagues at UC Berkeley that

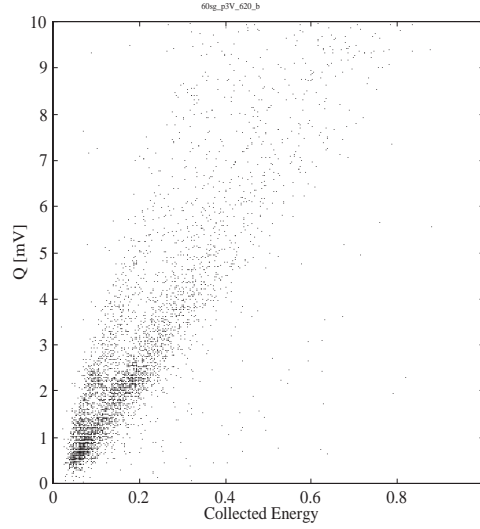


Figure 4.64: Raw 2D plot from a gamma source calibration.

these were results possible. They were kind enough to let us use their “75” facility which is capable of holding and cooling down our 100g detector.

4.4.1 Calibration

The most important test for the dark matter detectors in CDMS is the calibration of the discrimination capability. In figures 4.64 and 4.65, the raw 2D is plotted for the 100g Si detector. From the raw data it is difficult to believe that this detector is capable of discriminating between electronic and nuclear recoils.

However, because of the ability to measure the athermal component of the phonon signal, we are able to understand the source of confusion in the raw 2D plots and correct it.

In our first 100 g detector, we patterned two concentric backside ionization electrodes, a large inner circle and thin outer ring. On the phonon side, a large area of the perimeter is grounded with uninstrumented tungsten. The purpose of this tungsten guard ring was to create a uniform field within the silicon. Unfortunately, this guard ring acts as a phonon absorber and causes a reduction in the phonon

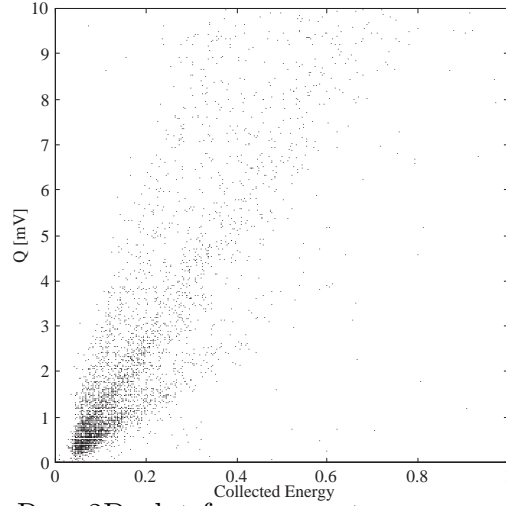


Figure 4.65: Raw 2D plot from a neutron source calibration.

signal for events towards the perimeter of the disc. However, by using the time difference between the arrival of phonon energy at the QET sensors and the start of the ionization pulse, we are able to correct for this loss in collection.

In figure 4.66, instead of plotting the recoil energy vs ionization as in figures 4.64 and 4.65, we plot the arctangent (or angle as it would appear in a 2D plot) of the ratio of total collected phonon energy over charge collected (P/Q) versus the relative delay between the start of the charge pulse and total phonon pulse. Because of the large size of the crystal, there is a significant observable delay. There are four regions of interest. By illuminating the detector with a gamma only source, we were able to determine that regions C and D are due to electron recoils. Events in regions A and B appear with the introduction of a neutron source. As expected, regions A and B are to the right of C and D because nuclear recoils produce fewer e/h pairs causing the ratio $[P/Q]$ to be larger. From the longer delay times, we expect regions A & C to have a lower ratio because they are events which occurred near the perimeter where the phonon collection is less efficient. The inset in 4.66 is a histogram of the arctan of P/Q compensating for the position dependent phonon loss. Thus, we have demonstrated over 99% electron recoil rejection with only 10%

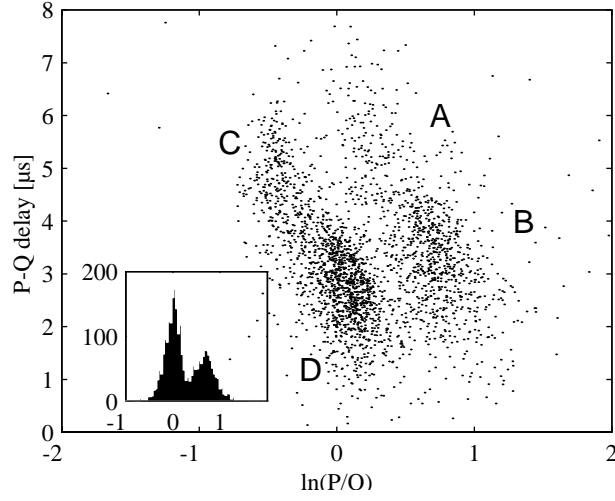


Figure 4.66: Plot of the delay in phonon and ionization pulses as a function of $1/\text{yield}$.

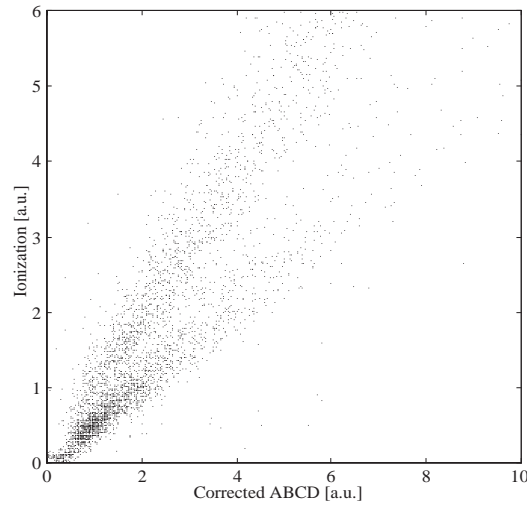


Figure 4.67: Corrected 2D plot of the neutron response.

rejection of nuclear recoil events above a threshold of $\approx 30 \text{ keV}$.

A corrected 2D plot for the neutron calibration appears in 4.67 by boosting the phonon energy for events which occur at longer delays (toward the edge of the crystal).

The two most important advances from running this detector are (1) in scaling by a factor of 25 from the 4g to 100g detector, the collected phonon energy went

from 250 eV to 200 eV for 60 keV gamma events; and (2) the detector is a usable 100g dark matter detector with discrimination capability.

Chapter 5

Simulations

5.1 Phonon Scattering Simulations

To understand the data observed in the larger four channel devices and the 100 g device, I used a simple model for phonon propagation described by Blas [5] and used by Kent in his thesis [22]. In this model, the phonons from an event were assumed to have down converted near the initial interaction site and propagated ballistically. In reality, modeling the anharmonic decay and isotope scattering is complex and very CPU intensive. The approximation that the phonons have anharmonically decayed close to the initial interaction site until they are ballistic and the isotope scattering isotropically scatters the phonons has given qualitatively consistent results in terms of energy partitioning. For the modeling of the phonons at the surface, the phonons were absorbed with a probability of 0.3 at metallized surfaces or scattered diffusively with a $\cos^2(\theta)$ dependence. Per event up to 10,000 phonons were launched and tracked.

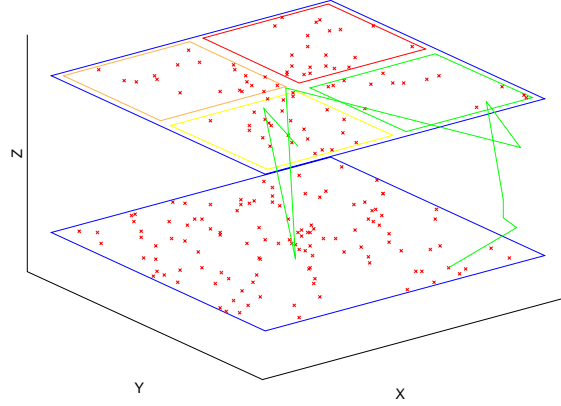


Figure 5.1: Phonon track in a 4g detector.

5.1.1 4-channel devices

Figure 5.1 is a sketch of the geometry of the 2 cm x 2 cm x 4 mm simulated. The phonon sensor side and the electrode sides are drawn. Phonons were launched from a cubic lattice of points throughout the crystal. In this figure, the jagged line is an example of a phonon track. the small “x”s represent where a phonon has been absorbed.

Figure 5.2 summarizes some of the results from one of the simulation runs. In this run, the phonons were launched from a triangular grid of starting points at five different depths (Z) under one phonon sensor on the crystal. At each point, 10,000 phonons were launched and their end points tabulated. Using the eight-fold symmetry of the detector, I mapped the response of the entire detector. For example, the plot on left in figure 5.2 is a plot of the partitioning of energy between the four phonon sensors as if the lattice of starting points were a 19x19x7 cubic lattice spaced every mm in x and y and 0.5 mm in z. The middle plot is the total energy collected within one phonon sensor. The x and y axis represent the x and y starting point of the phonon. The z axis is the negative of the average collected energy for phonons launched for a given x and y position. As one can see from the plot, there are is

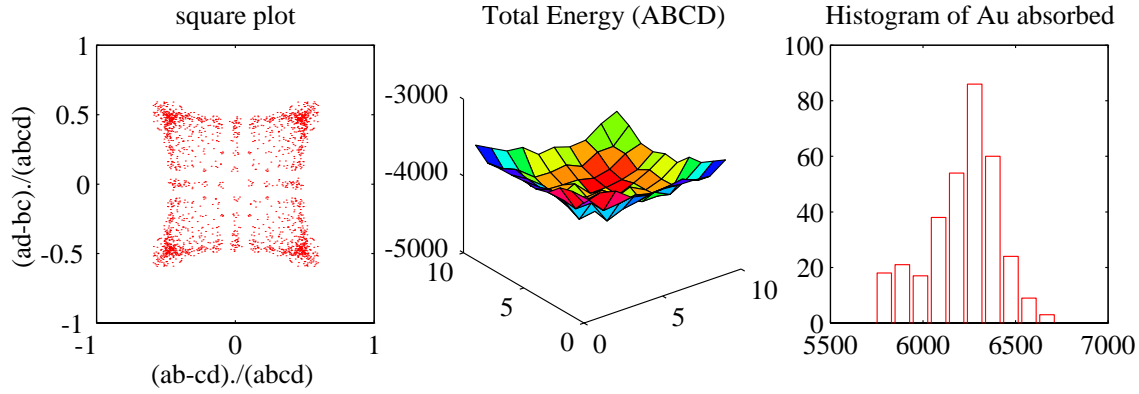


Figure 5.2: Summary of the phonon propagation Monte Carlo in a 4g device.

less complete collection if the starting point is close to the edge of the sensor. The histogram in figure 5.2 represents the number of phonons absorbed by the backside Au electrode.

The graphs shown in the Monte Carlo must be compared to the data taken by exposing the detector to the 60 keV source. The attenuation length of 60 keV gamma rays is a 1.3cm in Si. As a result, the crystal is somewhat uniformly illuminated in depth. Qualitatively, the results of the Monte Carlo agree with the data shown in the previous chapter. However, the real data actually appears to have more of a picture frame appearance and straighter edges. This indicates that there is less sharing of energy between phonon sensors. The real data also appears to have a larger maximum fraction (~ 0.7) of energy absorbed by a single phonon sensor. Again, this is probably due to less sharing because the phonons may not be completely ballistic and due to the fact that I did not simulate the effect of the emission of luke phonons as charges drift accross the crystal and the effect of recombination phonons at the surfaces. The luke phonons will effectively be a vertical line source of phonons and the recombination phonons will be secondary phonon sources located at the same x and y coordinate but at the surfaces. In either case, it will accentuate the signal in one phonon sensor. The monte carlo also gives confidence in our understanding

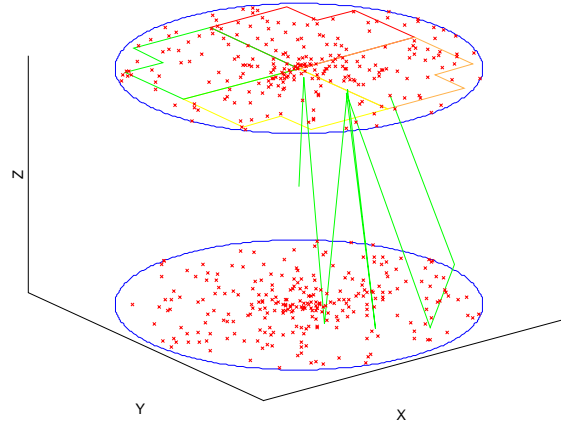


Figure 5.3: Phonon track in a 100 g detector.

of the effect of the backside electrode. We roughly see a half of the phonon energy is absorbed by the gold electrode and that its presence causes a slight dip in the collection efficiency for points between the sensors.

5.1.2 100 g devices

To understand the performance of the first 100 g dark matter device and to test new ideas for improved detectors, I primarily concentrated on starting a reasonable framework for doing phonon monte carlos of the 100 g crystals. Figure 5.3 is a drawing which is not to scale of one of the detector geometries simulated. This particular geometry is to simulate the first 100 g dark matter detector. The top side has four phonon sensors. The surface around the four electrodes is a solid W guard ring. The bottom side is a gold electrode. For simplicity, there is only one solid gold electrode instead of an inner and outer.

In figure 5.4, I've summarized the results from the first attempt at simulating the 100 g detector. In this run, 1,000 phonons were launched from a pie shaped set of points on a rectangular lattice with a 2.5 mm spacing in x and y and a 1 mm spacing in z. The upper left plot is the partitioning of energy between the four sensors.

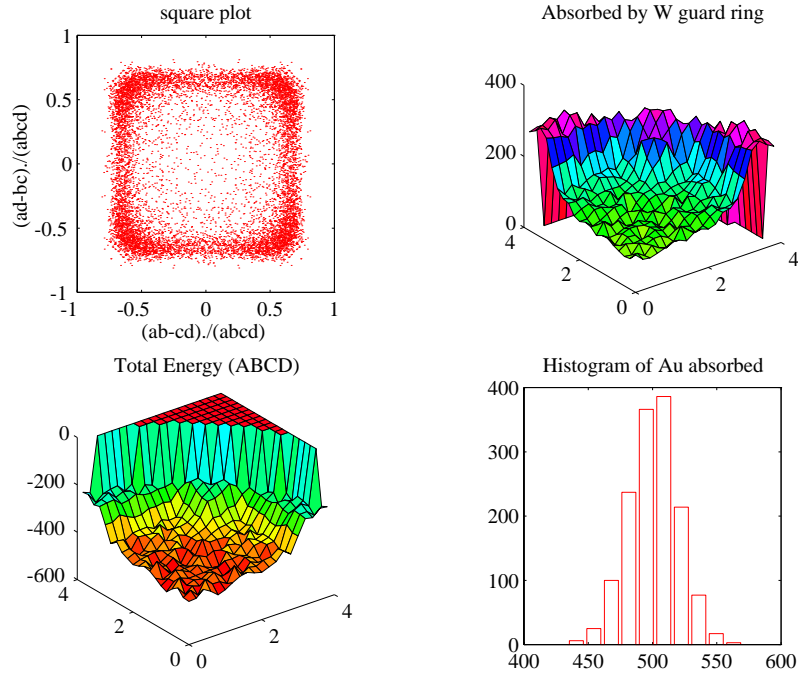


Figure 5.4: Summary of the phonon propagation Monte Carlo.

The lower left plot is the negative of the total collected energy from all four sensors. It is more convenient for plotting to use the negative of the collected energy, and the shelf at 0 along the perimeter are for coordinates outside the crystal and is an artifact from the plotting algorithm. The upper right plot is the number of phonons absorbed in the W guard ring as a function of initial xy phonon position. The lower right plot is a histogram of the number of phonons absorbed in the gold electrode.

One of the nice things from the results of this monte carlo is that the effect of the W electrode is clearly seen and matches the data. Basically, for events which occur towards the edge of the crystal, nearly half of the phonon energy is lost in the W electrode. Although the square image in the partitioning of energy is slightly smaller than the square formed by the data, I believe this effect is from not simulating the luke effect phonons and electron-hole recombination phonons. And as we observed in another 100 g device without a backside electrode, the presence of a gold electrode reduces the phonon signal by a factor of two [9] .

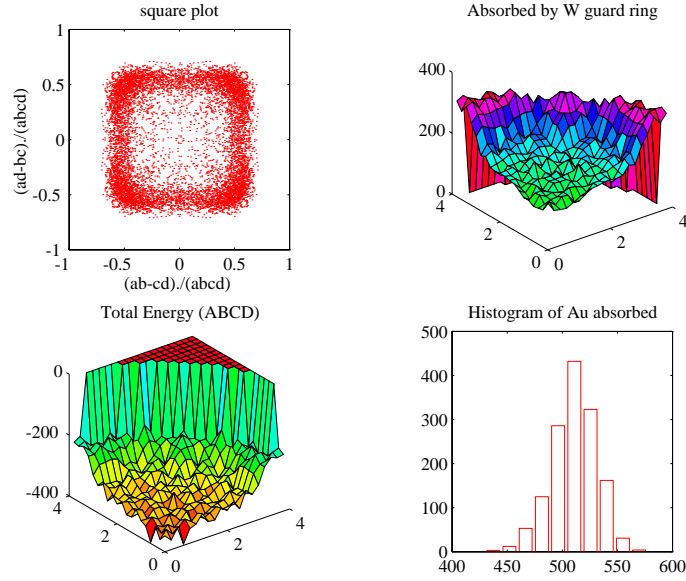


Figure 5.5: Summary of the phonon propagation Monte Carlo in a 100 g device assuming calculated phonon transmission coefficients [37]

In the first monte carlo, I assumed a phonon absorption value of 0.3 for phonons which hit the W guard electrode. From the qualitative success of the phonon monte carlo's run by Blas and previous members of his group, the empirically determined value of 0.3 for phonon absorption coefficient of the aluminum and gold. However, calculations by other groups based on lattice mismatch theories indicate different values. I've summarized the results of using the absorption coefficient values, 0.18 for Al, 0.25 for W, and 0.21 for Au from calculations done by the Munich group [37] in figure 5.5. As a cross check, I also ran the simulation assuming that there was no phonon absorption in the tungsten. This simulation clearly does not agree with the observed data.

New devices

Clearly, the reduction in phonon collection due to the tungsten guard ring is a characteristic of the first 100 g detector, and we would like to reduce this effect. From work done by previous members of our group on high impedance superconducting

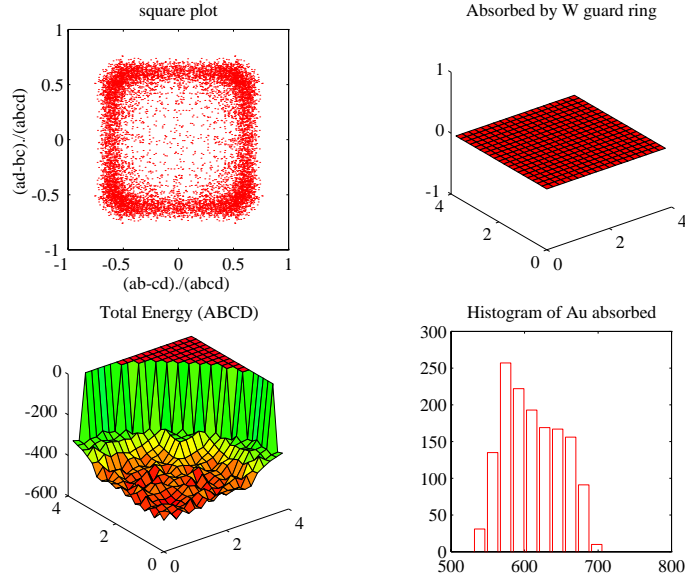


Figure 5.6: Summary of phonon propagation Monte Carlo in a 100 g detector with no absorption of phonons in the outer W electrode.

transition edge sensors [47, 34, 27], it is possible to use a grid electrode which forms an electrode over the same area but with only 10% of the surface covered with metal thin films. Consequently, one would expect significantly less phonon loss. The results from a simulation with a W and Au grid appear in figure 5.7. As expected, there is a dramatic drop in the phonon absorption due to the electrodes. The variation in collection efficiency across the sensor is less than a few percent. Since the time we ran this Monte Carlo, Roland Clarke has fabricated and is using a new generation 100 g detector which has the grid electrode design. It will be interesting to compare these results with the data he is collecting.

Another future test device which I simulated, is a two-sided phonon sensor. One of the biggest sources of contamination in all dark matter searches is radioactive contamination at the surface of the detectors. If a detector can be made which can spatially locate the interaction site of particles hitting the detector in three dimensions, a fiducial detector volume could be defined which would dramatically reduce the effects of surface contamination. A sketch of the design I simulated is

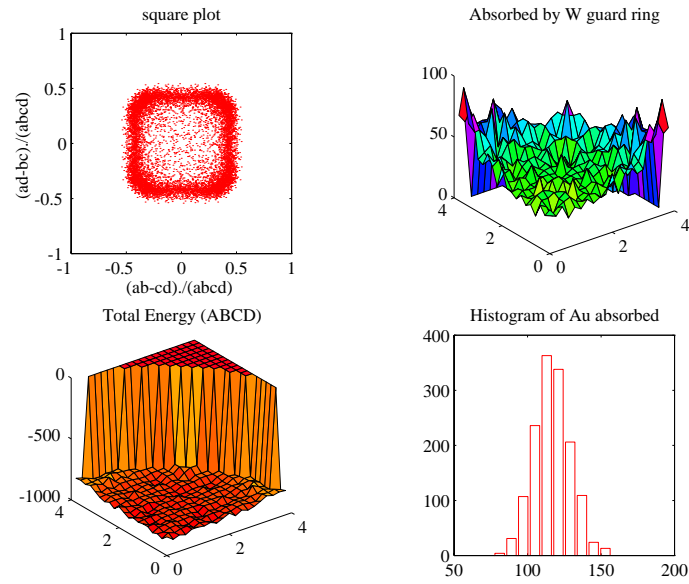


Figure 5.7: Summary of phonon propagation Monte Carlo in a 100 g detector with grided electrodes.

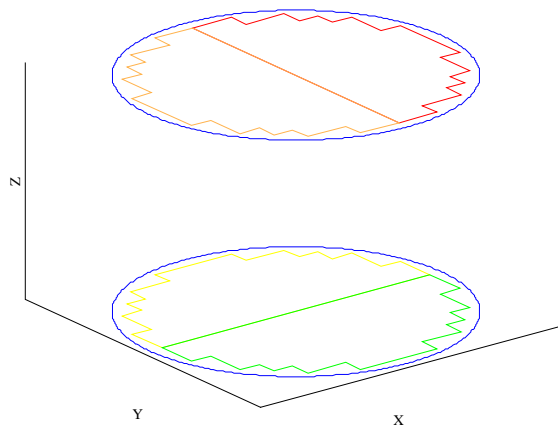


Figure 5.8: Sketch of a future detector design with phonon sensors on both sides.

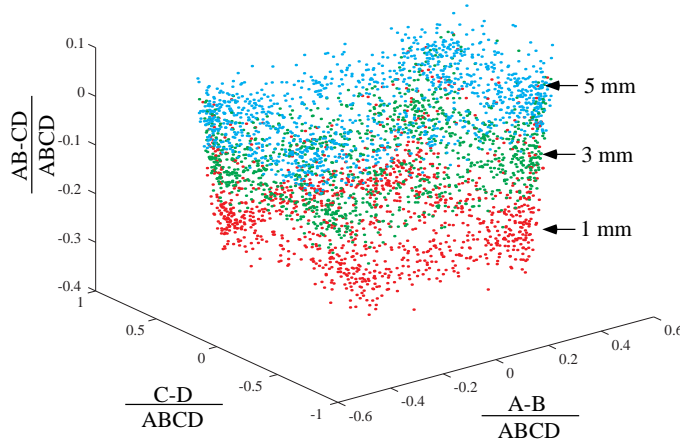


Figure 5.9: Plot showing the partitioning of phonon energy for different event locations.

shown in figure 5.8. Besides the obvious feature of phonon sensors on each side, the shape of the phonon sensor has changed. One of the design improvements which has been implemented by Roland in the large detectors is more surface area coverage of the phonon sensors. The layout shown in figure 5.8 is a modified version of his [8]

Figure 5.9 shows one of the results from the Monte Carlo. In this plot, I've plotted the partitioning of energy into the four sensors in three dimensions. In this figure it is hard to see, but the phonons launched from each depth appear layered in energy partitioning as well. In this plot, the phonons launched at locations 1 mm, 3 mm, and 5 mm from the surface are shown. In this simulations, 5 mm is the in the middle of the detector.

Despite the indications that such a detector design could give spatial resolution, this detector lacks a clear method for discrimination. From my calculations, it is difficult to float the voltage of phonon sensors of one side of the crystal and attach a charge amplifier to each of the phonon sensors. In principle, it can be done, however, because of noise issues and the cryogenic environment it would be a difficult electrical

engineering problem.

5.2 Phonon Sensor

The phonon physics within the crystal is only the first half of the entire FLIP/QET based dark matter detection scheme. The phonon sensing is the other half. In this part, I have looked at the phase separation stability of an ETF sensor in trying to understand the design constraints as well as the diffusion of quasiparticles from the aluminum into the tungsten. I hoped that a simple model could be formed which could qualitatively take input from the phonon Monte Carlos and result in an idea for expected pulse shapes.

5.2.1 ETF Stability

As mentioned earlier in Chapter 2 and observed in the actual data, the meanders in a QET sensor can phase separate into resistive and superconducting regions. This occurs if the thermal conductivity along the line is weaker than the thermal conductivity to the substrate. One limitation of the derivation presented in Chapter 2 is that it assumes that the sensor is always resistive. In other words, it only considers tiny perturbations around the operating point. It does not deal with the possibility of a phase separation.

Previous work by Barron Chugg and Blas Cabrera in our group showed with numerical modeling that the observed IbIs curves which were not truly hyperbolic in the self biasing region could be explained by the onset of a phase separation at lower biases. The power as a function of bias current would initially appear constant at high self biasing currents. However, as the bias current was lowered the power would turn downwards and appear to drop linearly with the bias. From this work,

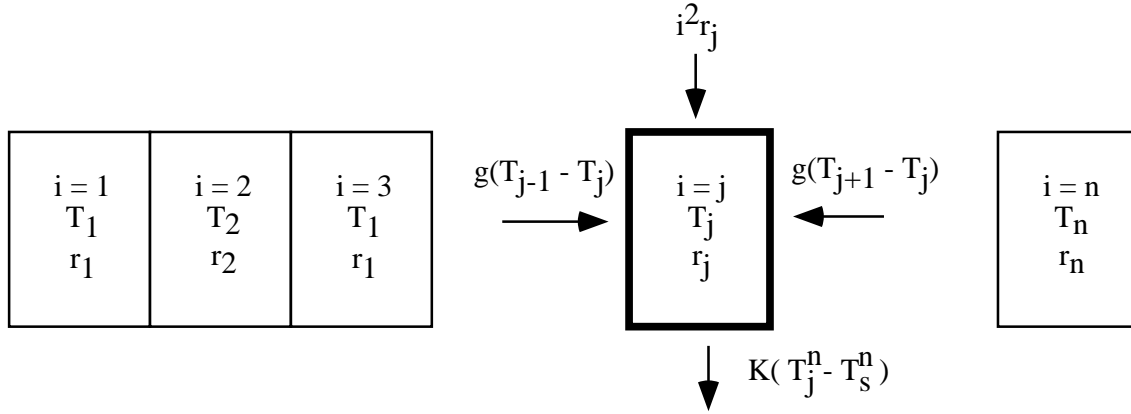


Figure 5.10: Finite difference model of the heat flow in the tungsten meanders.

they were able to verify within an order of magnitude the stability criterion

$$\frac{g_{wf}}{g_{ep}} > \frac{\alpha_o}{n\pi^2}. \quad (5.1)$$

where α_o is a figure of merit for the superconducting transition and n is the exponent in the power law describing the electron-phonon decoupling. I used a different approach to verify this critereon. I modeled the response of the detector to the injection of heat. With this approach, I wanted not only to verify the critereon for no phase separation but also to explore the stability of phase separated solutions. This numerical approach also yields the shape of the pulses from the injection of heat.

Both Barron and Blas's simulations and my simulations are based on using the model shown in figure 5.10. I also modeled the W as a 1D meander for simplicity. In the simulations, I explored several models for the transition region such as constant $\frac{dR}{dT}$, constant α , and the Fermi-function. In addition, I looked at the effects of a constant heat capacity versus a large jump in heat capacity at T_c . Finally, I also tried various power laws in temperature to model the drop in thermal conductivity of the W. As a starting point for the thermal conductivity I assumed the Wiedemann

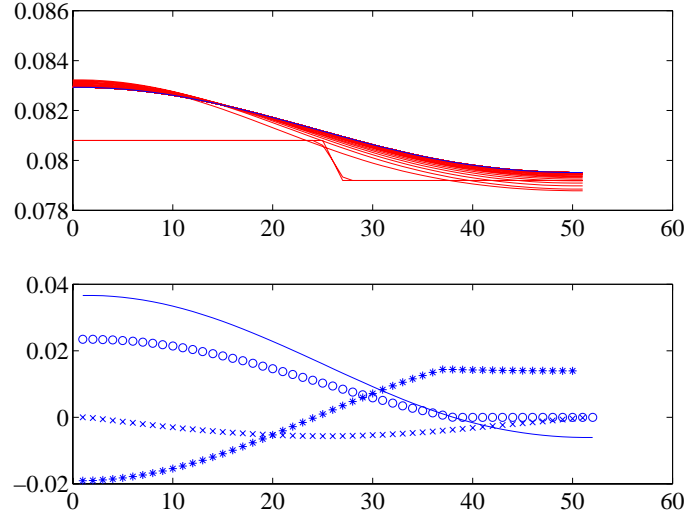


Figure 5.11: Summary of the results of modeling the heat flow in the W meanders.

Franz law where

$$g = \frac{LT}{R}. \quad (5.2)$$

In my modeling, I used T_c for the temperature and normal resistance for R .

An example of one of the simulations appears in figure 5.11. In the upper plot of this figure, I've started with asymmetric temperature profile around the $T_c = 80$ mK and have plotted the temperature profile for at a variety of time steps. In this case, half the meander was started above the T_c and half below. As one can tell, the temperature of the meander evolves towards a phase separated solution. The lower plot is a plot of $\frac{T}{T_c} - 1$ (solid line), $\frac{dT}{dx}$ (x), $\frac{d^2T}{dx^2}$ (*), and resistance (o) as a function of position for the last time step.

In figure 5.12, the response of the meander to heat injected at 8 points is shown. The temperature profile at several time steps is shown in the plot. Initially, the meander cools uniformly to a flat temperature profile. However, because the 8 injection points are not equally spaced because of the discretization of the meander, the very slight non uniformity in heating results in a phase separated cooling solution.

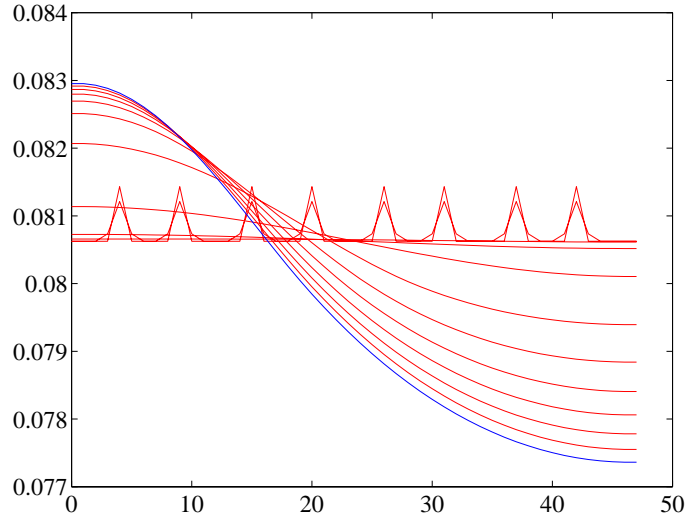


Figure 5.12: Response of the W meander to injection of heat at eight points.

As is typical with numerical problems when one is attempting to determine the value of a parameter which yields stable or unstable solutions, it is difficult to determine the exact value at which instabilities begin. The main difficulty lies in that many small time steps must be taken, and as a result long simulation times are required when the stability criterion is near the stable versus unstable point. However, to first order the criterion derived from a simple linear model around the operating point proved to be correct. Thus, if one starts with a phase separated initial condition when the stability criterion is met, then the solution relaxes to a non-phase separated solution. The effects of altering the details of the resistive transition, the heat capacity, and the thermal conductivity turn out to be much less important than careful measurements of the operating points of the detector which are the starting points of the simulation.

5.2.2 Quasiparticle Trapping

Before any energy is collected and removed via ETF, the athermal phonon energy is collected and injected into the tungsten by the quasiparticle collection fins. One surprise was the loss of energy collection when scaling the phonon sensor design. Because the collection efficiency is poor but similar in both the 4 g device and the 100 g detector, the inefficiency must not be related to the phonon collection. The most likely candidate is an effect related to the fact that the most significant design change was the size of the aluminum fins. They went from being 150/300 μm right triangles to 1 mm² squares. In the early pixel designs for small devices, trapping only occurs in the regions of tungsten which are those close to the edge of the Al/W interface. Trapping is not occurring in the tungsten which is patterned deep within the aluminum because the aluminum has proximitized the tungsten so that it is superconducting. So at best the effective trap area for the old design is a micron (\sim coherence length in Aluminum at best) times the spur/meander width of 2 microns. One design criteria that was appropriately considered was the ratio of trap area to aluminum coverage. The revised pixel design has an overlap 1 micron deep and 40 microns wide so that the effective trap area increased by a factor of 20 for a phonon collection area that only increased by a factor of 10. Another issue with enlarging the aluminum coverage is the quasiparticle diffusion and collection time. We now believe that this is what limits the phonon collection efficiency.

To get a sense for the quasiparticle collection time, I simulated the quasiparticle diffusion using the simplist model:

$$\frac{dn}{dt} = D\nabla^2 n \quad (5.3)$$

where n is the number density of quasiparticles and is a two dimensional function. For simplicity, I did not add a term proportional to n^2 to simulate the effects of

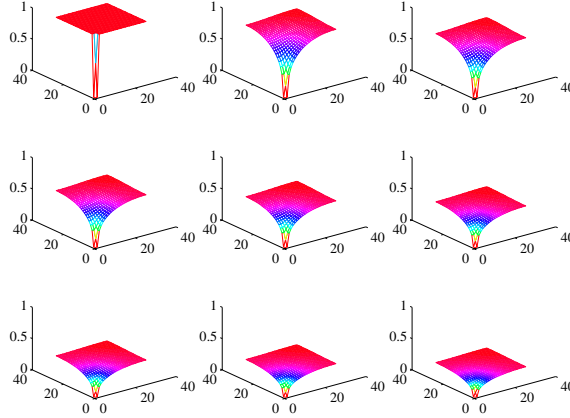


Figure 5.13: Time evolution (left to right and top to bottom) of quasiparticles assuming a simple diffusive model.

quasiparticle recombination. For the diffusion constant, I assumed a $D = 400 \text{ cm}^2/\text{sec}$ which is based on a simple estimate of $D = v_{fermi}l/3$ where l is the mean free path. From the resistance ratio measurements of the aluminum and using the Drude model, we found that l is thickness limited.

Figure 5.13 shows snapshots of the density profile for various time steps in the simulation. The W trap was placed at the origin and neumann boundary conditions were assumed elsewhere. The initial condition was that the pad was uniformly illuminated. Basically, this is a model of the impulse response of the pad. The slower decaying curve in figure 5.15 shows the flux of quasiparticles as a function of time. The decay time constant is on the order of $100 \mu\text{s}$. This is of order of measurements and estimates of the quasiparticle lifetime [15, 44, 25, 17]. However, adding such an n^2 term to account for quasiparticle lifetime can only account for a factor of two loss. Furthermore, such a loss mechanism would have been worse in earlier devices as well. Another more likely possibility is the presence of trapped magnetic flux in the aluminum. For example, if the spacing of flux quanta is on length scales larger than the size of the largest first generation aluminum fins ($\approx 150 \mu\text{m}$), the magnetic flux sites could be the sites where quasiparticle trapping or recombination could take

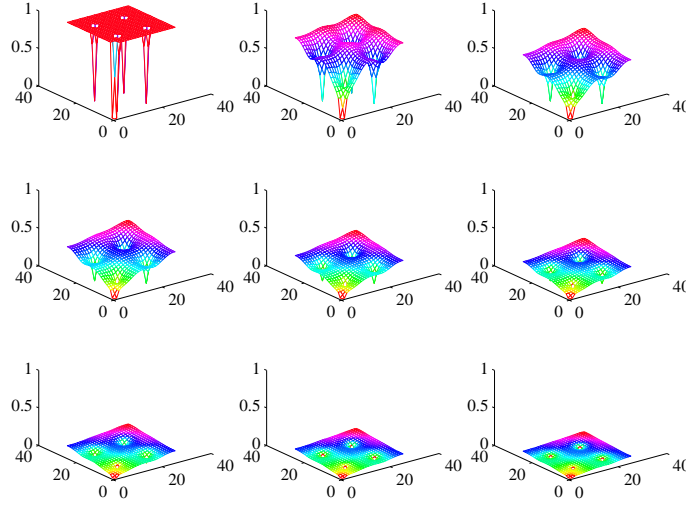


Figure 5.14: Time evolution (left to right and top to bottom) of quasiparticles assuming a simple diffusive model and four recombination sites possibly due to magnetic flux.

place.

Figure 5.14 shows the effects of adding four magnetic flux lines on a square lattice spaced at $500 \mu\text{m}$. In figure 5.15, the curve with the fast decay time is the flux of particle incident on the tungsten trap. In this case, the collection time constant is over an order of magnitude faster and the total collection is down by just over a magnitude. As a result, the presence of trapped flux within the aluminum is a strong candidate for the cause of reduced collection efficiency in the detectors.

Another possibility is that there exist local variations in the quality of the aluminum film which results in local variations in the superconducting gap. Quasiparticle trapping can occur if the quasiparticle energy relaxes to the superconducting gap which is a local minima.

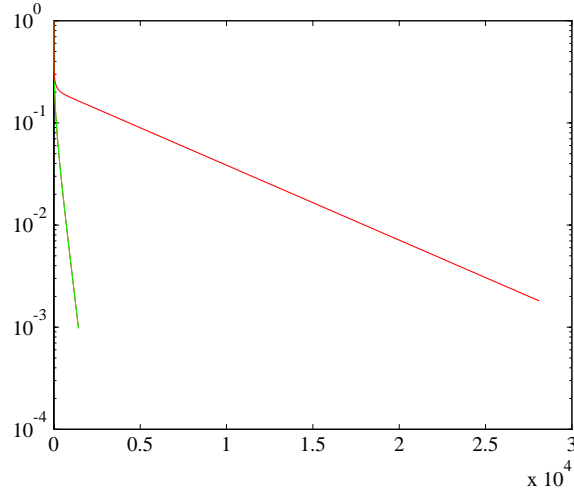


Figure 5.15: Flux of quasiparticles from the Aluminum fin into the W with and without trapping sites.

5.3 Putting it all together

There are two obvious techniques to extract the position information from the signals in a FLIP dark matter detector. One is to simulate or derive the dependence of the measured quantities as a function of position from a set of fundamental concepts. The second is to use a source of radiation and information about where the radiation interacts in the crystal and attempt to deconvolve the known position distribution from the distribution of measure quantities. Both techniques are difficult. In the data presented in the previous chapter, some of the position dependence was extracted by using collimated sources. In my modeling, I hoped to get a first order estimate of the dependence on the position sensitivity of the various signals by simulating the phonon propagation, quasiparticle diffusion, and ETF-TES response.

It is difficult to present all the data from this type of simulation. Figure 5.16 is an example of the output from simulations of the first 100 g dark detector. From the position indicated in the figure which is directly under one of the sensors, a 1000 phonons were launched. The upper plot is the number of phonons absorbed by each sensor as a function of time. To get the phonon arrival times, length of the

trajectory of each phonon was recorded. This distribution of lengths was divided by an estimate of the ballistic phonon velocity ($\sim 5 \text{ mm}/\mu\text{sec}$). Assuming the phonon flux absorbed by the sensor shown in the top plot is analogous to a uniform generation of quasiparticles within the aluminum and assuming a few microsecond collection time based upon the results from the modeling described in the previous section which includes the effect of trapped magnetic flux, the resulting flux of quasiparticle (or energy) trapped into the tungsten is shown in the middle plot. Finally, convolving the ETF time constant with the middle plot, gives a prediction for the pulse shape shown in the bottom plot.

At first glance the results of the simulation which combined the phonon flux, quasiparticle trapping with magnetic flux trapping, and ETF sensor response are not useful because of the results are nearly an order magnitude off in the time. However, I think the shape of the simulation indicates that if one believes that the arrival of phonon energy occurs over long time scales such as $100 \mu\text{sec}$, than because of the quasiparticle diffusion and ETF time constants (2 and $40 \mu\text{sec}$ respectively), the pulse would evolve with a leading edge dominated by these two time constants. Because the observed pulses have a much faster rise time, I believe that the phonon flux would be more accurately modeled as having two components. The first would be extremely fast and contain most of the energy. The second would be slower and decay with a time constant on the order of 100 microseconds. The net result would be a pulse with a rise time which is dominated by the quasiparticle diffusion and phonon arrival time constants. The pulse would initially decay with the ETF time constant but eventually decay with the second but longer phonon decay time constant.

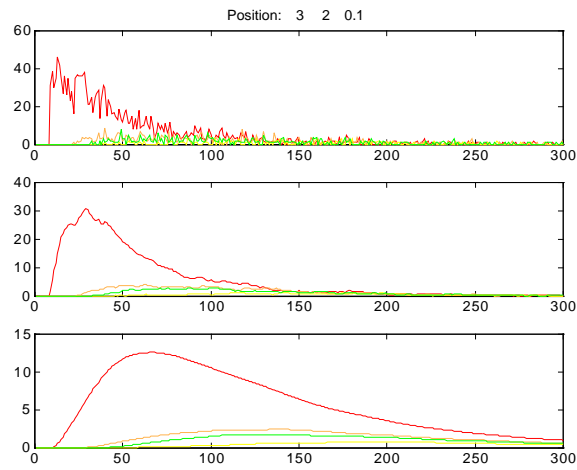


Figure 5.16: The upper curve is a plot of the phonon flux incident upon each sensor based on the phonon Monte Carlo. The middle graph is a plot of the flux of energy (quasiparticles) from the aluminum due to the phonon flux based on the previously described diffusive model. The bottom graph is the predicted pulse shapes taking into account ETF.

Chapter 6

Conclusions

6.1 Design constraints for the phonon sensor

The bulk of this work has been understanding the design constraints for the QET phonon sensors for the dark matter detectors. Starting with the tungsten active element, one of the important restrictions is the limitation placed by phase separation:

$$\frac{g_{wf}}{g_{ep}} > \frac{\frac{\alpha_o}{n} - 1}{\pi^2}. \quad (6.1)$$

It is useful to rewrite $\frac{g_{wf}}{g_{ep}}$ with geometrical and materials parameters by using the approximation that $g_{ep} = \frac{nP_o}{T_c}$ and $g_{wf} = \frac{LT_c}{R_n}$:

$$\begin{aligned} \frac{g_{wf}}{g_{ep}} &= \frac{LT_c^2}{ni_o^2 R_n R_o} \\ &= \frac{LT_c^2}{nJ_o^2 \rho_n \rho_o l^2} \end{aligned} \quad (6.2)$$

The stability critereon then becomes

$$\frac{LT_c^2}{J_o^2 \rho_n \rho_o l^2} > \frac{\alpha_o}{\pi^2}. \quad (6.3)$$

Assuming that the physical parameters of the tungsten are reasonably reproducible such as the T_c , J_o , and α_o , then the length of the tungsten sensor has the following length restriction,

$$l^2 < \frac{LT_c^2\pi^2}{J_o^2\rho_n\rho_o\alpha_o} \quad (6.4)$$

From experimental data, the tungsten meanders fabricated in the devices fabricated at CIS at Stanford, the upper limit for l appears to be $\sim 400 \mu\text{m}$. This roughly agrees with the stability criterion based on rough estimates for the α_o of our devices. For example, in the device shown in figure 4.60, we measured an operating current of $1 \mu\text{A}$ at an operating resistance of 1Ω , a normal resistance of 8Ω , and a T_c of 80 mK . Using the fact that the meanders in this device were of $200 \mu\text{m}$ long, we find an upper limit for l which is ~ 400 assuming an α of 100. A second restriction on the active tungsten is due to the readout electronics. To preserve the fast rise time on order of $1 \mu\text{s}$, the $\frac{L_{\text{input}}}{R_o}$ must be $1 \mu\text{s}$. At the moment, the target input coil inductance for the SQUID arrays is $.25 \mu\text{H}$. As a result, the operating resistance, R_o must be greater than $.25 \Omega$. Another design consideration is the noise due to the Johnson noise of the sensor and the SQUID readout. At the moment, the current performance of the SQUID arrays is $\sim 5 \text{ pA}/\sqrt{\text{Hz}}$. The Johnson not including the effects of electrothermal feedback is $\sim 4 \text{ pA}/\sqrt{\text{Hz}}$ for an operating resistance of 0.25Ω . Although, the Johnson noise is suppressed by ETF [22, 31], the phonon noise is comparable to the unsuppressed Johnson noise. As a result, given the current noise performance of the SQUIDs, it is desirable to operate at as low as operating resistance as possible so that the sensor noise dominates.

The real trick which makes it possible to fabricate large dark matter detectors is quasiparticle trapping. As it happens, it is relatively straightforward to fabricate aluminum in which quasiparticle lifetimes are sufficiently long that it can diffuse several hundred microns on tens to hundreds of microsecond time scales. However,

as was seen with the second generation phonon sensor, quasiparticle collection can be difficult in large collection fins (1mm). It is likely that trapped magnetic flux or spatial variation in the superconducting gap in Aluminum limits the collection efficiency in this case.

6.1.1 Performance

One of the coolest features of using athermal phonon detectors is the ability to extract position information. With the work on smaller devices, we were able to conclusively demonstrate 0.2 mm FWHM xy-position towards the middle of a 1 cm x 1 cm x 1 mm detector for 6 keV gammas hitting the side opposite the phonon sensors. Even with the larger detectors, both by looking at the partitioning of energy or delays in the start of signals, it was possible to extract useful position information.

At the present time, good phonon sensor performance is only part of the requirements for a dark matter detector. By evaporating a metallic electrode on the side opposite the phonons, we were able to simultaneously measure the ionization generated by a particle hitting the silicon substrate. By simultaneously measuring the phonon energy and amount of ionization, we were able to demonstrate the ability to discriminate electronic and nuclear recoils. In the smaller devices the gamma rejection was greater than 99% down to approximately 10 keV in recoil. This value was limited by the microphonic noise in the ionization channel. In the first 100 g dark matter detector, the rejection was 99% down to 30 keV recoil energy. The main problem was the poor quasiparticle collection.

6.2 Current and Future detector work

At the present time, there has already been a huge improvement in the detector performance since the work described in my thesis. Roland Clark has been able to

take advantage of the things learned in the early devices and first 100 g detector. He has implemented a new FLIP improvements in phonon sensor design [8] with respect to the amount of tungsten and quasiparticle traps which were made smaller and designed to reduce trapped flux. He also has implemented a grid electrode system to reduce the athermal phonon absorption by the electrodes. The result has been a improvement in the phonon sensor collected energy by a factor of 10.

In addition to the Roland's excellent work, Josef Jochum and Pierre Colling have designed, fabricated and begun testing devices to measure the detailed performance of the aluminum quasiparticle traps. I believe that these measurements will be useful not only for further optimization of the phonon detectors but also for developing accurate models to simulate the quasiparticle diffusion in the aluminum. Furthermore, I believe that more work with this quasiparticle diffusion modeling and the existing modeling of the ETF in the W will make it possible to begin to understand time evolution of the phonon flux hitting the sensors. With this information, it may be possible to begin deconvolving three dimensional information from the signals.

Work has already started to fabricate detectors using a Ge substrate. Betty Young, Roland Clarke, Andrea Davies, and Pierre Colling have all been working in this direction. There is a clear advantage to using Ge as the target material for dark matter because it has a higher cross section for a interaction WIMPs.

6.3 CDMS

For most of the past couple of years, instead of writing my thesis, I've been working with people in the CDMS collaboration to operate the BLIP and FLIP detectors in an experiment to detect dark matter. I have primarily focused on seeing results with the FLIP detectors.

Just as scaling the FLIP detectors from 1/4 g to 100 g required solving a host

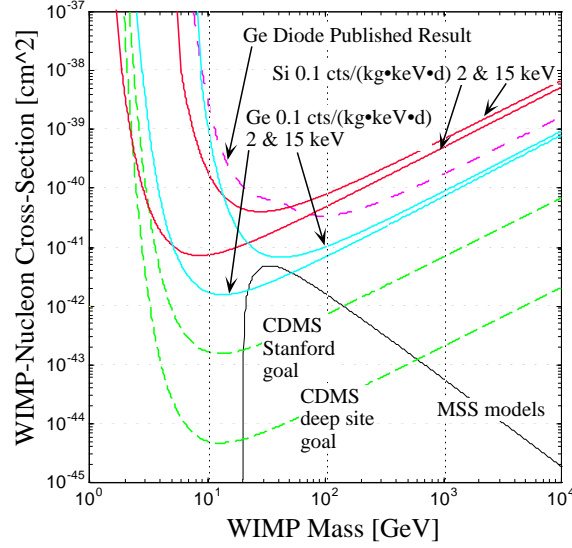


Figure 6.1: Experimental sensitivity to estimating the WIMP cross section.

of interesting problems, getting the CDMS experiment started and looking for dark matter has its own set of new and interesting problems. Although in this case most of the problems were logistical and not really related to detector physics. Nevertheless, working and solving problems like long term data acquisition, fully computerized SQUID and detector biasing electronics, and data analysis of large data sets has been necessary to obtain interesting results. Figure 6.1 shows the goals of the CDMS experiment at the Stanford site and the deep site at Soudan (1/2 mile underground).

Preliminary results from the first 100 g FLIP detector and BLIP detectors has yielded interesting and encouraging results. The ability of the detector technologies to discriminate between electron and nuclear recoils with good energy resolution and threshold has helped increase our understanding of the backgrounds at our site. Although the results on dark matter limits from the first Si FLIP detector with its high threshold are not close to the goals at the Stanford site, work has been proceeding swiftly to improve the threshold and discrimination at lower energies. In Figure 6.1, one can see the significance of discrimination and lower thresholds

for a given background event rate. For reference, the upper dashed line is the best published dark matter result using Ge diode detectors [19] .

The lowest solid line is the upper limit of possible WIMP cross sections predicted using Minimal Supersymmetry Models (MSSM). The other solid lines are calculated (potential) dark matter limits as a function of detector threshold for Ge and Si target materials assuming a nuclear recoil background rate of 0.1 counts/kg/keV/day.

With the factor of ten improvement demonstrated by R. Clarke, it is now possible for a Si FLIP detector to set a new dark matter limit at low WIMP masses. Hopefully, within the next year, a Ge FLIP detector will be fabricated. With such a detector, we expect to achieve the goals of the Stanford site and set a new dark matter limit accross the entire interesting mass range.

Bibliography

- [1] C. Alcock, R. A. Allsman, D. Alves, T. S. Axelrod, D. P. Bennett, K. H. Cook, K. C. Freeman, K. Griest, J. Guern, M. J. Lehner, S. L. Marshall, B. A. Peterson, M. R. Pratt, P. J. Quinn, A. W. Rodgers, C. W. Stubbs, and W. Sutherland. First observation of parallax in a gravitational microlensing event. *Astrophysical Journal, Letters*, 454(2, pt.2):L125–8, 1995.
- [2] Neil Ashcroft and David Mermin. *Solid State Physics*. Holt, Rinehart and Winston, New York, 1976.
- [3] K. G. Begeman, A. H. Broeils, and R. H. Sanders. Extended rotation curves of spiral galaxies: dark haloes and modified dynamics. *Monthly Notices of the Royal Astronomical Society*, 249(3):523–37, 1991.
- [4] Paul Brink. *Non-Equilibrium Superconductivity induced by X-ray Photons*. PhD thesis, Magdalen College, Oxford University, 1995.
- [5] Cabrera, 1993.
- [6] Blas Cabrera. Status report. Technical report, Stanford University, October 1998.
- [7] J. A. R. Caldwell and J. P. Ostriker. The mass distribution within our galaxy: a three component model. *Astrophysical Journal*, 251(1, pt.1):61–87, 1981.

- [8] R.M. Clarke, P.L. Brink, S. Nam, et al. Operation of an improved 100 g Si FLIP detector for the CDMS experiment. In Susan Cooper, editor, *Proc. of the Seventh Int. Seventh International Workshop on Low Temperature Detectors LTD-7*, pages 82–95. Max Planck Institute of Physics, 1997.
- [9] Roland Clarke. Ph. d., Stanford University, to be published.
- [10] A. Dekel, E. Bertschinger, A. Yahil, M. A. Strauss, M. Davis, and J. P. Huchra. Iras galaxies versus potent mass: density fields, biasing, and omega. *Astrophysical Journal*, 412(1, pt.1):1–21, 1993.
- [11] A. Dekel and M. J. Rees. Omega from velocities in voids. *Astrophysical Journal, Letters*, 422(1, pt.2):L1–4, 1994.
- [12] S. Dodelson, E. I. Gates, and M. S. Turner. Cold dark matter. *Science*, 274(5284):69–75, 1996.
- [13] C. Enss, and G. Seidel private communication, Brown University and D. D . Osheroff, private communication, Stanford University.
- [14] K. Freese and D. N. Schramm. General cosmological constraints on the masses of stable neutrinos and other 'inos'. *Nuclear Physics B, Particle Physics*, B233(1):167–88, 1984.
- [15] S. Friedrich, K. Segall, M. C. Gaidis, C. M. Wilson, D. E. Prober, A. E. Szymkowiak, and S. H. Moseley. Experimental quasiparticle dynamics in a superconducting, imaging x-ray spectrometer. *Applied Physics Letters*, 71(26):3901–3, 1997.
- [16] E. I. Gates, G. Gyuk, and M. S. Turner. Gravitational microlensing and the galactic halo. *Physical Review D (Particles, Fields, Gravitation, and Cosmology)*, 53(8):4138–76, 1996.

- [17] S. M. Grannan, B. A. Young, A. E. Lange, S. Labov, B. Sadoulet, J. Emes, and E. E. Haller. Collection of athermal phonons into doped ge thermistors using quasiparticle trapping. *Journal of Applied Physics*, 77(10):4887–91, 1995.
- [18] C. Hagmann, D. Kinion, W. Stoeffl, K. van Bibber, E. Daw, J. McBride, H. Peng, L. J. Rosenberg, H. Xin, J. Laveigne, P. Sikivie, N. S. Sullivan, D. B. Tanner, D. Moltz, F. Nezrick, M. S. Turner, N. Golubev, and L. Kravchuk. First results from a second generation galactic axion experiment. *Nuclear Physics B, Proceedings Supplements*, 51(B):209–12, 1996.
- [19] G. Heusser. Low- radioactivity background techniques. *Ann. Rev. Nucl. Part. Sci.*, 45:543–90, 1995.
- [20] K. D. Irwin. An application of electrothermal feedback for high resolution cryogenic particle detection. *Applied Physics Letters*, 66(15):1998–2000, April 1995.
- [21] K. D. Irwin, Sae Woo Nam, et al. A quasiparticle-trap-assisted transition-edge sensor for phonon-mediated particle detection. *Review of Scientific Instruments*, 66(11):5322–6, November 1995.
- [22] Kent Irwin. *Phonon-Mediated Particle Detection Using Superconducting Tungsten Transition-Edge Sensors*. PhD thesis, Stanford University, 1995.
- [23] G. Jungman, M. Kamionkowski, and K. Griest. Supersymmetric dark matter. *Physics Reports*, 267(5-6):195–373, 1996.
- [24] M. Kamionkowski, K. Griest, G. Jungman, and B. Sadoulet. Model-independent comparison of direct versus indirect detection of supersymmetric dark matter. *Physical Review Letters*, 74(26):5174–7, 1995.

- [25] S. B. Kaplan, C. C. Chi, D. N. Langenberg, J. J. Chang, S. Jafarey, and D. J. Scalapino. Quasiparticle and phonon lifetimes in superconductors. *Physical Review B (Solid State)*, 14(11):4854–73, 1976.
- [26] A. T. Lee, B. Cabrera, B. L. Dougherty, M. J. Penn, J. G. Pronko, and S. Tamura. Measurements of the ballistic-phonon component resulting from nuclear and electron recoils in crystalline silicon. *Physical Review B (Condensed Matter)*, 54(5):3244–56, 1996.
- [27] Adrian Lee. *Cryogenic Phonon-Mediated Particle Detectors for Dark Matter Searches and Neutrino Physics*. PhD thesis, Stanford University, 1992.
- [28] J. D. Lewin and P. F. Smith. Review of mathematics, numerical factors, and corrections for dark matter experiments based on elastic nuclear recoil. *Astroparticle Physics*, 6(1):87–112, 1996.
- [29] F. J. Low. Low-temperature germanium bolometer. *Journal of the Optical Society of America*, 51(11):1300–4, 1961.
- [30] P. N. Luke. Voltage-assisted calorimetric ionization detector. *Journal of Applied Physics*, 64(12):6858–60, 1988.
- [31] J. C. Mather. Bolometer noise: nonequilibrium theory. *Applied Optics*, 21(6):1125–9, 1982.
- [32] B. Neganov and V. Trafimov. *Otkytia: Izobreteniya*, 146:215, 1985.
- [33] M. J. Penn, B. L. Dougherty, B. Cabrera, R. M. Clarke, and B. A. Young. Charge collection and trapping in low-temperature silicon detectors. *Journal of Applied Physics*, 79(11):8179–86, 1996.
- [34] Mike Penn. *Phonon-Mediated Particle Detection Using Superconducting Tungsten Transition-Edge Sensors*. PhD thesis, Stanford University, 1996.

- [35] M. Persic and P. Salucci. The baryon content of the universe. *Monthly Notices of the Royal Astronomical Society*, 258(1):14p–18, 1992.
- [36] Joel Primack. Dark matter and structure formation. In F.P. Ostriker A. Dekel, editor, *Formation of Structure in the Universe*. Cambridge University Press, 1996.
- [37] F. Probst, M. Frank, S. Cooper, P. Colling, D. Dummer, P. Ferger, G. Forster, A. Nucciotti, W. Seidel, and L. Stodolsky. Model for cryogenic particle detectors with superconducting phase transition thermometers. *Journal of Low Temperature Physics*, 100(1-2):69–104, 1995.
- [38] V. C. Rubin. The rotation of spiral galaxies. *Science*, 220(4604):1339–44, 1983.
- [39] T. Shutt and et al. Simultaneous high resolution measurement of phonons and ionization created by particle interactions in a 60 g germanium crystal at 25 mk. *Phys. Rev. Lett.*, 69(24):3531–4, Dec. 1992.
- [40] Tom Shutt. *A Dark Matter Detector Based on the Simultaneous Measurement of Phonons and Ionization at 20mK*. PhD thesis, Stanford University, 1995.
- [41] S. Tamura. Monte carlo study of effective decay time of high-frequency phonons. In A. C. Anderson and J. P. Wolfe, editors, *Phonon Scattering in Condensed Matter V. Proceedings of the Fifth International Conference*, pages 356–8. Springer-Verlag, Berlin, West Germany, 1986.
- [42] S. Tamura, J. A. Shields, and J. P. Wolfe. Lattice dynamics and elastic phonon scattering in silicon. *Physical Review B (Condensed Matter)*, 44(7):3001–11, 1991.
- [43] A. Udalski, A. Olech, M. Szymanski, J. Kaluzny, M. Kubiak, M. Mateo, and W. Krzeminski. The optical gravitational lensing experiment. the catalog of

- periodic variable stars in the galactic bulge. iii. periodic variables in four baade's window fields: Bw5, bw6, bw7 and bw8. *Acta Astronomica*, 45(3):433–622, 1995.
- [44] J. N. Ullom, P. A. Fisher, and M. Nahum. A direct measurement of the quasi-particle trapping efficiency for a normal metal trap. *Nuclear Instruments & Methods in Physics Research, Section A (Accelerators, Spectrometers, Detectors and Associated Equipment)*, 370(1):98–100, 1996.
- [45] R. P. Welty and J. M. Martinis. A series array of DC SQUIDs. *IEEE Trans. Magn.*, 27(2):2924–6, 1990.
- [46] S. D. M. White, J. F. Navarro, A. E. Evrard, and C. S. Frenk. The baryon content of galaxy clusters: a challenge to cosmological orthodoxy. *Nature*, 366(6454):429–33, 1993.
- [47] Betty Young. *Phonon-Mediated Detection of Elementary Particles Using Silicon Crystal Acoustic Detectors*. PhD thesis, Stanford University, 1995.

Appendix A

Q amplifiers in detail

A.1 Noise in a the Charge Amplifier Readout

The general noise behavior of a charge amplifier system which is front-end noise limited is relatively straightforward to analyze. The schematic for such an analysis is in figure A.1 where the input impedance is given by Z_i . The detector capacitance

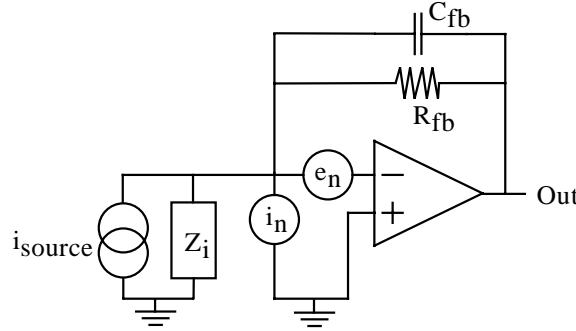


Figure A.1: Schematic of a charge amplifier with signal and noise sources.

and stray capacitances are folded into this impedance.

Under the ideal op-amp approximation, the output voltage can be written as

$$v_{out} = \frac{R_{fb}}{1 + R_{fb}C_{fb}s} i_{signal} \quad (\text{A.1})$$

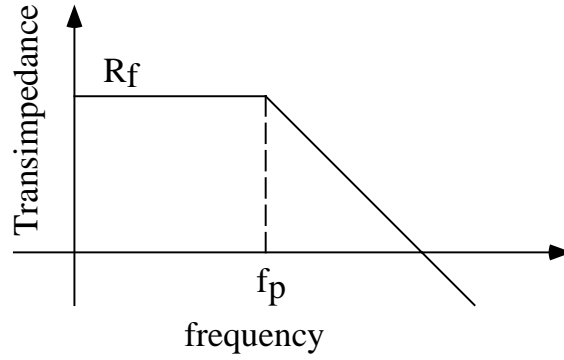


Figure A.2: The Bode plot of the magnitude of the gain/transimpedance of the charge amplifier shown in figure A.1

in the Laplace transform space. For a δ -function input, the output is a single exponential decaying pulse with an $R_{fb}C_{fb}$ time constant. The transimpedance of the Q-amp appears in figure A.2.

Using the ideal op-amp approximations, the contribution of the front-end voltage noise, e_n , to the overall noise can be derived to be

$$v_{e_n} = \left(1 + \frac{\frac{R_{fb}}{1+R_{fb}C_{fb}}}{Z_i} \right) e_n. \quad (\text{A.2})$$

This can be simplified if we assume that the input impedance is dominated by the capacitance of the detector, input capacitance of the charge amplifier, and stray capacitances. If we represent the sum of those capacitances as C_i , then we find

$$v_{e_n} = \frac{R_{fb}(C_i + C_{fb})s + 1}{R_{fb}C_{fb}s + 1} e_n \quad (\text{A.3})$$

We can rewrite the above equation as

$$v_{e_n} = H(s)e_n \quad (\text{A.4})$$

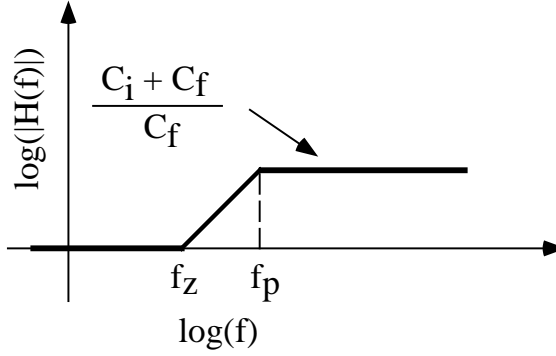
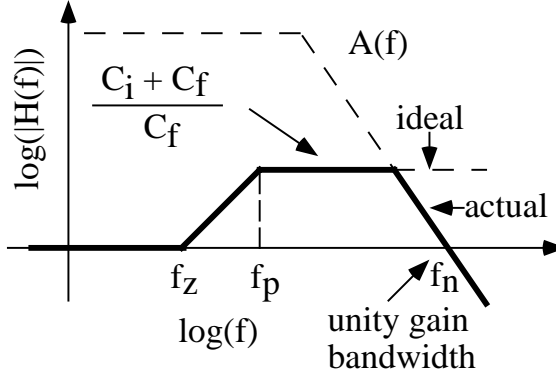
Figure A.3: Bode plot of the magnitude of $H(s)$.

Figure A.4: The system function response for a voltage noise source.

where

$$H(s) = \frac{R_{fb}(C_i + C_{fb})s + 1}{R_{fb}C_{fb}s + 1} \quad (\text{A.5})$$

The Bode plot for $H(s)$ appears in figure A.3. There is one pole at f_p , corresponding to the $R_{fb}C_{fb}$ time constant. There is also one zero at f_z corresponding to the $R_{fb}(C_{fb} + C_i)$. In our case the gain above f_p is typically around 100.

We can relax the assumption of an ideal op-amp, by convolving the frequency response of the op-amp with $H(s)$ derived above. The answer is shown pictorially in figure A.4. The magnitude of the open loop gain of the op-amp is labeled by $A(f)$ and is sketched in the figure. The frequency at which the overall gain equals one is known as the unity gain bandwidth and is denoted in the figure by f_n .

If we know the spectrum of the voltage noise source, e_n , it is straightforward

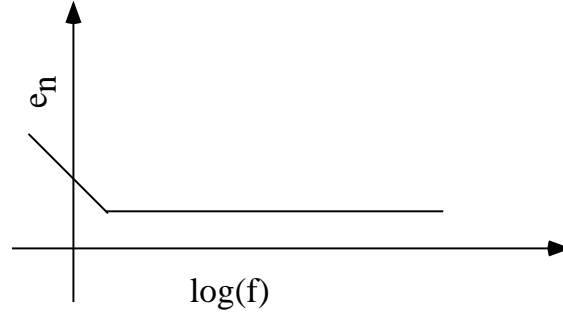


Figure A.5: Sketch of a typical voltage noise spectrum for the front end components of a charge amplifier

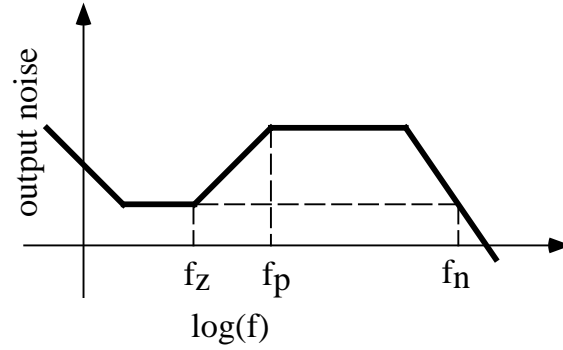


Figure A.6: The contribution of the input voltage noise to the output voltage noise.

to determine the output noise. An typical example for a voltage noise spectrum is shown in figure A.5. The noise is flat except for $1/f$ noise at low frequencies. This is typical for FET front end electronics.

The voltage noise contribution to the total output voltage noise is the sum of the two previous plots (this is the point of using a log scale) and appears in figure A.6.

Using a similar analysis, the input current noise, i_n , contribution to the output voltage noise can be determined. For the current noise, the output voltage noise is given by

$$v_{i_n} = \frac{R_{fb}}{1 + R_{fb}C_{fb}} i_n. \quad (\text{A.6})$$

Figure A.2 is the transimpedance gain, and a typical input current noise spectrum appears in figure A.7.

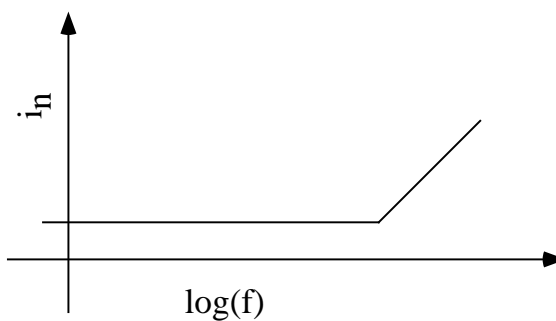


Figure A.7: Typical input current noise for a charge amplifier.

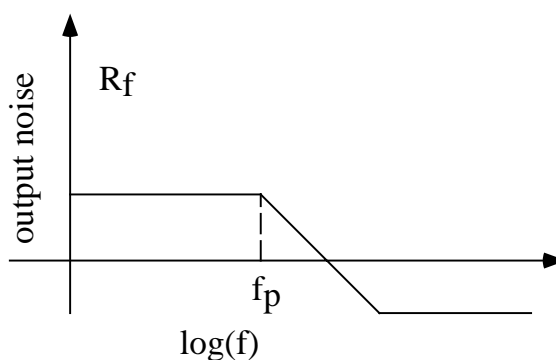


Figure A.8: The contribution of the input current noise to the output voltage noise.

As a result, the contribution of i_n to the output voltage noise is drawn in figure A.8.

In practice, the overall contribution of the voltage noise source to the output voltage noise is much greater than the contribution from the input current noise. As a result, the output voltage spectra looks like figure A.6 when the readout scheme is front-end electronics limited.

A.2 Ionization Signal to Noise Optimization

The optimization of signal to noise for a charge amplifier readout has can be found in many places. However, I've always found them to be rather obtuse. I present a more straightforward derivation for the ionization scheme I used.

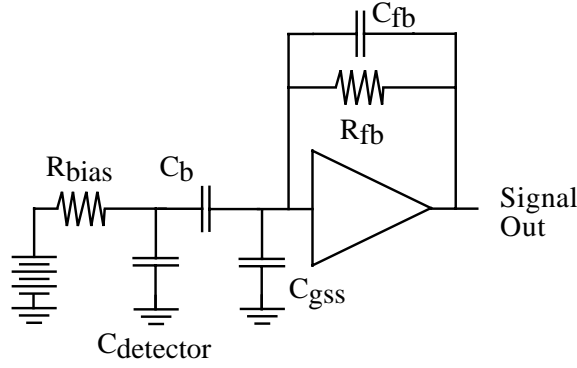


Figure A.9: Q amp schematic which includes the blocking capacitor and the input capacitance of the charge amplifier

The basic idea is to minimize the output voltage due to noise. From the derivations in the previous section we know that output voltage from noise is given by

$$v_{out}^{noise} = i_n Z_f + \frac{v_n}{Z_i} Z_f \quad (\text{A.7})$$

where Z_f is the impedance of the feedback element in the charge amplifier and Z_i is the impedance appearing at the input. Figure A.9 is a schematic of the ionization readout which includes the capacitances to consider when determining Z_i . To optimize the signal to noise, the capacitance, C_{gss} due to the input of the charge amplifier must be considered. In fact C_{gss} should not only include capacitances of the first stage of the amplifier, but also stray capacitances. However, for notational convenience I am labelling it C_{gss} because that is the dominant source (the input FET).

The charge amplifier circuit including noise sources including noise sources is shown in figure A.10. The voltage noise of the first stage amplifier typically dominates the output noise as given in equation A.7. We use a cold FET at the front end

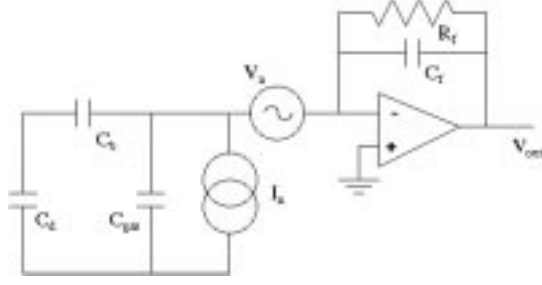


Figure A.10: Schematic of the Q amplifier including noise sources

of the charge amplifier. Typcially,

$$v_n \propto \frac{1}{g_m} \propto \frac{1}{C_{gss}}. \quad (\text{A.8})$$

Using the Laplace transform formalism, we can write

$$Z_i = \frac{1}{(C_d + C_{gss})s}. \quad (\text{A.9})$$

Using the relation between the voltage noise and gate capacitance and the expression for the output voltage noise, we find that

$$v_{out}^{noise} \propto \frac{(C_d + C_{gss})}{\sqrt{C_{gss}}} \quad (\text{A.10})$$

Minimizing the ouput voltage noise with respect to C_{gss} , we find that the minimum occurs when C_{gss} equals C_d .

A.3 Calculating the electronics limit to the rise time

Previous analysis of the Q amplifiers which were available to me idealized the response of the Q amp (i.e. infinite open loop gain). This simplification makes circuit

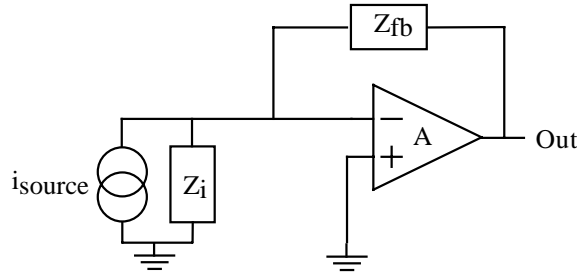


Figure A.11: Simplified Schematic of the Q amplifier

analysis and understanding noise sources significantly easier. However, it doesn't model leading edge behavior correctly. In this section, I derive the electronics rise time by considering the finite gain and bandwidth of the Q amplifier circuit.

The charge amplifier that we use can be simply modeled using the schematic shown in figure A.11 where Z_i is the input impedance, Z_{fb} is the impedance of the feedback network, and A is the open loop gain of the op-amp.

At the inverting terminal of the op-amp we can write the following expressions:

$$\begin{aligned} i &= \frac{v_-}{Z_i} + \frac{v_- - v_o}{Z_{fb}} \\ v_o &= -Av_- \end{aligned} \quad (\text{A.11})$$

where i is the input current (charge pulse), v_- is the voltage at the inverting terminal, and v_o is the output voltage. By combining the two equations, we get an expression containing only the output voltage and the input current:

$$i = -\frac{v_o}{AZ_i} - \frac{1 + \frac{1}{A}}{Z_{fb}} v_o \quad (\text{A.12})$$

$$= -\left(\frac{1}{AZ_i} + \frac{1}{AZ_{fb}} + \frac{1}{Z_{fb}} \right) v_o \quad (\text{A.13})$$

Solving for v_o yields

$$v_o = -\frac{Z_{fb}}{1 + \frac{1}{A} \left(1 + \frac{Z_{fb}}{Z_i} \right)} i \quad (\text{A.14})$$

To proceed further, we need to use expressions for Z_{fb} , Z_i , and A . Of the three parameters, Z_{fb} is the most straightforward to model. It is the parallel combination of the feedback capacitor, C_{fb} , and feedback resistor, R_{fb} . From this point forward, it is much more convenient to express the results using the Laplace transformation formalism. Unless otherwise noted, the variables are in frequency space. We can write

$$Z_{fb} = \frac{R_{fb}}{1 + R_{fb}C_{fb}s} \quad (\text{A.15})$$

$$= \frac{R_{fb}}{1 + \tau_{fb}s} \quad (\text{A.16})$$

where $\tau_{fb} = R_{fb}C_{fb}$. For simplicity, I will assume that Z_i is due to an input capacitance, C_i . A much more complex expression for the input impedance can be written which describes the AC coupled nature of the input circuitry, but to first order approximating the input impedance as a single input capacitance is adequate. It is also convenient to describe the frequency response of the op-amp with a single pole where

$$A(\omega) = \frac{A_o\omega_o}{s + \omega_o}. \quad (\text{A.17})$$

In the expression for A , the gain-bandwidth product of the op-amp is given by $A_o\omega_o$.

Using the approximate expressions for Z_{fb} , Z_i , and A , we find

$$v_o = -\frac{Z_{fb}}{1 + \frac{1}{A}\left(1 + \frac{Z_{fb}}{Z_i}\right)}i \quad (\text{A.18})$$

$$= -\frac{\frac{R_{fb}}{1 + \tau_{fb}s}}{1 + \frac{\omega_o + s}{A_o\omega_o}\left(1 + \frac{R_{fb}C_i s}{1 + \tau_{fb}s}\right)}i \quad (\text{A.19})$$

$$= -\frac{R_{fb}}{1 + \tau_{fb}s + \frac{(s + \omega_o)(1 + \tau_{fb}s + R_{fb}C_i s)}{A_o\omega_o}}i \quad (\text{A.20})$$

$$= -\frac{R_{fb}}{1 + \tau_{fb}s + \frac{(s + \omega_o)(1 + (\tau_{fb} + R_{fb}C_i)s)}{A_o\omega_o}}i \quad (\text{A.21})$$

$$(A.22)$$

If we define, $\tau_1 = \tau_{fb} + R_{fb}C_i$ than the expression for v_o can be written as

$$v_o = -\frac{R_{fb}}{1 + \tau_{fb}s + \frac{(s+\omega_o)(1+\tau_1s)}{A_o\omega_o}}i \quad (A.23)$$

$$= -\frac{R_{fb}}{\frac{\tau_1}{A_o\omega_o}s^2 + \left(\frac{1+\omega_o\tau_1}{A_o\omega_o} + \tau_{fb}\right)s + \left(1 + \frac{1}{A_o}\right)}i. \quad (A.24)$$

In the ideal op-amp limit where $A \rightarrow \infty$, we get the familiar result that

$$v_o = \frac{R_f}{\tau_{fb}s + 1}i \quad (A.25)$$

If we approximate an event as a delta function in current, $i = Q\delta(t)$, than for the ideal op-amp scenario,

$$v_o = \frac{\tau_{fb}}{\tau_{fb}s + 1} \frac{Q}{C_{fb}}. \quad (A.26)$$

In the time domain, the output voltage, v_o is a pulse with an infinitely fast rise and an exponentially decaying tail with a decay time of τ_{fb} .

In the non-ideal case, the situation is more complicated. To determine the shape of the output pulse from an impulse, it is necessary to determine the poles of the non-ideal op-amp expression for v_o . The poles are the roots of the equation

$$s^2 + \left(\frac{1 + \omega_o\tau_1 + A_o\omega_o\tau_{fb}}{\tau_1}\right)s + \frac{\omega_o}{\tau_1}(A_o + 1) = 0 \quad (A.27)$$

and are given by

$$p = -\frac{2\frac{(1+A_o)\omega_o}{1+\omega_o\tau_1+A_o\omega_o\tau_{fb}}}{1 \pm \sqrt{1 - 4\frac{(1+A_o)\omega_o\tau_1}{(1+\omega_o\tau_1+A_o\omega_o\tau_{fb})^2}}} \quad (A.28)$$

In the limit that $A_o \gg 1$ and $A_o C_{fb} \gg C_i$, the poles are approximately given by

$$p_{1,2} = -\frac{1}{\tau_{fb}}, -\frac{A_o \omega_o \tau_{fb}}{\tau_1} \quad (\text{A.29})$$

Using the poles, we can write v_o in partial fraction form,

$$v_o = -\frac{R_{fb} A_o \omega_o}{\tau_1} \left(\frac{\frac{1}{p_1 - p_2}}{s - p_1} + \frac{\frac{1}{p_2 - p_1}}{s - p_2} \right) i \quad (\text{A.30})$$

where p_1 and p_2 are the two poles. If we let

$$p_1 = -\frac{1}{\tau_{fb}} = -\frac{1}{\tau_f} \quad (\text{A.31})$$

$$p_2 = -\frac{A_o \omega_o \tau_{fb}}{\tau_1} = -\frac{1}{\tau_r}, \quad (\text{A.32})$$

then the expression for v_o simplifies to

$$v_o = -\frac{R_{fb}}{\tau_f - \tau_r} \left(\frac{\tau_f}{\tau_f s + 1} - \frac{\tau_r}{\tau_r s + 1} \right) i. \quad (\text{A.33})$$

For an impulse of current, $i = Q\delta(t)$, the output voltage is given by

$$v_o = -\frac{QR_{fb}}{\tau_f - \tau_r} \left(\frac{\tau_f}{\tau_f s + 1} - \frac{\tau_r}{\tau_r s + 1} \right). \quad (\text{A.34})$$

In the time domain, the output voltage is a pulse with an exponential rise given by τ_r and an exponential fall given by τ_f .

$$v_o = \frac{Q}{C_{fb} - \frac{\tau_r}{R_{fb}}} \left(e^{-\frac{t}{\tau_f}} - e^{-\frac{t}{\tau_r}} \right) \quad (\text{A.35})$$

where

$$\tau_f = \tau_{fb} = R_{fb} C_{fb} \quad (\text{A.36})$$

and

$$\tau_r = \frac{\tau_1}{A_o\omega_o\tau_{fb}} = \frac{C_{fb} + C_i}{C_{fb}} \frac{1}{A_o\omega_o}. \quad (\text{A.37})$$

The amplitude of the pulse is roughly $\frac{Q}{C_{fb}}$. However, the maximum pulse height can be significantly less than the amplitude. For example, in the case where the rise time is 5 μ seconds and the fall time is 40 μ seconds, the pulse height is 0.65 of the amplitude. Basically, the slow rise time cuts off the expected pulse height. This effect is also known as ballistic deficit. Thus, in situations where the algorithms for determining the amount of charge for an event is the pulse height, a charge amplifier with a small rise time will give poor signal to noise. From the above derivation, it is clear that charge amplifiers with larger open loop gain ($A_o\omega_o$) will result in faster rise times and larger pulse heights.

A.4 Determining Depth from charge amplifiers

In principle, the ultimate limit to the rise time of the measured pulse is due to the momentary flow of charge as the electron-hole pairs from an event drift across the crystal. If the Q amplifier electronics were fast enough, the leading edge shape of the pulse could give information as to depth of the event within the crystal. To determine the feasibility of extracting depth information using charge amplifiers in a silicon FLIP detector, I simulated the expected pulse shape using the simple model for the charge amplifier derived in the previous section. In my simulation, I assumed no charge trapping and that the electrons and holes drift at the same speed of 0.02mm/ns. I assumed the crystal was 10mm thick and started events at 0 to 5 mm in depth in steps of 1mm. The current profile as a function of time was assumed to be step like. Initially, the current is due to both charge carriers drifting towards the electrodes. When one sign has reached an electrode, the current is cut in half until the charge has reached the second electrode.

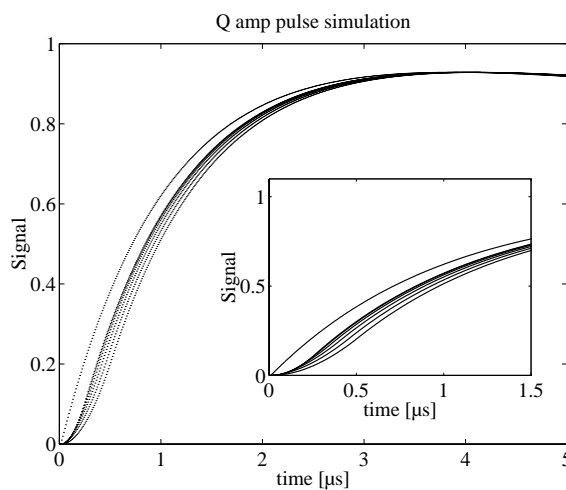


Figure A.12: Leading edge behavior of Q pulses assuming a GBW of 1×10^8

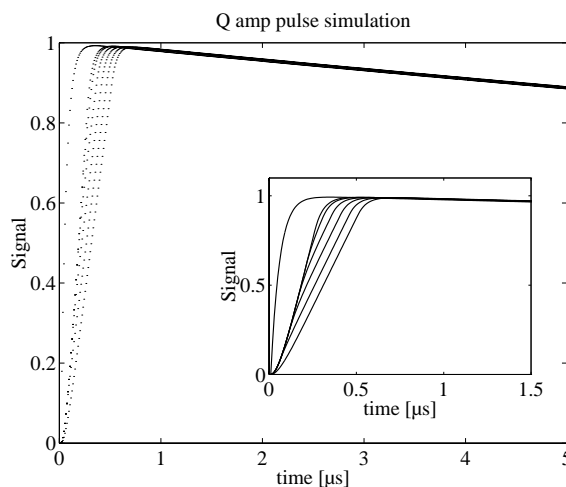


Figure A.13: Leading edge behavior of Q pulses assuming a GBW of 2×10^9

The three plots below are the response of the Q amp as I varied the Gain-Bandwidth product. Each plot has seven curves. The curve with the fastest rise time is the circuits response to an impulse. The six slower curves are the response of the Q amp to events at different depths. The fastest of the slower six is the 5mm starting point and slowest is the 0mm starting point. The Q amplifier I modeled includes the effect of the detector capacitance, fet capacitance and stray capacitances at the gate.

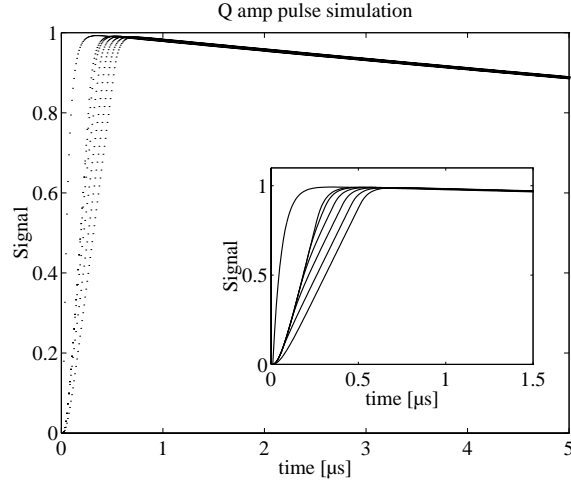


Figure A.14: Leading edge behavior of Q pulses assuming a GBW of 2×10^{10}

From the data it is clear that resolving depth may be impractical using the Q amplifiers. For the lower GBW circuits, the only way to discern differences is at the onset of pulses. This is virtually impossible once noise is introduced. For the high GBW circuit which is probably achievable, the need for even faster digitizers makes this impractical. One possibility (BTW, this is a complete stab in the dark) is to try using a transimpedance amplifier or a voltage amplifier. In many ways this is analagous to FLIP vs BLIP phonon sensors. With BLIP which effectively integrates the heat ie charge amp resolution is great. With FLIP there is an attempt to look at the flux of heat ie transimpedance/voltage amp where the resolution may be degraded.

However, the use of a charge amplifier to determine depth may not be out of the realm of possibility in a Ge detector where the drift velocities are slower.

A.5 UCB discrete Qamp addendum

For our detectors, it is desirable to use charge amplifiers with a fast rise time. The most compelling reason is that a charge amplifier with a low gain-bandwidth and

an associated slow rise time yields suppressed peak heights. In principle, the signal can be recovered with pulse processing, but in practice, such techniques are often limited by non gaussian noise processes and low frequency noise sources. For FLIP detectors, it is desirable to use a Q amplifier with a fast to define a “ t_o ” for an event. A good t_o is necessary to extract information about the position of the event within the crystal.

There are two charge amplifier systems which we’ve been using. One is based on a commercially available package, A250, from AmpTek. The second is a discrete component circuit designed by members of the CDMS collaboration at UCB. On benchtop setups, one sees that the A250 design gives much faster pulses than the UCB design with the same front end FET.

Unfortunately, the A250 design doesn’t easily work in the CDMS experimental setup. The coaxial connections between the front end FET and the A250 seems to introduce enough phase delay to cause a resonance. On the other hand, the UCB design doesn’t suffer from a similar resonance, but the rise time is on order of 5 μ s.

One potential advantage of the UCB design is that we can attempt to optimize the circuit to achieve faster rise times. The first step is to understand the origin of the limits in the rise time as currently designed. A simplified version of the schematic appears in the figure below.

The design is rather elegant, and the calculation of the open loop gain is straightforward. The voltage at the drain of the input FET is fixed using a cascode design with Q1. Fluctuations in the input voltage are converted to fluctuations in drain current using the transimpedance g_m of the front end FET. The current fluctuations are passed through collector of Q1 and can flow either through R4, into the base of Q2, or through the capacitors C4 or C5. For now, we will only consider slow signals so that C4 and C5 can be ignored. When we consider the bandwidth, we will reexamine the effects of C4 and C5. For small signals, the effective impedance of R4

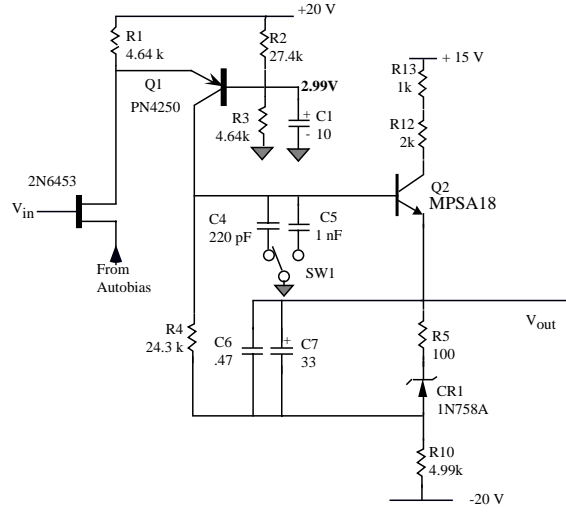


Figure A.15: Simplified Schematic of the UCB Berkeley Q-amp

is much bigger than that seen through the base of Q2. Consequently, the current flows through the base of Q2. Because of the transistor action in Q2, the emitter current is the current gain β_{Q2} times the base current. As a result, the change in output voltage is the change in the emitter current multiplied by the value of R10. So, the overall open loop gain is given by

$$A_o = g_m \beta_{Q2} R_{10}. \quad (\text{A.38})$$

where g_m is the transconductance of the FET, β_{Q2} is the current gain of Q2.

To determine the bandwidth, we need to examine the effects of C4 and C5. Basically, the C4 and C5 shunt AC currents. The cutoff frequency is determined by the RC time constant where C is either C4 or C5 and R is the input resistance seen at the base of Q2. Because the other end of R4 is attached to R10, the effective AC input resistance is given by

$$R \approx \beta_{Q2} R_{10}. \quad (\text{A.39})$$

As a result, we see that the bandwidth is given by

$$\omega_o = \frac{1}{C\beta_{Q2}R_{10}}. \quad (\text{A.40})$$

This leads to an expression the following expression for the gain-bandwidth

$$A_o\omega_o = \frac{g_m\beta_{Q2}R_{10}}{C\beta_{Q2}R_{10}} = \frac{g_m}{C} \quad (\text{A.41})$$

Looking at data sheets for the input FET (IF4500), I found that g_m is typically 15 mS. Usually, C is 1 nF. This yields a GBW of 1.5×10^7 . Using the previously derived formulas for $\tau_r = \frac{C_{fb}+C_i}{C_{fb}} \frac{1}{A_o\omega_o}$ and estimating that $C_{fb} \approx 1$ pF and $C_i \approx 100$ pF, we find that the τ_r is $\approx 7\mu\text{s}$. This agrees well with what we have observed!

In terms of getting the amplifier to work at high speed with a stripline, it looks like the capacitive and inductive effects of a stripline need to be examined. For example, a back of the envelope calculation which estimates the capacitance of a stripline trace to be on the order of 300 pF could introduce a phase shift on the output terminal which may be sufficient to cause an oscillation. In the UCB discrete design, if the emitter-follower output stage has an output impedance of 5 kohms (I am guessing without having done a proper calculation). An output pulse would be rounded by the RC time constant of the output resistance and stripline capacitance. This is around $1.5 \mu\text{seconds}$. Another less likely possibility is that the capacitance on the drain is causing the phase shift. Yet another possibility is that the auto-bias circuit doesn't have enough capacity (capacitor output) to provide the necessary current quickly.

Appendix B

Enhanced Electrothermal Feedback

B.1 Enhanced ETF simplified theory[†]

For simplicity, consider the differential equation which describes the temperature of the electron system and assumes the substrate is a sufficiently good heat sink:

$$c_v \frac{dT}{dt} = \frac{V_{bias}^2}{R(T)} - \Sigma(T^n - T_s^n), \quad (\text{B.1})$$

Linearizing leads to

$$c_v \frac{d \delta T}{dt} = 2i_s \delta V - \frac{P_o \alpha_o}{T_c} \delta T - g_o \delta T \quad (\text{B.2})$$

If we make δV proportional to δi (change in current through the sensor) we can enhance the reduction in joule heating which occurs when there is injection of heat

[†]Latex'ed December 2, 1998.

into a voltage biased TES.

So if we use

$$\delta V = R_c \delta i \quad (\text{B.3})$$

and

$$\delta i = i_s \left(\frac{\delta V}{V_{bias}} - \frac{\delta R}{R_o} \right), \quad (\text{B.4})$$

we can determine expressions for δV and δi :

$$\delta V = -V_{bias} \frac{R_c}{R_o - R_c} \frac{\delta R}{R_o} \quad (\text{B.5})$$

$$\delta i = -\frac{V_{bias}}{R_o - R_c} \frac{\delta R}{R_o}. \quad (\text{B.6})$$

So substituting into B.2 and using the small signal approximation that

$$\frac{\delta R}{R_o} = \alpha_o \frac{\delta T}{T_o} \quad (\text{B.7})$$

leads to

$$c_v \frac{d \delta T}{dt} = -2 \frac{R_c}{R - R_c} \frac{P_o \alpha_o}{T_c} \delta T - \frac{P_o \alpha_o}{T_c} \delta T - g_o \delta T \quad (\text{B.8})$$

$$= -\frac{R_o + R_c}{R_o - R_c} \frac{P_o \alpha_o}{T_c} \delta T - g_o \delta T \quad (\text{B.9})$$

This means there is an effective speed up over intrinsic the intrinsic time constant by a factor of $1 + \frac{R_o + R_c}{R_o - R_c} \frac{\alpha}{n}$.

B.2 Noise issues with EETF

To understand the noise issues, we need consider noise fluctuation in the context of equation B.2 and also extend the equation to include power flows due to noise. The new equation is

$$c_v \frac{d \delta T}{dt} = 2i_s \delta V - \frac{P_o \alpha_o}{T_c} \delta T - g_o \delta T + P_J + P_\Phi \quad (\text{B.10})$$

where P_J is the power due to Johnson noise, P_Φ is the power fluctuations due to phonon noise. The contribution of the noise in the active bias feedback is subtle. I find that it is convenient to introduce the following expression for δV :

$$\delta V = R_c \delta i_m \quad (\text{B.11})$$

$$= R_c \delta i + R_c i_n \quad (\text{B.12})$$

where δi_m is the change in current observed by the electronics and includes electronics noise, δi is the actual current through the sensor, and i_n is the electronics noise referenced to the input (we are not capable of measuring this because it is folded into i_m). Using the fact that

$$\delta i = i_o \left(\frac{\delta V}{V_{bias}} - \frac{\delta R}{R_o} \right) \quad (\text{B.13})$$

$$= -i_o \frac{\delta R}{R_o - R_c} + \frac{R_c}{R_o - R_c} i_n, \quad (\text{B.14})$$

equation B.10 can be rewritten as

$$\begin{aligned} c_v \frac{d \delta T}{dt} &= 2i_s R_c \delta i + 2i_s R_c i_n - \frac{P_o \alpha_o}{T_c} \delta T - g_o \delta T + P_J + P_\Phi \\ &= -\frac{R_o + R_c}{R_o - R_c} \frac{P_o \alpha_o}{T_c} \delta T - g_o \delta T + 2i_s R_c i_n + \frac{2R_c^2 i_o}{R_o - R_c} i_n \end{aligned} \quad (\text{B.15})$$

$$+P_J + P_\Phi \quad (\text{B.16})$$

$$= -\frac{R_o + R_c}{R_o - R_c} \frac{P_o \alpha_o}{T_c} \delta T - g_o \delta T + 2 \frac{R_c R_o i_o i_n}{R_o - R_c} + P_J + P_\Phi \quad (\text{B.17})$$

It is convenient to define

$$g_{enh} = \frac{R_o + R_c}{R_o - R_c} \frac{P_o \alpha_o}{T_c} \quad (\text{B.18})$$

and

$$P_{fb} = 2 \frac{R_c^2 i_o i_n}{R_o - R_c} \quad (\text{B.19})$$

so that the differential equation describing the temperature fluctuations in the sensor can be written as

$$c_v \frac{d \delta T}{dt} = -g_{enh} \delta T - g_o \delta T + P_{fb} + P_J + P_\Phi. \quad (\text{B.20})$$

Taking the Laplace Transform of the previous equation leads to

$$\widetilde{\delta T} = \frac{\widetilde{P_{fb}} + \widetilde{P_J} + \widetilde{P_\Phi}}{c_v s + g_{enh} + g_o}. \quad (\text{B.21})$$

For convenience, unless explicitly stated, it is understood that the equations from here on are in the frequency domain after a Laplace transformation. The measured noise referenced to the input is a combination of the Johnson noise of the sensor, electronics noise of the readout, and noise due to temperature fluctuations:

$$i_m = i_J + i_n + i_T. \quad (\text{B.22})$$

Using B.14 and B.21,

$$i_T = -\frac{i_o R_o \alpha_o}{R - R_c} \frac{\delta T}{T_o} + \frac{R_c}{R - R_c} i_n \quad (\text{B.23})$$

$$= -\frac{i_o R_o}{R_o - R_c} \frac{\alpha_o}{T_o} \left(\frac{P_{fb} + P_J + P_\Phi}{c_v s + g_{enh} + g_o} \right) + \frac{R_c}{R - R_c} i_n \quad (\text{B.24})$$

$$= -\frac{1}{i_o (R_o + R_c)} \frac{P_{fb} + P_J + P_\Phi}{\frac{c_v}{g_{enh}} s + 1 + \frac{g_o}{g_{enh}}} + \frac{R_c}{R_o - R_c} i_n \quad (\text{B.25})$$

Substituting back into the expression for the i_m , assuming $g_o \ll g_{enh}$, and defining

$\tau_{enh} = \frac{c_v}{g_{enh}}$ leads to

$$i_m = i_n + i_J - \frac{1}{i_o (R_o + R_c)} \left(\frac{P_{fb} + P_J + P_\Phi}{\tau_{enh} s + 1} \right) + \frac{R_c}{R_o - R_c} i_n \quad (\text{B.26})$$

$$\begin{aligned} &= i_J - \frac{1}{i_o (R_o + R_c)} \left(\frac{P_J + P_\Phi}{\tau_{enh} s + 1} \right) \\ &\quad - \left(\frac{2R_c R_o}{R_o^2 - R_c^2} \right) \frac{i_n}{\tau_{enh} s + 1} + \frac{R_o}{R_o - R_c} i_n \end{aligned} \quad (\text{B.27})$$

From the previous equation, it is apparent that there are three uncorrelated noise sources which must be added in quadrature, the electronics noise, Johnson noise, and phonon noise.

B.2.1 Electronics noise contribution

The electronics noise contribution is given by

$$i = - \left(\frac{2R_c R_o}{R_o^2 - R_c^2} \right) \frac{i_n}{\tau_{enh} s + 1} + \frac{R_o}{R_o - R_c} i_n \quad (\text{B.28})$$

$$= \frac{-2R_c R_o + R_o^2 + R_c R_o + R_o (R_o + R_c) \tau_{enh} s}{\tau_{enh} s + 1} i_n \quad (\text{B.29})$$

$$= \left(\frac{R_o i_n}{R_o + R_c} \right) \left(\frac{\frac{R_o + R_c}{R_o - R_c} \tau_{enh} s + 1}{\tau_{enh} s + 1} \right) \quad (\text{B.30})$$

$$= \left(\frac{R_o i_n}{R_o + R_c} \right) \left(\frac{\tau_{etf} s + 1}{\tau_{enh} s + 1} \right) \quad (\text{B.31})$$

where $\tau_{etf} = \frac{c_v}{g_{etf}}$ and $g_{etf} = \frac{P_o \alpha_o}{\tau_o}$. It is interesting to note that the noise contribution for frequencies below the $1/\tau_{etf}$ the noise is suppressed because of electrothermal

feedback. For frequencies between the $1/\tau_{etf}$ and $1/\tau_{enh}$, the noise increases and finally plateaus above $1/\tau_{enh}$. The value at the upper plateau is given by

$$\frac{R_o}{R_o - R_c} i_n. \quad (\text{B.32})$$

B.2.2 Johnson noise contribution

The Johnson noise contribution is given by

$$i = i_J - \frac{1}{i_o (R_o + R_c)} \frac{P_J}{\tau_{enh}s + 1} \quad (\text{B.33})$$

$$= i_J - \frac{R_o}{(R_o + R_c)} \frac{i_J}{\tau_{enh}s + 1} \quad (\text{B.34})$$

$$= \left(\frac{R_c}{R_o + R_c} \right) \left(\frac{\frac{R_o + R_c}{R_c} \tau_{enh}s + 1}{\tau_{enh}s + 1} \right) i_J \quad (\text{B.35})$$

B.2.3 Phonon noise contribution

The phonon noise contribution is given by

$$i = - \frac{1}{i_o (R_o + R_c)} \frac{P_\Phi}{\tau_{enh}s + 1}. \quad (\text{B.36})$$

In the extreme electrothermal feedback limit where $T_s^n \ll T_o^n$, we can write

$$P_\Phi^2 = 2k (T_o^2 g_o + T_s^2 g_s) \quad (\text{B.37})$$

$$\approx 2k T_o^2 g_o. \quad (\text{B.38})$$

This implies that the phonon noise contribution is given by

$$i = - \frac{1}{i_o (R_o + R_c)} \frac{P_\Phi}{\tau_{enh}s + 1} \quad (\text{B.39})$$

$$= -\frac{1}{i_o (R_o + R_c)} \frac{\sqrt{2kT_o^2 g_o}}{\tau_{enh}s + 1} \quad (\text{B.40})$$

$$= -\frac{1}{i_o (R_o + R_c)} \sqrt{\frac{4kT_o n P_o R_o}{2R_o}} \frac{1}{\tau_{enh}s + 1} \quad (\text{B.41})$$

$$= -\frac{R_o}{R_o + R_c} \frac{\sqrt{n/2}}{\tau_{enh}s + 1} \sqrt{\frac{4kT_o}{R_o}} \quad (\text{B.42})$$

B.3 Fundamental Energy Resolution

The fundamental energy resolution is given by the following expression

$$\Delta E_{RMS}^{-2} = \int_0^\infty \frac{4}{NEP^2} df \quad (\text{B.43})$$

For EETF, the signal which we are able to measure is the change in current and has the following form for small signals:

$$\delta i = -\frac{i_o \alpha_o}{T_o} \frac{R_o}{R_o - R_c} \delta T. \quad (\text{B.44})$$

From the differential equation describing the heat flow in the tungsten electron system, we can write an expression for δT in frequency space,

$$\delta T = \frac{P(w)}{c_v s + g_{enh} + g_o}. \quad (\text{B.45})$$

Using equations B.44, B.45, and the expressions for the measured current noise due to electronics noise, Johnson noise, and phonon noise, we can solve for the “noise equivalent power”, NEP.

$$NEP = -\frac{c_v s + g_{enh} + g_o}{\frac{i_o \alpha_o}{T_o} \frac{R_o}{R_o - R_c}} \delta i_{noise} \quad (\text{B.46})$$

$$= -\frac{\frac{c_v}{g_{enh}} s + 1 + \frac{g}{g_{enh}}}{\frac{1}{i_o (R_o + R_c)}} \delta i_{noise} \quad (\text{B.47})$$

$$= - \left(\tau_{enh}s + 1 + \frac{g_o}{g_{enh}} \right) i_o (R_o + R_c) \delta i_{noise} \quad (B.48)$$

From the previous derivation of the current noise we know that

$$\begin{aligned} i_{noise} &= \frac{R_o}{R_o + R_c} \left(\frac{\tau_{etf}s + 1}{\tau_{enh}s + 1} \right) i_n \\ &\quad - \frac{R_c}{R_o + R_c} \left(\frac{\frac{R_o + R_c}{R_c} \tau_{enh}s + 1}{\tau_{enh}s + 1} \right) i_J \\ &\quad - \frac{R_o}{R_o + R_c} \left(\frac{\sqrt{\frac{n}{2}}}{\tau_{enh}s + 1} \right) \sqrt{\frac{4kT_o}{R_o}} \end{aligned} \quad (B.49)$$

In deriving the previous equation I have simplified the expression by using:

$$P_o \approx \frac{g_o T_o}{n} \quad (B.50)$$

$$g_{etf} = \frac{P_o \alpha_o}{T_o} \approx \frac{g_o \alpha_o}{n} \quad (B.51)$$

$$g_{enh} = \frac{R_o + R_c}{R_o - R_c} g_{etf} \approx \frac{g_o \alpha_o}{n} \frac{R_o + R_c}{R_o - R_c} \quad (B.52)$$

$$\tau_{etf} = \frac{c_v}{g_{etf}} \quad (B.53)$$

$$\tau_{enh} = \frac{c_v}{g_{enh}}. \quad (B.54)$$

Because the i_n, i_J , and the phonon noise are all uncorrelated, we can write an expression for the magnitude of the NEP,

$$\begin{aligned} NEP^2 &= R_o^2 (\tau_{etf}^2 \omega^2 + 1) i_o^2 i_n^2 \\ &\quad + R_c^2 \left(\left(\frac{R_o + R_c}{R_c} \right)^2 \tau_{enh}^2 \omega^2 + 1 \right) i_o^2 i_J^2 \\ &\quad + R_o^2 \frac{n}{2} i_o^2 \frac{4kT_o}{R_o}. \end{aligned} \quad (B.55)$$

Because the magnitude of the Johnson noise and phonon noise contribution is directly related to the size of the Johnson current noise through the sensor, it is convenient to

write the magnitude of the electronics noise, i_n , as a multiple/fraction of the Johnson noise,

$$i_n = \beta \sqrt{\frac{4kT_o}{R_o}} = \beta i_J. \quad (\text{B.56})$$

The NEP can be rewritten as

$$\begin{aligned} NEP^2 &= 4kT_o P_o \beta^2 \left(\tau_{etf}^2 \omega^2 + 1 \right) \\ &\quad + 4kT_o P_o \left(\left(\frac{R_o - R_c}{R_o} \right)^2 \tau_{etf}^2 \omega^2 + \frac{R_c^2}{R_o^2} \right) \\ &\quad + 4kT_o P_o \frac{n}{2}. \end{aligned} \quad (\text{B.57})$$

Using the previous equation we can derive the fundamental energy resolution

$$\begin{aligned} \Delta E_{RMS}^{-2} &= \int_0^\infty \frac{4}{NEP^2} df \\ &= \frac{1}{4kT_o P_o} \int_0^\infty \frac{4}{\left(\beta^2 + \left(1 - \frac{R_c}{R_o} \right)^2 \right) \tau_{etf}^2 \omega^2 + \left(\frac{R_c}{R_o} \right)^2 + \frac{n}{2} + \beta^2} df \\ &= \frac{1}{4kT_o P_o} \frac{1}{\sqrt{\beta^2 + \left(1 - \frac{R_c}{R_o} \right)^2} \tau_{etf}} \frac{1}{\sqrt{\left(\frac{R_c}{R_o} \right)^2 + \frac{n}{2} + \beta^2}} \end{aligned} \quad (\text{B.58})$$

We can replace τ_{etf} in terms of c_v and α_o . This leads to

$$\begin{aligned} \Delta E_{rms}^2 &= 4kT_o P_o \tau_{etf} \sqrt{\beta^2 + \left(1 - \frac{R_c}{R_o} \right)^2} \sqrt{\left(\frac{R_c}{R_o} \right)^2 + \frac{n}{2} + \beta^2} \\ &= 4kT_o^2 \frac{c_v}{\alpha_o} \sqrt{\beta^2 + \left(1 - \frac{R_c}{R_o} \right)^2} \sqrt{\left(\frac{R_c}{R_o} \right)^2 + \frac{n}{2} + \beta^2} \end{aligned} \quad (\text{B.59})$$

This result agrees with the result in Kent's thesis in the limit where $\beta \rightarrow 0$ (no SQUID noise) and $R_c \rightarrow 0$. It is an extension to the derivation in Kent's thesis for ETF noise limits because it considers the more realistic case of including the noise from the measurement scheme by choosing a $\beta \neq 0$ and with $R_c = 0$.

The result also indicates that for situations where the electronics noise is the dominant source, the enhanced electrothermal feedback does not improve upon the ultimate energy resolution achievable. In this limit, ETF and enhanced ETF have the same resolution. Enhanced ETF, however, may yield however better resolution in real world situations since it makes you even less sensitive to low frequency noise. In the limit where the electronics noise is not the dominant form, $\beta \ll 1$, we get the interesting result that the ultimate energy resolution is better than that achievable with ETF. In essence the improvement is by a factor of $\sqrt{1 - \frac{R_c}{R_o}}$. This is really cool. It would be nice to be in this situation.

B.4 Dynamic and source resistance Corrections

To compensate for finite voltage source resistance and the possibility that the TES is not ohmic, I can rewrite equation B.1 as

$$c_v \frac{dT}{dt} = i_s^2 R(T) - \Sigma(T^n - T_s^n), \quad (\text{B.60})$$

where i_s is the current through the sensor and $R(T)$ is the resistance of the TES (bolometer). In the enhanced ETF mode, the bias circuit equation can be written as

$$V_{\text{sensor}} + i_s R_{\text{bias}} = (i_b + f(i_s - i_o)) R_{\text{bias}}, \quad (\text{B.61})$$

where R_{bias} is the bias shunt resistor, i_b is the current through the bias shunt resistor, i_s is the current through the sensor, i_o is the quiescent current through the sensor, and f is the fraction of the current pulse feedback. In essence, $f R_b$ is equivalent to R_c in the previous derivation.

Linearizing the expression for the bias circuit for small deviations around the

operating point yields the equation,

$$Zdi + IdR + R_{bias}di - fR_{bias}di = 0 \quad (\text{B.62})$$

where $Z = \frac{dV}{dT}$ of the sensor. By manipulating the above equation, we can write

$$\frac{di}{i} = -\frac{R}{Z + R_{bias} - fR_{bias}} \frac{dR}{R}. \quad (\text{B.63})$$

If we linearize the differential equation describing the thermal picture assuming that i , R , and T are the independent variables, then we get

$$c_v \frac{d\delta T}{dt} = 2i_s R \delta i + i_s^2 \delta R - \Sigma(T^n - T_s^n). \quad (\text{B.64})$$

Using the expression which relates δi and δR , we get

$$\begin{aligned} c_v \frac{d\delta T}{dt} &= 2P_o \frac{\delta i}{i} + P_o \frac{\delta R}{R} - \Sigma(T^n - T_s^n) \\ &= -\frac{2R}{Z + (1-f)R_{bias}} P_o \frac{\delta R}{R} + P_o \frac{\delta R}{R} - \Sigma(T^n - T_s^n) \\ &= -\frac{2R - Z - (1-f)R_{bias}}{Z + (1-f)R_{bias}} \frac{P_o \alpha_o}{T_c} \delta T - g_o \delta T \end{aligned} \quad (\text{B.65})$$

Now my gut feeling is that the expression,

$$\delta P = 2i_s R \delta i + i_s^2 \delta R \quad (\text{B.66})$$

is incorrect. I think the expression should be something like

$$\delta P = i_s (R + Z) \delta i + i_s^2 \delta R. \quad (\text{B.67})$$

Working carefully, I think this is the way the derivation goes:

$$\delta P = i_s \delta V + V \delta i \quad (\text{B.68})$$

$$= i_s \left(\frac{\partial V}{\partial i} \delta i + \frac{\partial V}{\partial T} \delta T \right) + V \delta i \quad (\text{B.69})$$

$$= i_s (Z + R) \delta i + i_s \frac{\partial V}{\partial T} \delta T \quad (\text{B.70})$$

The equation describing the bias circuit becomes

$$\frac{\partial V}{\partial i} \delta i + \frac{\partial V}{\partial T} \delta T + R_{bias} \delta i - f R_{bias} \delta i = 0 \quad (\text{B.71})$$

Solving for $\frac{\partial V}{\partial T}$ and substituting into the expression for δP , we find that

$$\delta P = i_s (R + (f - 1) R_{bias}) \delta i \quad (\text{B.72})$$

Using the equation for the bias circuit, we can rewrite δP in terms of the change in temperature:

$$\delta P = i_s \left(\frac{R + (f - 1) R_{bias}}{Z - (f - 1) R_{bias}} \right) \frac{\partial V}{\partial T} \delta T. \quad (\text{B.73})$$

If this is correct than the differential equation describing the change in temperature becomes,

$$c_v \frac{d\delta T}{dt} = \delta P - g_o \delta T \quad (\text{B.74})$$

$$= i_s \left(\frac{R + (f - 1) R_{bias}}{Z - (f - 1) R_{bias}} \right) \frac{\partial V}{\partial T} \delta T - g_o \delta T. \quad (\text{B.75})$$

If we assume that $\frac{\partial V}{\partial T} = i_s \frac{\partial R}{\partial T}$, then we find that

$$c_v \frac{d\delta T}{dt} = i_s^2 \left(\frac{R + (f - 1) R_{bias}}{Z - (f - 1) R_{bias}} \right) \frac{\partial R}{\partial T} \delta T - g_o \delta T \quad (\text{B.76})$$

$$= \left(\frac{R + (f - 1) R_{bias}}{Z - (f - 1) R_{bias}} \right) \frac{P_o \alpha_o}{T_c} \delta T - g_o \delta T \quad (\text{B.77})$$